A Versatile Atom Transport Apparatus for Photonics

Björn Ole Mußmann

A Versatile Atom Transport Apparatus for Photonics

Cover

Photo by Pieter van Dorp van Vliet, Faculteit Bètawetenschappen, Universiteit Utrecht; transformed by neural networks (`neural-style` package [Joh15]) with the strokes and colors of Vincent van Gogh's Self-Portrait with Grey Felt Hat.

Ph.D. thesis, Utrecht University, the Netherlands, September 2016
ISBN: 978-90-393-6624-0

A Versatile Atom Transport Apparatus for Photonics

Een Veelzijdige Opstelling ter Verplaatsing van Atomen voor Fotonica

(met een samenvatting in het Nederlands)

Proefschrift

ter verkrijging van de graad van doctor aan de Universiteit Utrecht op gezag van de rector magnificus, prof. dr. G.J. van der Zwaan ingevolge het besluit van het college voor promoties in het openbaar te verdedigen op woensdag 7 september 2016 des ochtends 10.30 uur

door

Björn Ole Mußmann

geboren op 2 september 1981 te Kiel, Duitsland

Promotor:	Prof. dr. P. van der Straten
Copromotor:	Dr. D. van Oosten

This work is financially supported by the *Nederlandse Organisatie voor Wetenschappelijk Onderzoek* (NWO).

Contents

1. Introduction

Cold atoms and nanophotonics are a promising combination for science. By themselves, both fields are already incredibly rich, giving detailed insight into the quantum world. But when two domains of physics meet, their combination allows tools from one field to be transformational in the other.

Cold Atoms Usually fundamental in nature, the study of cold atoms is a very clean approach to investigate laws of physics. By using laser cooling, clouds of atoms are cooled down to millikelvins or microkelvins. The specimens used are of high purity, commonly a specific atom isotope. The potential landscape used to control the atoms can be moulded with fine-grained control with the help of lasers and/or magnetic fields. These features allow for creating unique experiments that explore the principal laws of physics [MvdS12], as well as for modelling other physical systems [Bon15]. Beyond fundamental interest, the applications are diverse, such as sensing [SGV+12] and quantum simulations [BDN12].

Nanophotonics The study of light close to or beyond the diffraction limit is called nanophotonics. In this region, the field-like nature of light can certainly no longer be ignored. By confining light in sub-wavelength-sized structures, high peak intensities can be achieved, giving rise to exciting non-linear optics phenomena. The strong field gradient that can be created allows, for instance, precise spectroscopy measurements, phase-sensitive sub-wavelength microscopy [BK07, BK06], as well as producing highly receptive sensing devices [CLPS15].

Furthermore, nanophotonics can be used for electromagnetically induced transparency and slowing light propagation for creating extremely high light intensities and light filtering [HLW+14].

As a subtopic, the field of nanoplasmonics focuses on photons coupled to collective, coherent electron oscillations on conducting surfaces. Such Surface Plasmon Polaritons have been proposed as a base for circuits that merge photonics and electronics at the nanoscale [Ozb06, ZXL+12, BLSD+10].

1.1. Standing on the Shoulders of Giants

No research happens in figurative vacuum. We learn from the masters of the past and build upon their achievements. As Bernard of Chartres said in the twelfth century [McG62]:

> DICEBAT BERNARDUS CARNOTENSIS NOS ESSE QUASI NANOS, GIGANTIUM HUMERIS INSIDENTES, UT POSSIMUS PLURA EIS ET REMOTIORA VIDERE, NON UTIQUE PROPRII VISUS ACUMINE, AUT EMINENTIA CORPORIS, SED QUIA IN ALTUM SUBVENIMUR ET EXTOLLIMUR MAGNITUDINE GIGANTEA.
>
> Bernard of Chartres used to compare us to [puny] dwarfs perched on the shoulders of giants. He pointed out that we see more and farther than our predecessors, not because we have keener vision or greater height, but because we are lifted up and borne aloft on their gigantic stature.

The first interactions of atoms and resonant light were observed in 1901 [Leb01, NH01], well before coherent light sources were invented. Even more surprisingly, the first application of nanoplasmonics already happened in the 4th century with the fabrication of the Lycurgus cup [FMSH07]. Connecting cold atoms and nanophotonics is not a new idea; fantastic pioneering experiments have been conducted in this area. The potential of combining the two fields is manifold.

Firstly, the high peak intensities and extraordinary gradients of strongly confined light fields open up more ways to influence cold atoms in experiments. These extreme conditions are very challenging to achieve using conventional optics. Moreover, nanoplasmonics allows for new degrees of freedom to tailor the potential landscape for the atoms. Several proposals suggest nanoplasmonic traps for cold atoms [GTC$^+$12, JDGD$^+$13, GTHC$^+$15].

Secondly, cold atoms can be used to probe or influence the electromagnetic fields of photonic or plasmonic devices. Examples include all-optical switching using cold Rubidium atoms [BHB$^+$09] and quantum phase switch with a single atom [TTdL$^+$14].

Thirdly, there are new possibilities for interactions. Cold atoms can influence the interaction of photonic structures. Plasmons can couple cold atoms that are held in different places. The interactions of atoms and plasmons is also an interesting subject to study in itself. Recent research includes coupling of ultracold atoms and surface plasmons [SZS14] and coupling individual atoms to optical cavities [TTdL$^+$13].

Most of these experiments require highly specialized setups. They do one thing and they do it well. But they require choosing the area of research very carefully, for they lack the flexibility to conduct different experiments.

Planning and building experimental setups is a time-consuming endeavour. Being agile and being able to quickly try new ideas is a great boon for scientists. This requires a flexible multipurpose experimental setup.

1.2. A Versatile Atom Transport Apparatus for Photonics

The work in this thesis is based on the idea of building an experimental apparatus that can conduct many types of experiments combining nanophotonics and cold atoms. An apparatus that can switch between different experiments fast. Multiple researchers are expected to alternate

between lab time and analysis, and converting to an entirely different type of experiment should take no longer than a weekend.

Our specimen of choice is a Rubidium isotope. It is a popular choice for cold atom experiments because of many favourable aspects such as a low melting point and high vapour pressure as well as cheaply available laser systems [Geo15]. The vacuum chamber features a load-lock system for quick sample exchange. An optical conveyor-belt system delivers the Rubidium atoms to the sample surface. One restriction for the delivery process to work is that samples must be either transparent or reflective for 780 nm light. Finally, a spectroscopy and imaging setup collects the data from experiments.

A sample case of an experiment is discussed in Chapter 2. It shows the potential and boundary conditions for possible experiments in this apparatus. The setup itself is described in detail in Chapter 3 and characterized in Chapter 4. Finally, Chapter 5 employs a computer model to gain a deeper understanding of the experimental results and to get access to experimental variables that cannot be directly obtained.

2. Motivation

As an example of future experiments, we study a tangible sample case to see what is possible and to explore the boundary conditions. This chapter introduces a series of computer simulations to examine a possible experiment. It allows us to get an impression of necessary constraints and orders of magnitude of relevant variables. One of the key ideas behind the design of the setup is to allow for interactions of cold atoms and evanescent light. In this chapter we simulate the interaction of a cloud of cold atoms with evanescent light surrounding a nanobeam waveguide.

The outline of the system is as follows. A sample is placed into a vacuum chamber. On its surface is a small nanobeam. Light coupled into the nanobeam is so strongly confined that it penetrates into the surrounding vacuum, forming an evanescent field. Cold atoms are transported to the sample surface. They interact with the evanescent field, scatter light, and reduce the transmission of light through the nanobeam. A photodetector measures the loss in transmittance.

The nanobeam can be etched out of a Si_3N_4 (Silicon Nitride) membrane. Test samples are fabricated with a height of 215 nm, a length of 100 µm and a width varying from 300 nm to 20 µm. Near-infrared laser light can be coupled into and out of the beam via gratings on the Si_3N_4 surface. For this light Si_3N_4 has a refractive index of $n_{Si_3N_4} \approx 2$ [Båå82]. Figure 2.1 depicts the theoretical mode profile of a nanobeam with a width of 300 nm. The mode profile is obtained using a fully vectorial finite difference modesolver.*

The same figure indicates atom trajectories around the nanobeam. In

* python: `EMpy.modesolvers.FD.VFDModeSolver`

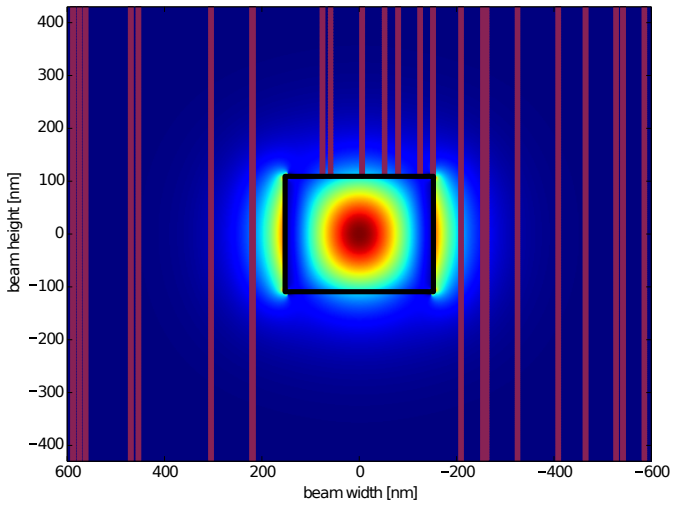

Figure 2.1.: Intensity profile of the mode inside a nanobeam. The outline of the nanobeam is shown in black. The light is so strongly confined that a substantial part of it propagates on the outside of the beam as an evanescent field. Atom trajectories, shown in violet, indicate that atoms either fly past the beam or collide with it.

these simulations, as well as in the real experiments, we work with the isotope Rubidium 87 (^{87}Rb). It has a transition at a frequency corresponding to a wavelength of 780.24 nm [TVH$^+$06]. For strong light-matter interactions we choose the light in the nanobeam to be of this wavelength.

In the experiment (as discussed in Chapter 4) 150 000 ^{87}Rb atoms with a temperature of roughly 1 mK can be brought to the sample. In this simulation, we assume these are simply released and allowed to fall under gravity. Figure 2.2 shows their initial thermal velocity distribution and the rate with which they arrive at the sample surface.

Each atom that penetrates the evanescent field scatters light and change

a)

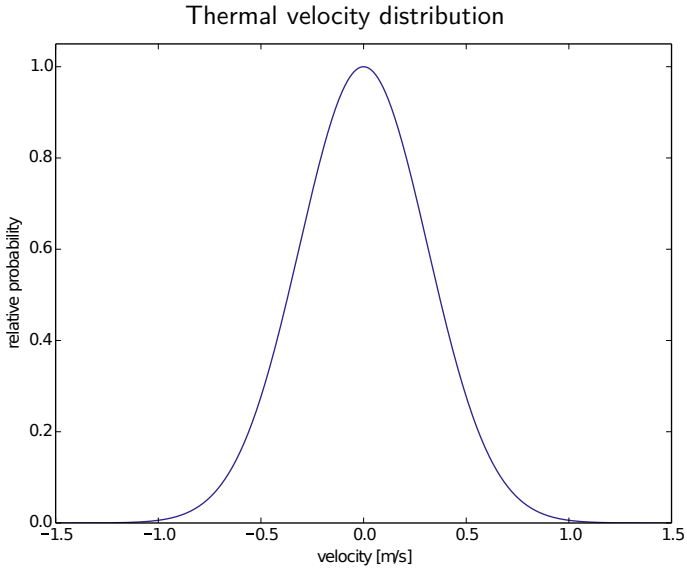

b)

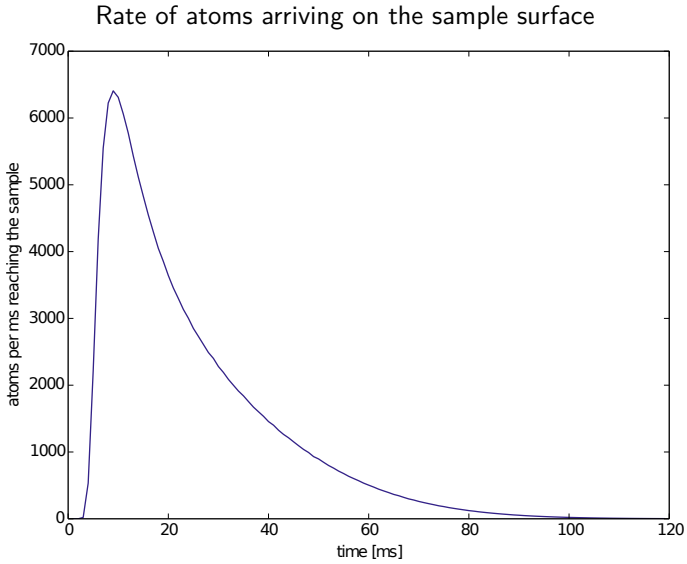

Figure 2.2.: Simulated motion of the atoms. **a)** Thermal velocity distribution of atoms released into the dipole trap. The atom temperature is 1 mK. **b)** Rate of atoms ms^{-1} adsorbing onto the sample surface.

the light transmission through the nanobeam. The power that the atoms can scatter depends strongly on the intensity of the evanescent field. On one hand, a higher beam power results in a lower relative light loss through scattering, because the light intensity exceeds the saturation intensity of the atoms. This results in a low signal. On the other hand, a lower beam power is more difficult to detect, resulting in more noise. A good balance has to be found and several transmitted beam powers are thus tested. The scattered power is

$$P_{\mathrm{scat}} = I\sigma = I\frac{\sigma_0}{1 + 4\delta/\gamma^2 + I/I_{\mathrm{sat}}},$$

with I being the intensity of the light and σ the scattering cross section of one atom. Here σ_0 is the scattering cross section at low intensities, δ the detuning of the light from resonance, γ the natural linewidth and I_{sat} the saturation intensity. Figure 2.3 shows the scattered power versus the intensity of the evanescent field and illustrates the diminishing returns of increasing the intensity.

There are more effects to consider than just the scattering rate, as the close proximity to the nanobeam influences this rate. Proximity to a reflecting surface changes the Local Density Of States (LDOS) of the atoms, as Drexhage demonstrated in his famous experiment [Dre70]. The change in the LDOS can enhance or suppress the scattered power, in essence through destructive or constructive interference. Figure 2.4 shows calculations of the LDOS around a nanobeam with a width of 300 nm. A finite difference time domain approach is used for the calculations.* The LDOS is at most increased by a factor of 2. As the scattered power is linearly dependent on the LDOS [CCC+15], the scattered power is at maximum a factor of two higher than the vacuum value.

Calculating the LDOS at high resolutions is time consuming. For the following simulations of atoms scattering light we therefore neglect the LDOS effects, knowing that the results are off by at most a factor of 2.

The simulated light transmittances through nanobeams are depicted in Figure 2.5. Several nanobeam widths and beam powers are studied.

* meep: MIT Electromagnetic Equation Propagation [ORI+10]

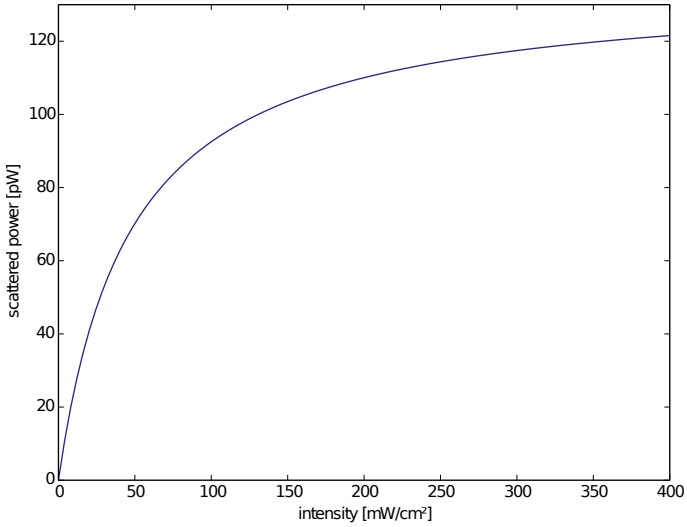

Figure 2.3.: The atoms scatter power as a function of the light intensity they are exposed to, with diminishing returns for increasing the intensity beyond the saturation intensity of the atoms.

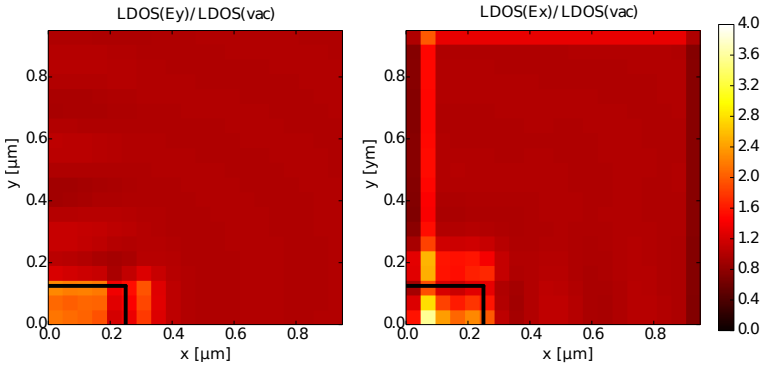

Figure 2.4.: The presence of the nanobeam changes the Local Density Of States (LDOS) of the atoms, influencing their scattering rate. The stripes in the LDOS(E_x) calculations are unphysical, they result from numerical instabilities.

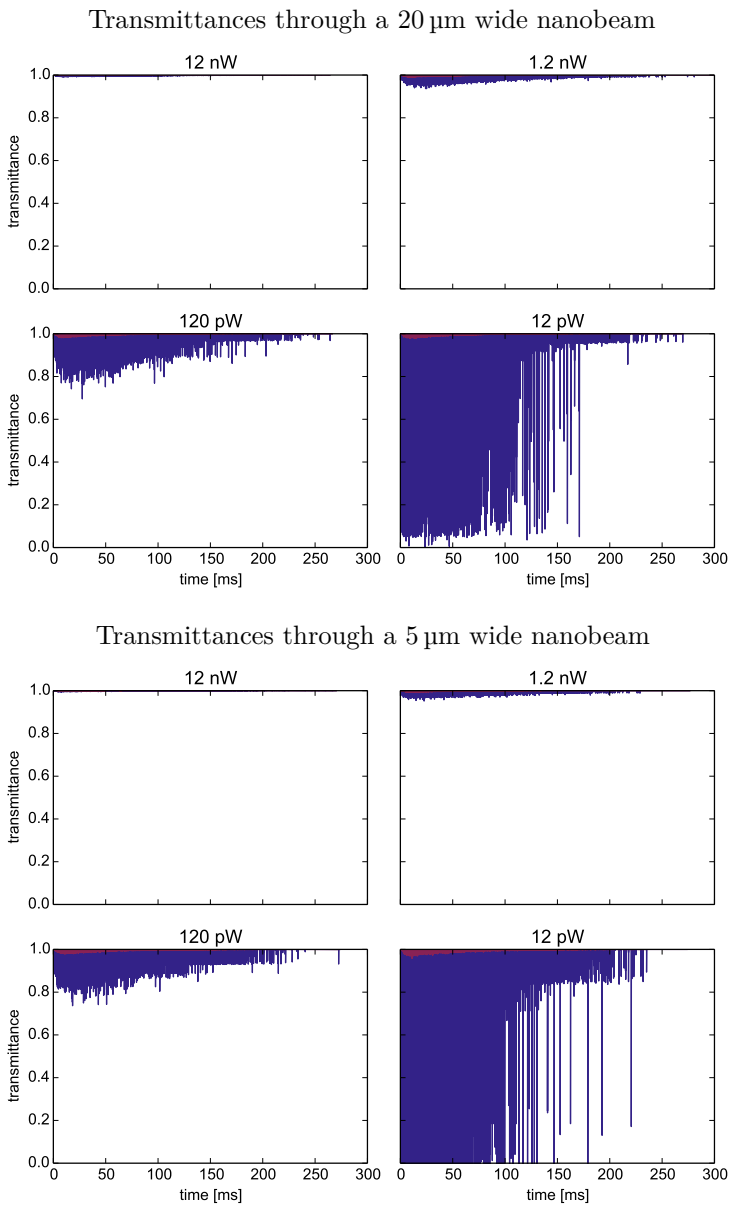

Figure 2.5.: Light transmittances, shown in blue, through nanobeams of various widths and beam powers. The same signal filtered with a lock-in amplifier is shown is violet.

c) Transmittances through a 1 µm wide nanobeam

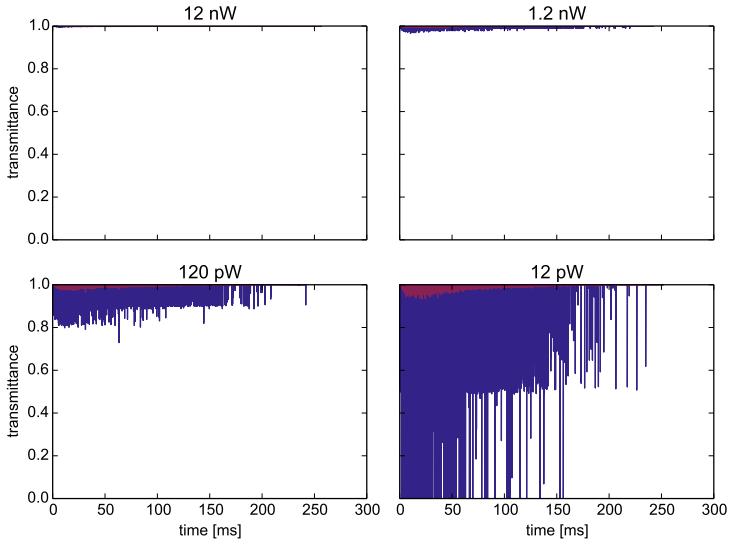

d) Transmittances through a 300 nm wide nanobeam

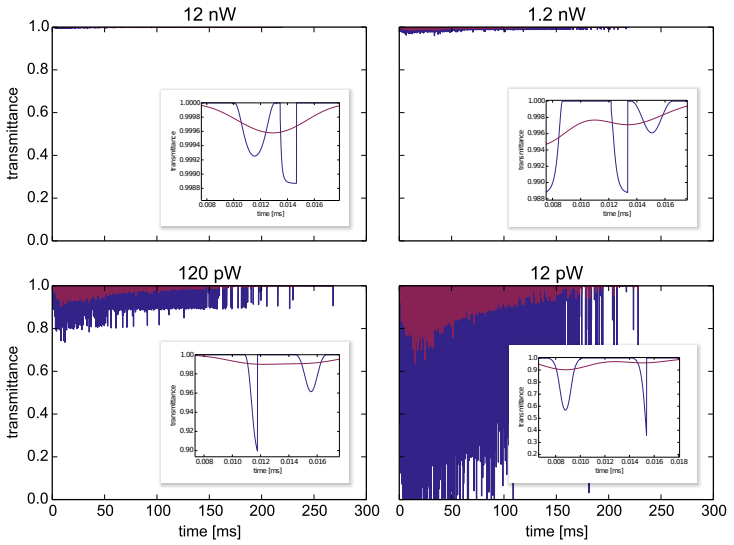

The inset in part **d)** shows the transmittance traces caused by both an atom fly-by (symmetric shape) and a collision event (sharp edge). Note the saturation effects for high light powers.

The wider the nanobeam is, the higher the overall atom number is that can contribute to scattering. But a wider beam also results in a larger mode area and thus the atoms interact with a smaller fraction of the overall field. As a result, smaller beams interact with less atoms, but cause more light to be scattered per atom. The insets in Figure 2.5 **d)** each show an absorption trace of an atom passing the nanobeam and an absorption trace of an atom hitting the nanobeam. For higher beam powers there is less power scattered and the trace has a rectangular shape. This indicates that the atom saturates at high beam powers. At low beam powers this saturation does not occur and the scattering trace follows an inverse exponential.

The highest reduction in transmittance happens at low beam powers. However, at these beam powers the noise of the light detector starts to play a role. There are two approaches to overcome the low signal-to-noise ratio: filtering the signal with a lock-in amplifier and using a photon-counting detector. Figure 2.5 also shows a simulated lock-in filtered signal, plotted in violet. Even with a short integration time of 4 µs the lock-in amplifier cannot capture the individual time traces of the atoms, as shown in the insets of that figure. The resulting signal is much lower.

A power of $P = 12\,\mathrm{pW}$ in the nanobeam corresponds to a photon rate of

$$N = P\ h\ \frac{780\,\mathrm{nm}}{c} \approx 47\,\mu\mathrm{s}^{-1},$$

with h being the Planck constant. Photon-counting detectors are necessary for such a low photon flux. They are readily available as off-the-shelf components.

To estimate the signal strengths of atoms interacting with the evanescent field, we can analyse two atom trajectories. For the following cases we use a light power of 12 pW in the beam.

Direct Hit In this case the atom hits the nanobeam right in the centre and adsorbs to the surface. At the highest intensity the saturation parameter is $s_0 = {}^{I}/_{I_{\mathrm{sat}}} = 0.14$. The atom scatters 6 photons during the interaction time, when on average 58 photons would pass through the

nanobeam. This leads to a signal-to-noise ratio of

$$S/N = 0.8.$$

Grazing Fly-By Here the atom passes next to the nanobeam. The highest saturation parameter is $s_0 = 0.46$, so saturation is barely starting to play a role. The atom scatters 35 photons, while 155 photons would pass through the nanobeam. This leads to a higher signal-to-noise ratio of

$$S/N = 2.8.$$

It is thus in principle possible to detect atom-light interactions at the nanoscale for the very simple system described here.

2.1. Possible Experiments

With a more refined atom transport we could trap atoms in close proximity to the nanostructure. This increases the interaction time significantly and enable a wide range of possible exciting experiments.

Van Oosten and Kuipers proposed to trap single atoms near a photonic crystal nanocavity with a fraction of a photon [vOK11]. Rauschenbeutel et al. trap atoms next to nanofibres by using a combination of red-detuned and blue-detuned light [VRS+10]. Lukin et al. use plasmonic lattices for ultracold atoms [GTC+12], and Slama et al. worked on cooperative coupling of ultracold atoms and surface plasmons [SZS14]. All of these are quite different experiments. And all of these types of experiments are possible in our experimental setup.

2.2. Goal of the Setup

Switching between the above-mentioned experiments only takes a weekend. We can study the interactions of cold atoms and nanostructures with many different approaches, covering multiple interesting topics at the same time and making use of their synergy effects.

3. Experimental Setup

The purpose of the experimental setup is to deliver cold rubidium atoms to a sample surface and record their interaction. While the experimental sequence varies depending on the type of experiment conducted, the process of collecting and delivering the atoms to the sample surface stays the same. This process is the subject of this chapter.

3.1. Overview

Figure 3.1 shows the roadmap that the atoms follow, as well as the roadmap for this chapter. A sealed ampule containing 1 g of rubidium in metallic form is placed in the vacuum chamber. The rubidium has a natural isotope abundances of 72.17 % ^{85}Rb / 27.83 % ^{87}Rb [San06]. At room temperature it is solid — the melting point lies at 39.31 °C — with a vapour pressure of 5×10^{-7} mbar in vacuum [Wie08]. After the final pump-down of the setup, the ampule is broken. The rubidium vapour fills a glass tube, henceforth called 2D chamber. Frequency-stabilized lasers and magnetic fields are used to trap ^{87}Rb atoms in a cigar-shaped two-dimensional magneto-optical trap, abbreviated 2D-MOT. The remaining ^{85}Rb atoms are not affected by the light.

From the 2D chamber the laser-cooled atoms are pushed by a laser through a differential pumping section into the 3D chamber. This differential pumping section allows for a significantly lower pressure in the 3D chamber of 3×10^{-10} mbar and thus a longer lifetime for atom clouds within. In the 3D chamber the rubidium atoms are trapped in a three-dimensional MOT (3D-MOT).

The atoms are then loaded into an optical dipole trap for transportation

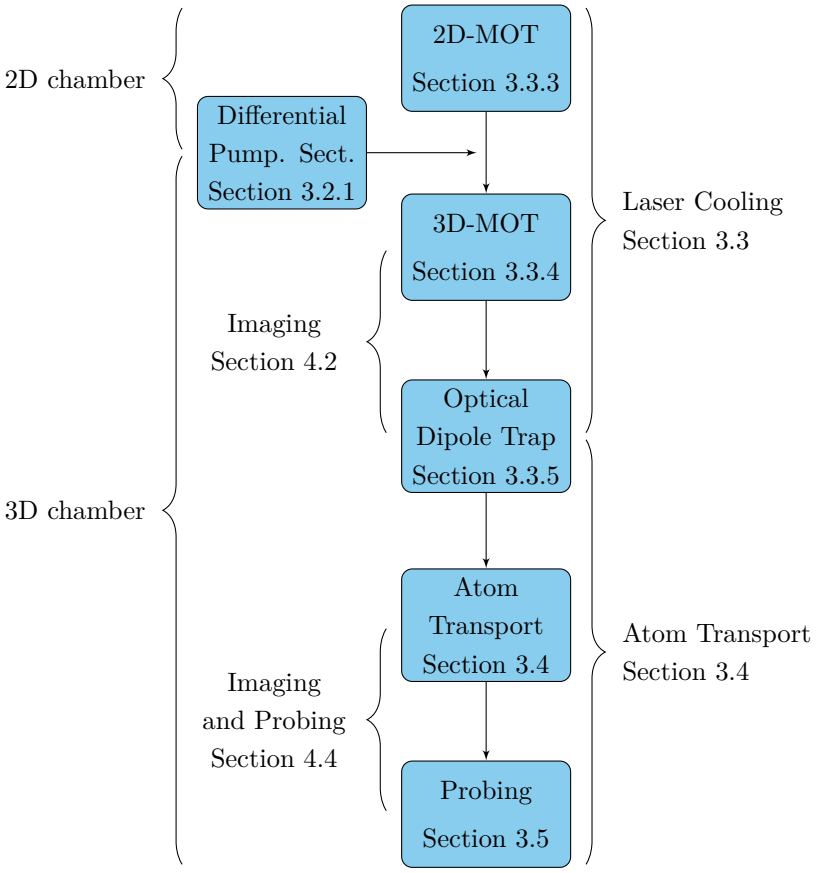

Figure 3.1.: Thematic overview of the experimental setup.

and further cooling. The trap consists of a strong, focused, single-mode Ytterbium fibre laser beam. A mirror mounted on a rotation stage steers the laser, and the atoms trapped inside the beam, from the 3D-MOT to a location above the sample. There the atoms are loaded into a vertical optical lattice. In this final trap stage, the atoms can be moved in three dimensions to position them anywhere above the sample surface.

3.2. Vacuum System

As shown in Figure 3.2, the vacuum chamber consists of three main parts: the 2D chamber, the 3D chamber and the load-lock chamber.

The 2D chamber is used to collect and cool the atoms in a "high" pressure environment of 5×10^{-7} mbar, the vapour pressure of rubidium. From there they are loaded into the 3D chamber through a differential pumping section, as described in Section 3.2.1.

In the 3D chamber the atoms from the 2D-MOT are collected and loaded into a 3D-MOT. Due to the differential pumping section, a lower pressure of 3×10^{-10} mbar can be maintained there, increasing the lifetime of the atom cloud and thus increasing the available time for experiments. They are then further transported to the sample. The interactions of the atoms and the sample are then measured and recorded.

The load-lock chamber is used to quickly exchange samples with minimal disturbance to the vacuum in the 3D chamber. Three samples can be stored in the load-lock chamber. It is held under a vacuum of 5×10^{-9} mbar, which can be reached within a few days of pumping after venting and sample exchange. A large-aperture valve with an opening diameter of 50 mm connects the load-lock chamber to the 3D chamber. After evacuating the load-lock chamber, the valve can be opened for sample exchange. Being only shortly exposed to a pressure which is only about one magnitude higher than the working pressure, the 3D chamber can be evacuated down to a working pressure within hours. A complete cycle like this is usually planned across a weekend, allowing for minimal downtime.

3.2.1. Differential Pumping Section

The differential pumping section (DPS) is a small and narrow round tube connecting the 2D chamber and the 3D chamber. It has an inner radius $R = 0.5$ mm and length $L = 50$ mm. The pressures in the vacuum chambers are $P_{2D} \approx 10^{-7}$ mbar and $P_{3D} = 3 \times 10^{-10}$ mbar. Due to the

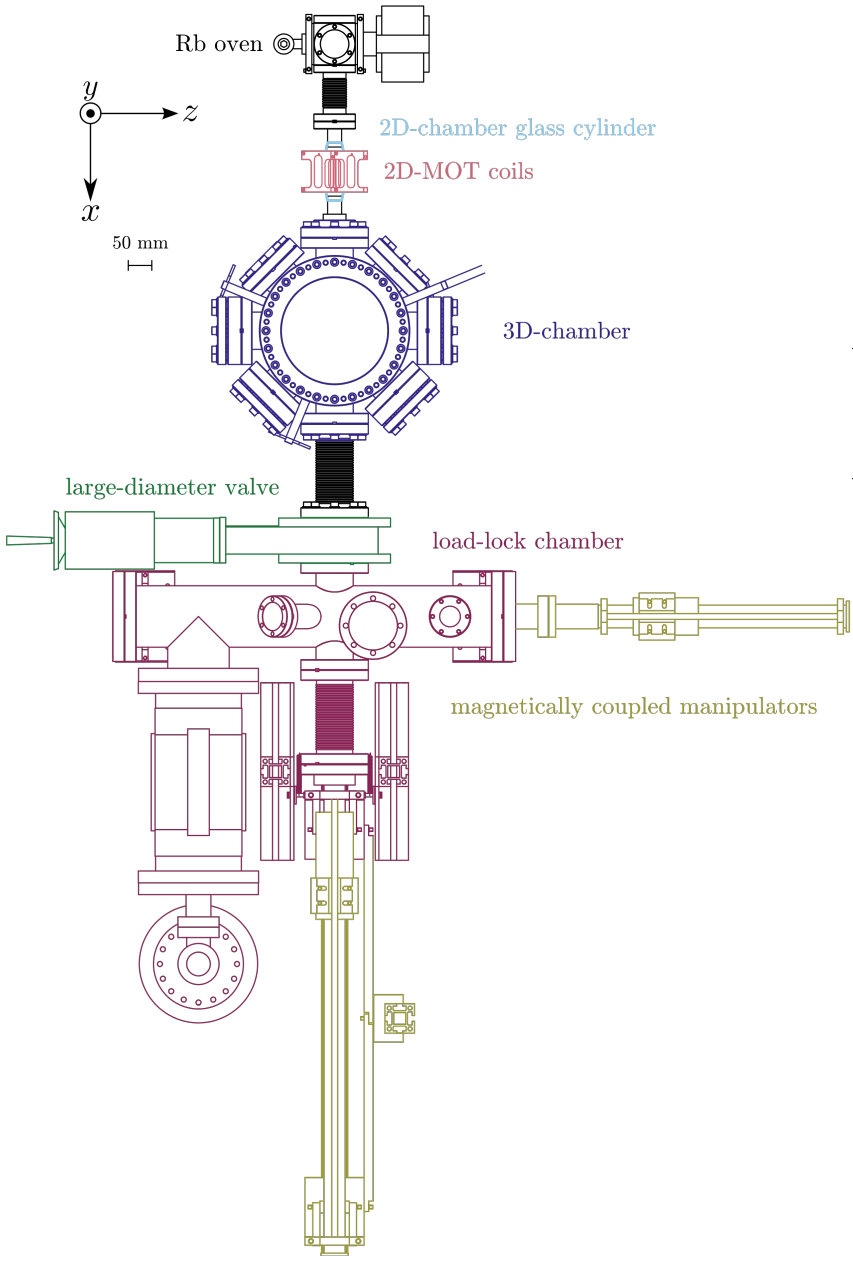

Figure 3.2.: Top view of the vacuum chambers.

nature of free molecular gas flow at low pressures, the DPS is capable of maintaining a high pressure difference between the two chambers.

We can assume constant room temperature of the vacuum chamber and ignore the wall outgassing inside the DPS due to its small surface area. The ideal gas law is

$$pV = Nk_{\mathrm{B}}T = \text{const.}$$

The product of pressure p and volume V is therefore constant before, in, and after the DPS. In vacuum engineering a measure called $Q = \frac{N}{t}k_{\mathrm{B}}T$ for a "quantity" of gas flow is often used to describe elements of a vacuum chamber [Rol67]. At constant temperature, Q is proportional to the mass flow rate $\dot{m} = \frac{N}{t}$ and we can write

$$Q = pV/t,$$

with

$$Qt = pV = \text{const.}$$

The flow rate through an obstruction like a DPS depends on the conductance C of the obstruction and the pressure difference P_Δ across [O'H05], such that

$$Q = CP_\Delta.$$

The conductance of a round pipe with radius R and length L in the limit of $R \ll L$ is [Rol67]

$$C = 0.98 \times 10^{-6}\ \frac{R^3}{L}\ \mathrm{l\,s^{-1}}.$$

Thus the differential pumping section has a conductance of:

$$C_{\mathrm{DPS}} = 0.98 \times 10^{-6}\ \frac{(0.5 \times 10^{-3}\,\mathrm{m})^3}{50 \times 10^{-3}\,\mathrm{m}} = 2.45 \times 10^{-3}\,\mathrm{l\,s^{-1}}.$$

The 3D chamber is pumped by an ion pump with a pumping speed of $S = 50\,\mathrm{l\,s^{-1}}$. The inflow of gas through the differential pumping section is therefore negligible.

Finally, the DPS flow rate Q results to

$$Q \approx 245 \times 10^{-12}\,\mathrm{mbar\,l\,s^{-1}}.$$

3.3. Laser Cooling

In order to study the interactions of atoms with plasmonic structures, it is beneficial to work with cold atoms. The colder the atoms are, the less thermal energy they have, the easier it is to localize them close to the sample. Colder atoms also allow for higher atom densities or higher atom numbers in a trap. The atoms are therefore cooled to ultra-low temperatures using laser cooling.

For cooling, repumping and imaging the D_2 transition hyperfine structure in ^{87}Rb is used. All the lasers that operate close to resonances need to be carefully tuned in wavelength. To this end we use spectroscopy to find the correct rubidium lines and then lock the lasers directly or indirectly to them.

The level scheme of ^{87}Rb, the spectroscopy and the various locking techniques are described in Section 3.3.1. The cascade of traps and cooling stages are discussed in Sections 3.3.2 to 3.3.5.

3.3.1. Frequency Locking

At room temperature $T \approx 300\,\mathrm{K}$, the rubidium atoms have a thermal energy E, which translates to a thermal velocity spread v_{th} with respect to the lab frame. Due to the Doppler effect, this velocity spread has an impact on the spectroscopy. With k_{B} being the Boltzmann constant and $m = 1.42 \times 10^{-25}\,\mathrm{kg}$ being the mass of a rubidium atom, we have

$$E = \frac{3}{2} k_{\mathrm{B}} T = \frac{1}{2} m v_{\mathrm{th}}^2,$$

leading to a speed of

$$v_{\mathrm{th}} = \sqrt{\frac{3 k_{\mathrm{B}} T}{m}} \approx 300\,\mathrm{m\,s^{-1}}.$$

During spectroscopy, this velocity spread leads to a considerable Doppler shift $\Delta f = \frac{v_{\mathrm{th}}}{c_0} f_0$. Here c_0 is the speed of light in vacuum and $f_0 \approx 384\,\mathrm{THz}$ the frequency associated with the D_2 excited state, as depicted in Figure 3.3. We can expect a Doppler shift of the order of

$$\Delta f = \frac{300\,\mathrm{m\,s^{-1}}}{2.997\,92 \times 10^{8}\,\mathrm{m\,s^{-1}}} 384\,\mathrm{THz} \approx 380\,\mathrm{MHz}.$$

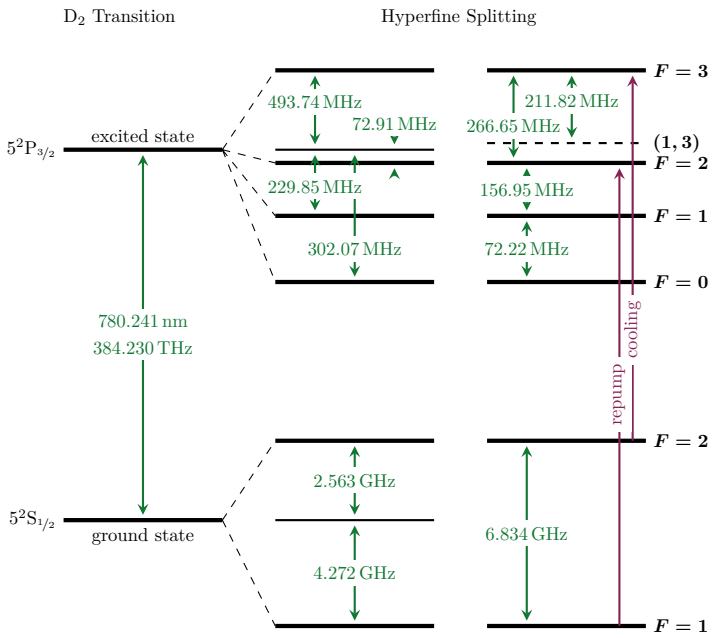

Figure 3.3.: D_2 transition of ^{87}Rb, adapted from [Ste09, BSS+99, YSJH96]

This is considerably larger than the line width of the cooling- or repump-transition, shown in Figure 3.3, of about $\Gamma = 2\pi \cdot 6\,\mathrm{MHz}$ [VS96]. The ground state hyperfine splitting as well as the isotopes ^{85}Rb and ^{87}Rb can be resolved, but the resolution is not good enough to lock the lasers for cooling and trapping. The spectrum in Figure 3.4 shows that the hyperfine structure is drowned in Doppler broadening.

To eliminate the Doppler shift, we use saturated absorption spectroscopy, a pump-probe scheme, developed by Schawlow and Hänsch in the early 70s [Pre96]. The atomic resonances appear as dips in the saturated absorption spectrum. As an error signal, this is impractical: if the laser drifts away from resonance, the error signal increases. We do not know, however, if the laser frequency is too high or to low. As an error signal,

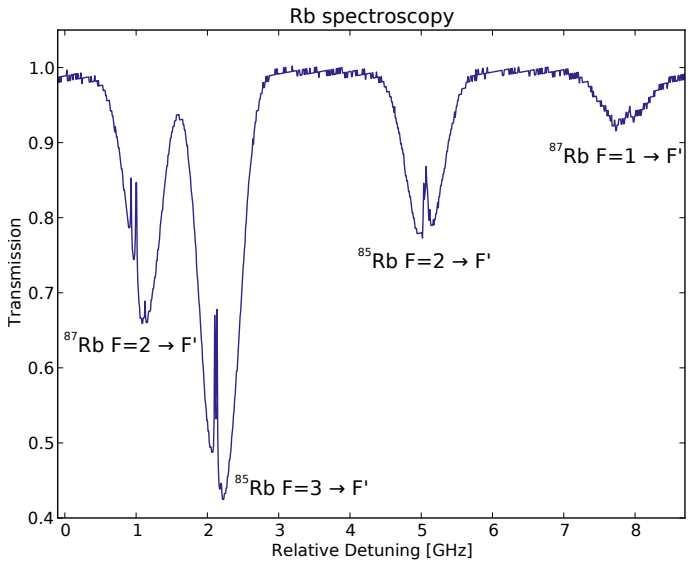

Figure 3.4.: Doppler Free Rb Spectroscopy. Plotted is the transmission signal from the photodiode of the Pound-Drever-Hall setup depicted in Figure 3.5. Narrow features of the hyperfine lines are visible inside four broad Doppler broadened dips.

we need a slope to lock on, not a dip. Consequently, the *derivative* of the saturated absorption signal is a good error signal to lock on.

To this end, we extend the saturated absorption spectroscopy to Wavelength Modulation (WM) spectroscopy, a technique to transform an absorption signal into a slope suitable to lock on [BSS92]. Figure 3.5 shows the spectroscopy setup including the electronics involved. A local oscillator running at 250 kHz dithers the laser diode current. The dithering frequency and amplitude are small compared to the laser line width. The output from the photodiode is input into a lock-in amplifier, where it is mixed with the local oscillator signal and subsequently low-pass filtered. This process filters the photodiode output for signals with the local oscillator frequency. Photodiode signals in-phase with the local oscillator

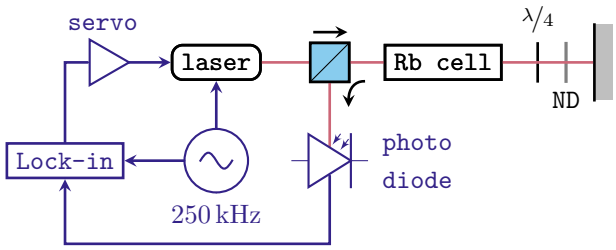

Figure 3.5.: Schematic view of the Pound-Drever-Hall WM spectroscopy, including the electronics involved. A local oscillator dithers the laser frequency at 250 kHz. A lock-in amplifier turns the spectroscopy signal into a locking signal.

creates a positive output of the lock-in amplifier, while out-of-phase signals create a negative output. A subsequent servo amplifier amplifies the lock-in output and, depending on the laser control scheme, inverts it if necessary.

Figure 3.6 illustrates the detection of the locking signal. When the laser frequency is right at an absorption line, the signal is the lowest. Any small deviation in frequency causes higher absorption of the rubidium gas. When the laser frequency is dithered, the laser scans across the absorption signal. If the laser has a slightly too low frequency, it scans across a strong, negative slope. This causes a strong out-of-phase signal on the photodiode and a strong, negative output of the lock-in amplifier. When lasing right on the resonance frequency of the absorption line, the laser scans across the bottom of the dip. The photodiode detects a low signal at twice the oscillator frequency. This signal is filtered out by the lock-in amplifier, resulting in zero output. At a slightly too high frequency, the laser scans across a strong positive slope, causing a strong positive signal after the lock-in amplifier. With a low dithering amplitude, the output of the lock-in amplifier approaches the derivative of the absorption signal. This provides a slope and zero crossing to lock on. Figure 3.7 shows this so called error signal for ^{85}Rb and ^{87}Rb.

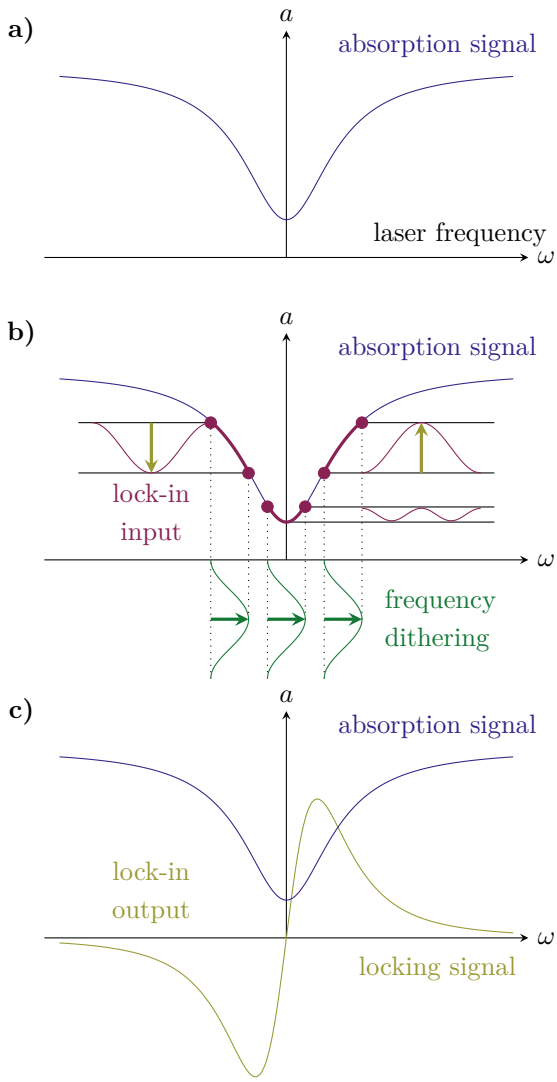

Figure 3.6.: WM spectroscopy principle. **a)** Photodiode absorption dip, in blue. **b)** Laser frequency dithering (green) causes modulations in the absorption signal, depicted in violet. **c)** A lock-in amplifier transforms these into a locking signal, plotted in olive.

Offset Locking

The previously described WM spectroscopy is suitable for locking onto or very close to an atomic transition. To operate a MOT, the laser has to be locked at a *variable offset* with respect to atomic transitions. To this end, we need a stable reference: a laser that is locked on the transition in question. Furthermore, we need a system to lock the MOT cooling laser to a frequency difference from that reference laser.

The schematics of the offset lock is depicted in Figure 3.8. The laser-to-be-locked is overlapped with a reference laser. A fast photodiode detects the beating signal containing the difference frequency. The sum frequency is in the several-hundred-THz range, which is much too high for the photodiode to detect. The photodiode signal is split in two. One output is used as a monitor; it is fed to a frequency counter that displays the offset between the two lasers. The other output is mixed with an RF signal generated by a Direct Digital Synthesiser (DDS). The resulting beat signal is low-pass filtered to suppress the electronic sum signal and keep the electronic difference signal which is then subsequently amplified. A combination of a splitter and a mixer acts as an interferometer for the electronic signal. The different path lengths of the two arms of the interferometer cause a frequency-dependent phase difference of the signals. A scanning laser causes fringes in the signal after the mixer, just as light transmission through a Mach-Zehnder interferometer would. Changing the output of the DDS changes the positions of the fringes as well, making it possible to change the frequency of the laser while it is in lock.

3.3.2. MOT Lasers and Probe Light

The diode lasers are low-cost laser diodes that are set up with a grating in Littrow configuration, a practical and compact technique to stabilize the frequency [Trä12]. The layout is sketched in Figure 3.9. Light from a laser diode is collimated by a lens and reflected off a grating. The first grating order is reflected back into the diode as optical feedback. The zeroth order is coupled out as usable laser light. A set screw changing

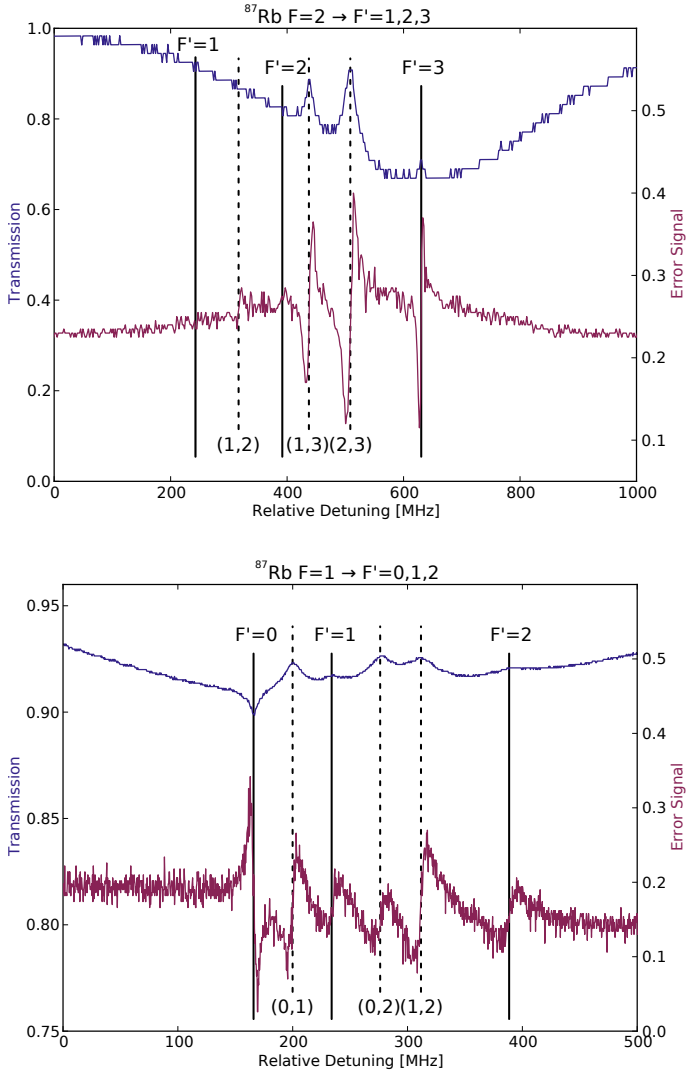

Figure 3.7.: Plotted in blue are the transmission-signals from the Pound-Drever-Hall WM spectroscopy of ^{87}Rb. The derived error signals are shown in violet. Solid lines show the hyperfine

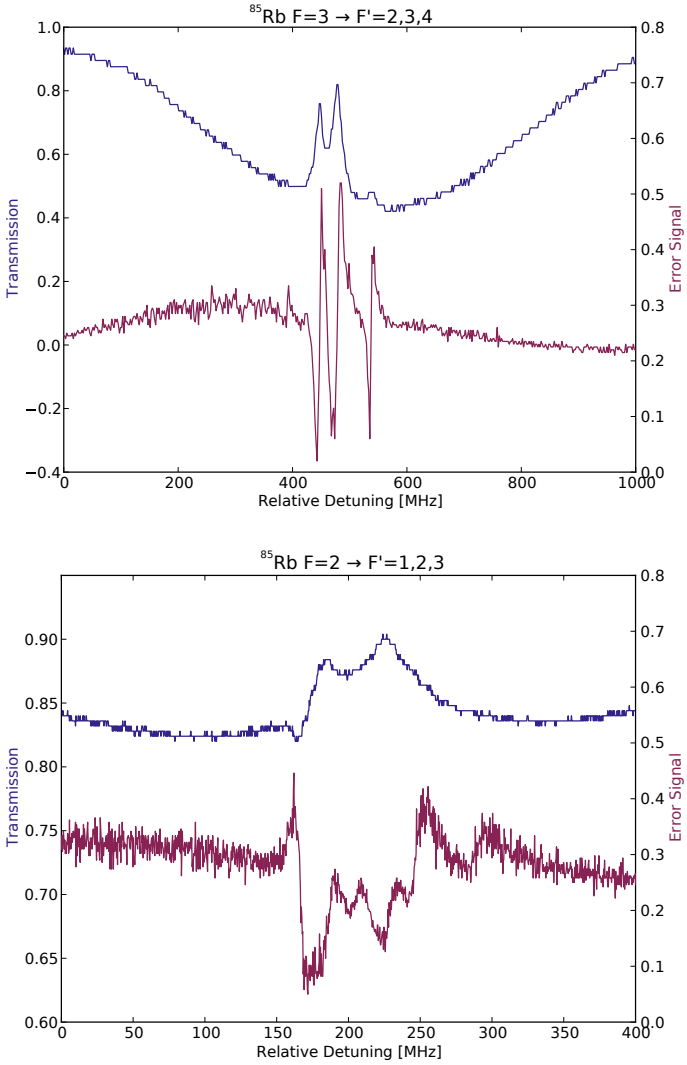

lines, whereas dashed lines indicate the crossovers. The spectra of ^{85}Rb are included for visual reference.

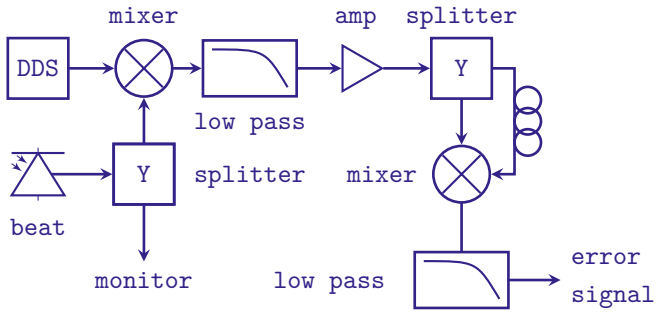

Figure 3.8.: Laser Offset Locking. The beating signal of two lasers is mixed with an RF output from a DDS. An electronic Mach-Zehnder interferometer provides a DC error signal, depending on the frequency of the mixed signal.

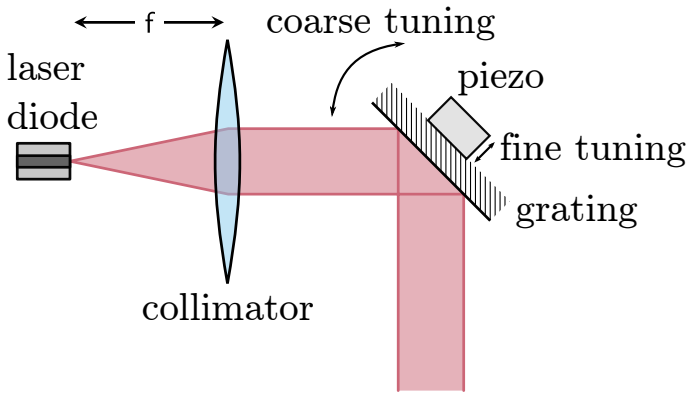

Figure 3.9.: Schematics of a laser in Littrow configuration. A laser diode emits a diverging laser beam that is collimated by a lens. A grating forms a cavity with the diode and can be tilted for wavelength tuning.

position and angle of the grating provides coarse frequency tuning, while a piezo is used for the fine tuning. Mode-hop-free single-mode scanning can be achieved by modulating the grating position simultaneously with the diode current.

Five different lasers provide the light for the MOTs and probing. Figure 3.10 shows the setup layout. An overview over the rubidium level scheme can be found in Figure 3.3.

Reference Laser The reference laser is locked to the $F = 2 \rightarrow F' = (1/3)$ crossover. It is split several times. One beam is sent to spectroscopy. Two other beams are used for probing in two different locations: the MOT location at the centre of the chamber and at the sample position. See Figure 3.16 for references. Two AOMs (Acousto-Optical Modulators) in each path are used to control the amplitude of the light. The laser light in each path is coupled into separate fibres.

The same laser is also used as a reference for offset locking the 2D- and 3D-MOT cooling light. The beat signal of the MOT beams and the reference beam is used to generate an error signal for locking as described in Section 3.3.1.

2D-MOT Repump Laser The 2D-MOT repump laser is overlapped with the 2D-MOT cooling light and coupled into a single fibre. A part of the beam is split off for spectroscopy. The laser is locked to the $F = 1 \rightarrow F' = 2$ transition.

2D-MOT Cooling Laser Cooling light for the 2D-MOT comes from the 2D-MOT cooling laser. Parts of it are split off for spectroscopy and offset locking with the reference laser. The cooling light is amplified in a tapered amplifier, overlapped with the repump light and coupled into a fibre.

3D-MOT Repump Light The 3D-MOT repump light is locked to the $F = 1 \rightarrow F' = (1/2)$ crossover and shifted with an AOM to the $F = 1 \rightarrow F' = 2$ transition 78.475 MHz away. The AOM is used to control the

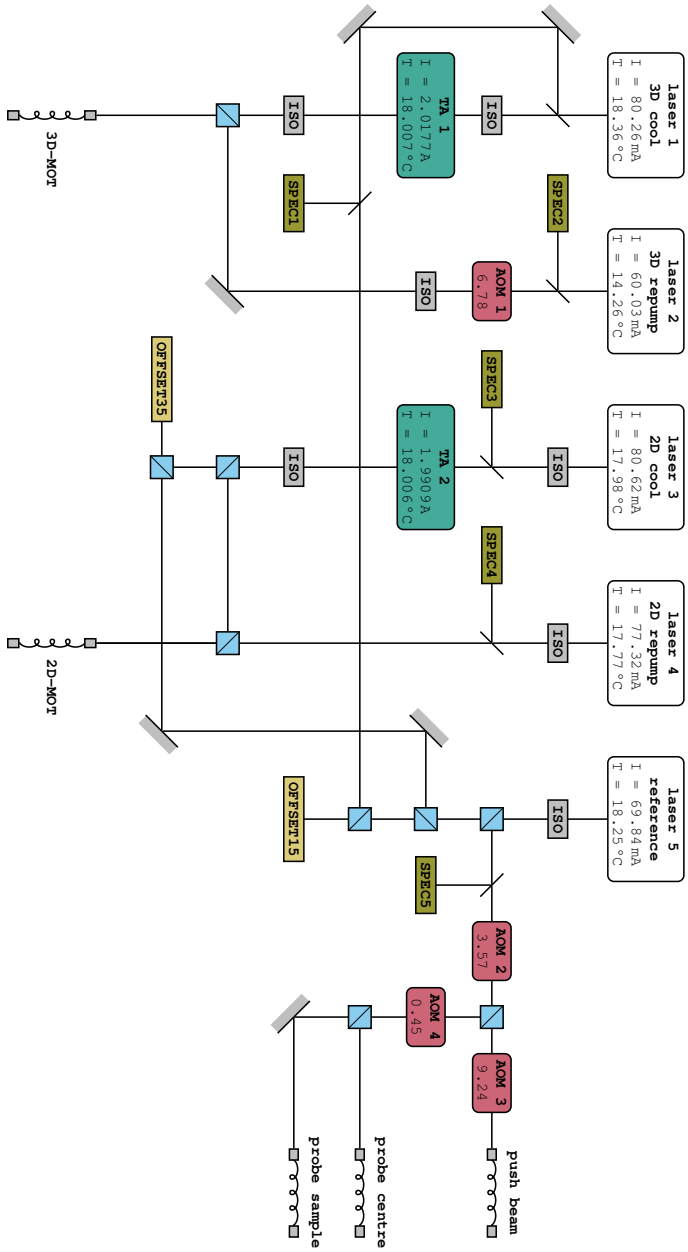

Figure 3.10.: Layout of the laser table.

amplitude of the light. It is then overlapped with the cooling light and coupled into a fibre.

3D-MOT Cooling Light Finally, parts of the 3D-MOT cooling light are sent to spectroscopy and offset locking. The rest is amplified in a tapered amplifier and coupled into a fibre.

3.3.3. 2D-MOT

The 2D-MOT is a four-beam MOT. Since the advent of the magneto-optical trap, it has been used as cold atom sources in numerous experiments [RPC+87, CKM+90, DSWW98]. The magnetic field is provided by four coils in the shape of rounded rectangles — often called race-track coils — to match the desired cigar shape of the atomic cloud in the 2D-MOT. Two opposing coils are each oriented in anti-Helmholtz configuration. They each have 81 windings with a wire cross section of $1\,\text{mm} \times 1.5\,\text{mm}$. Their inner dimensions are 27 mm and 77 mm, and their outer dimensions are 45 mm and 95 mm. Opposing coils are placed at a distance of 54 mm to each other and carry a current of 1.96 A, leading to a gradient of 7.43 G/cm in the centre. To shield the nearby optics from the dissipated power of 7.25 W, the coil holders are internally water cooled. Figure 3.11 shows a sketch of the holders and their assembly.

To match the 2D-MOT shape, the four laser beams for the MOT are elliptical Gaussian beams with beam waists of 31.5 mm and 97.5 mm, respectively. The beams are circularly polarized and have a power of 30 mW each.

With the use of a push beam, the 2D-MOT provides an atom flux of up to 4.4×10^9 atoms/s, measured at the 3D-MOT position. The 2D-MOT thus provides a high atom flux while staying very compact, measuring only 40 cm in length.

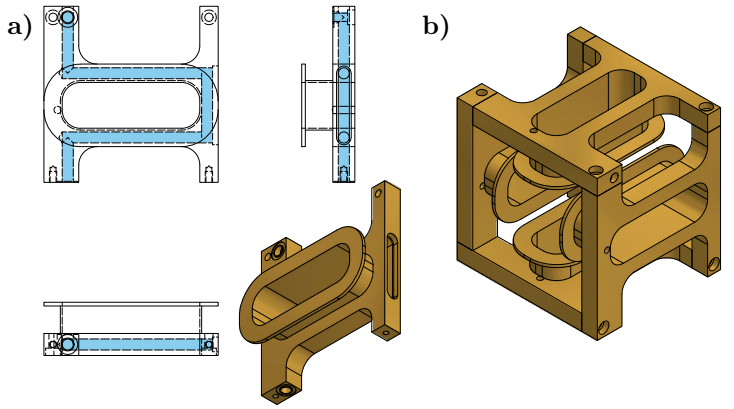

Figure 3.11.: Internally water-cooled 2D-MOT coil holder. **a)** A water channel is routed into each brass coil holder. **b)** Four coil holders are combined into a cage that encloses the 2D chamber.

3.3.4. 3D-MOT

The 3D-MOT is set up in a classic six-beam configuration. Two coils in anti-Helmholtz orientation enclose the vacuum chamber. They have 195 windings each, with a wire cross section of 1 mm × 4 mm. The coils have a length of 60 mm with an inner diameter of 255 mm and an outer diameter of 283 mm. They are mounted at a distance of 178 mm from centre to centre. Figure 3.12 provides references of orientation. With a current of 19.3 A, the coils create in the centre of the chamber a gradient of 17.3 G/cm in the y-direction. The coils dissipate a total of 612 W and thus need to be water cooled: a copper sheet with soldered-on copper tubing surrounds the coils.

Three orthogonal laser beam pairs enter the vacuum chamber. They are circular Gaussian beams with beam waists of 12.6 mm. Their polarization is circular and they each have a power of 14 mW.

Compensation Coils

The diameter of the 3D-MOT coils is comparable to the distance between the 2D and 3D chambers. The 3D-MOT coils thus cause a considerable magnetic field gradient in the x-direction inside the 2D-MOT glass cylinder and a non-constant Zeeman-shift of the rubidium atoms along the axial direction of the 2D-MOT. As a result, the efficiency of the 2D-MOT would be severely reduced.

Compensation coils are used to overcome this. A single coil would be sufficient to keep the magnetic field inside the 2D-MOT low, but it would also move the magnetic zero inside the 3D chamber by about 1 cm. Two compensation coils are therefore installed. They compensate for the field of the 3D-MOT coils at the 2D-MOT position while having only a minor influence on the magnetic zero on the 3D-MOT. Their position and the resulting magnetic fields are shown in Figure 3.12.

Both coils consist of 16 layers of ribbon cables that are 20 wires wide. This results in a total wire count of 320 wires per compensation coil. The smaller one, placed between the 3D chamber and 2D chamber, has a coil radius of about 100 mm and is placed 175 mm away from the centre of the 3D chamber. This coil mostly compensates the 3D-coil field inside the 2D chamber. The bigger coil has a radius of about 135 mm and is placed on the opposite side, 210 mm away from the 3D chamber centre. This coil mainly compensates for the small-coil magnetic field inside the 3D chamber.

With the compensation coils, the field zero of the 3D-MOT is only moved by 350 µm and the field gradient inside the 2D-MOT is reduced from 3 G/cm to 0.2 G/cm, which is low enough to not significantly impede the functioning of the 2D-MOT.

3.3.5. Optical Dipole Trap

After being collected and cooled in the 3D-MOT, the rubidium atoms are loaded into the far-off-resonance Optical Dipole Trap (ODT). The atoms inside are transported close to the sample and undergo further cooling.

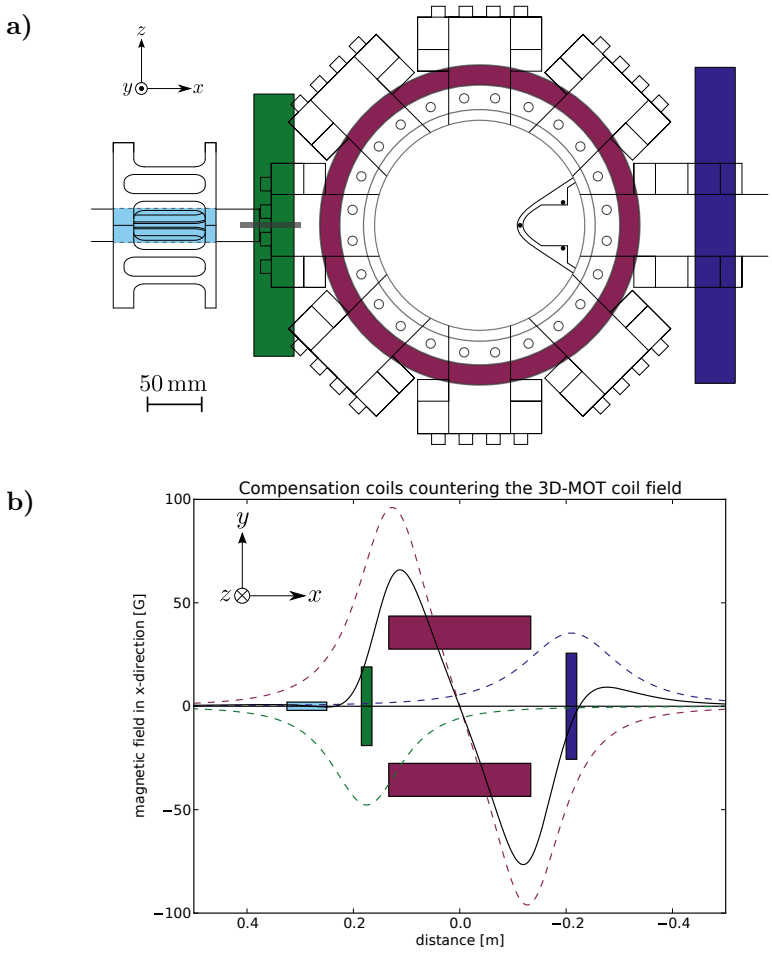

Figure 3.12.: Compensation of magnetic fields inside the 2D-MOT. **a)** Coil configuration around the 3D chamber. **b)** Simulation of the magnetic fields. The 3D-MOT coils, depicted in violet, create a magnetic field gradient inside the 2D-MOT, depicted in light blue. The two compensation-coils, shown in green and dark blue, respectively, greatly reduce this field gradient. The solid black graph is the sum of the fields of the individual coils (dashed).

To be far-off-resonance and still maintain a deep trap, the laser needs to be of high power. For this reason a diode-pumped Ytterbium-fibre-laser is used. Yb^{3+} ions have a simple energy structure with small quantum defect that allows for a high energy efficiency [Dua08]. The laser used has 20 W output power with a wall-plug efficiency of >20 % and a wavelength centred around 1070 nm [Gap09].

The optics for the ODT are set up on two stacked layers. The first level is depicted in Figure 3.13, the second level is shown in Figure 3.14. The laser light first passes an AOM for amplitude control. The zeroth order is not in use right now. It passes a second AOM that can be used for power control of a secondary beam for the dipole trap.

The first order continues to move to the second level above through a closely spaced pair of $f_1 = -200\,\text{mm}$ and $f_2 = 200\,\text{mm}$ meniscus lenses. Together they act as a lens with variable focal length, tunable by the distance between the lenses, to counter a slight beam divergence.

A cylindrical telescope using $f_3 = -400\,\text{mm}$ and $f_4 = 700\,\text{mm}$ lenses and a telescope using $f_5 = 50\,\text{mm}$ and $f_6 = 200\,\text{mm}$ lenses modify the beam waist to be $w_\text{s} = 7.7\,\text{mm}$ and $w_\text{p} = 4.4\,\text{mm}$ before being focused into the 3D chamber with an $f_7 = 400\,\text{mm}$ focusing lens. The last mirror before the focusing lens is mounted on a rotation stage for beam steering. This is described in more detail in Section 3.4.1.

The shape of the trap is shown in Figure 3.15. The remaining beam power inside the vacuum chamber is $P_\text{dip} = 15\,\text{W}$ and the elliptical beam focus has beam waists of $w_{0,\text{x}} = 23.5\,\mu\text{m}$ and $w_{0,\text{y}} = 40\,\mu\text{m}$. This results in a trap depth of $T_\text{dip} = -1.49\,\text{mK}$. The trap parameters as well as the trap frequencies are summarized in Table 3.1.

3.4. Atom Transport

Until the atoms arrive on the sample surface, they undergo a cascade of different traps. From the 3D-MOT the atoms are loaded into the dipole trap. The laser beam of the dipole trap is moved over to the sample, where the atoms are transferred into a one-dimensional optical lattice.

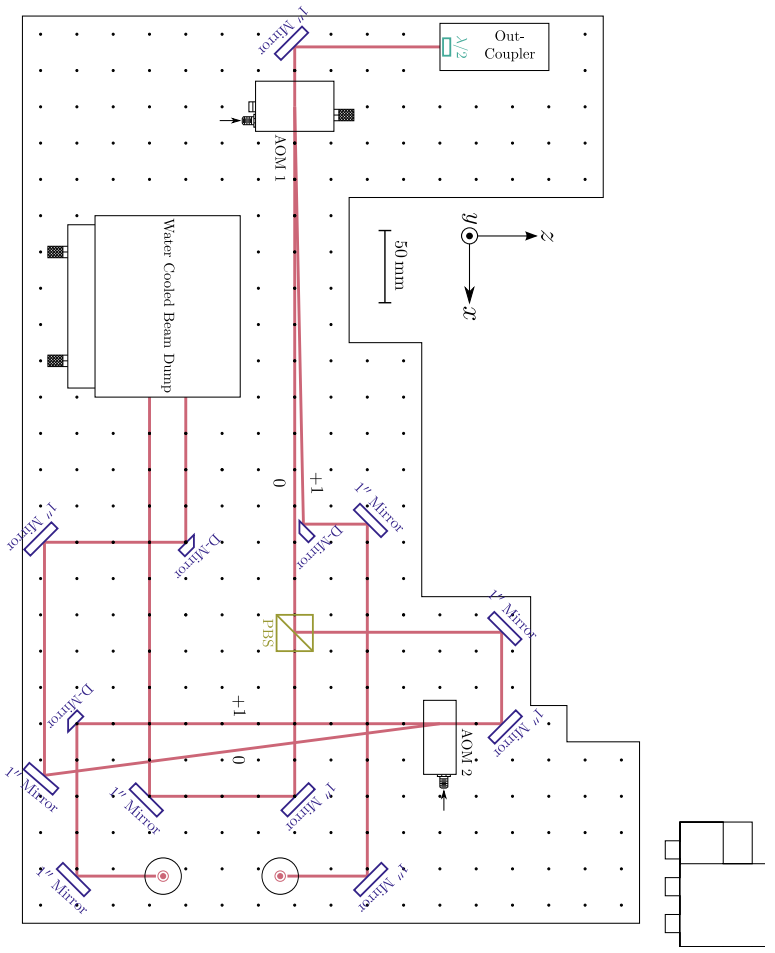

Figure 3.13.: First level of the ODT. The amplitude of the laser light is controlled by an AOM. The first AOM order is sent upwards to the second level, shown in Figure 3.14. The power of the zeroth AOM order is dissipated in a beam dump.

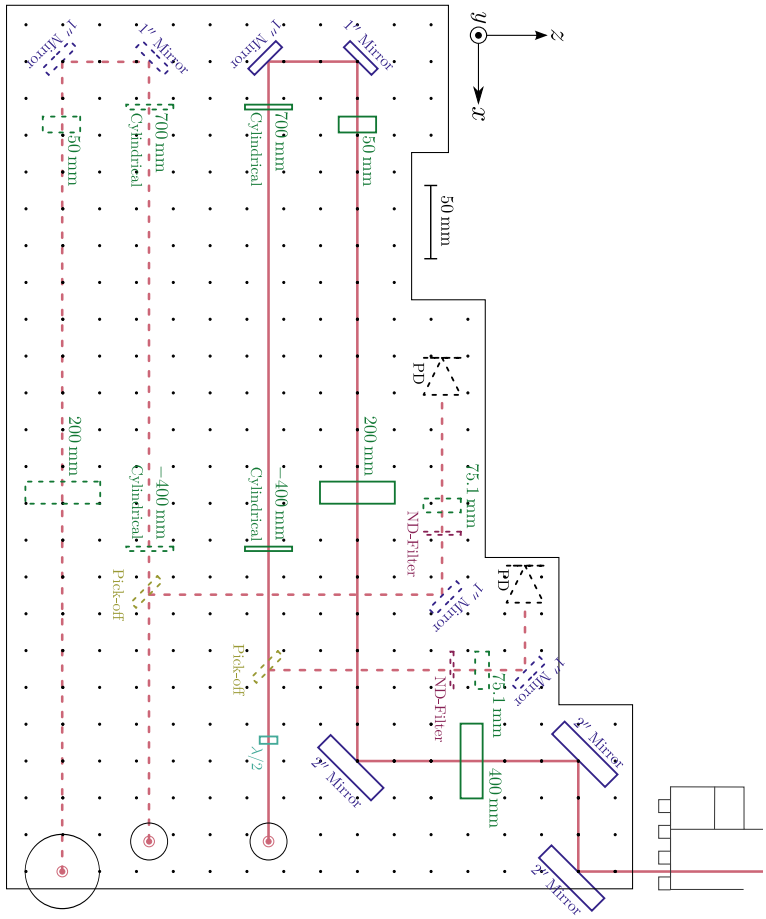

Figure 3.14.: Second level of the ODT. A cylindrical and a normal telescope are used to shape the beam. A lens with focal length of $f_7 = 400\,\mathrm{mm}$ focuses the beam into the vacuum chamber. The last mirror is mounted on a rotation stage for beam steering.

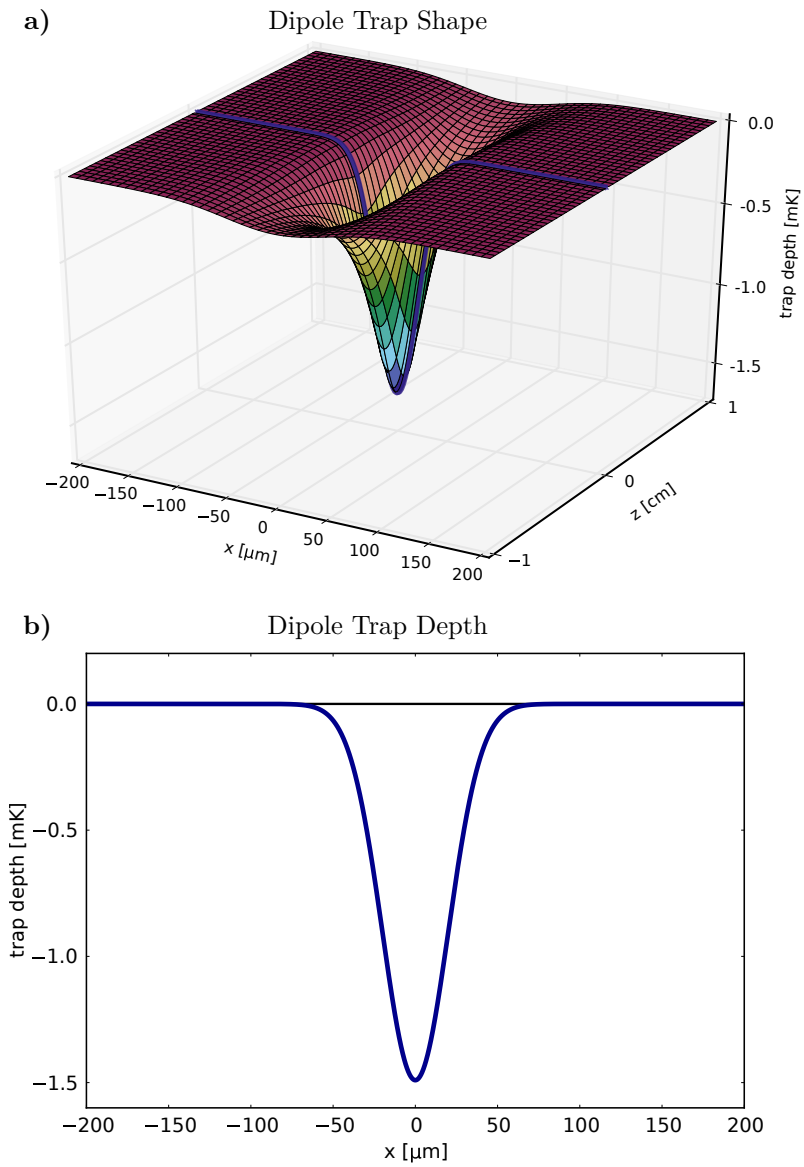

Figure 3.15.: **a)** Potential landscape in the horizontal plane. **b)** Cross section of the x-plane: the tight, horizontal direction.

centre wavelength	λ	1070 nm
centre frequency	ω	280 THz
detuning	$\Delta\omega$	104 THz
natural line width	γ	$2\pi \cdot 6.065$ MHz
beam waist x	$w_{0,x}$	40 µm
beam waist y	$w_{0,y}$	23.5 µm

Table 3.1.: Specifications of the optical dipole trap. A typical beam power of 15.0 W results in a trap depth of -1.49 mK and trap frequencies of $\omega_x = 3.01$ kHz and $\omega_y = 5.08$ kHz in the radial direction and $\omega_z = 39.3$ Hz in the longitudinal direction.

This lattice can move in three dimensions to deliver the atoms to the sample surface and steer the atom cloud towards a sample site.

3.4.1. Dipole Beam Steering: Offset Rotation

To transport the atoms from the centre of the chamber towards the sample, the last mirror of the ODT setup is mounted on a rotation stage*, as mentioned in Section 3.3.5. The starting and target positions, however, do not have the same distance from the mirror. To compensate for this mismatch in distance, the mirror is mounted off-centre with respect to the rotation axis, as depicted in Figure 3.16. The beam focus is both rotated and displaced to reach the centre of the 3D chamber as well as the sample position. The focus effectively follows a circle with a large radius; its centre lies far outside the setup.

A TTL (Transistor-Transistor Logic) signal to the controller of the rotation stage triggers the motion. The stage has a feedback mechanism to ensure a rotational precision of ±24 µrad. The trajectory is thus not deterministic and we have to wait a few milliseconds before the experiment continues to ensure the arrival of the atoms in the beam.

* Physik Instrumente U-651.04

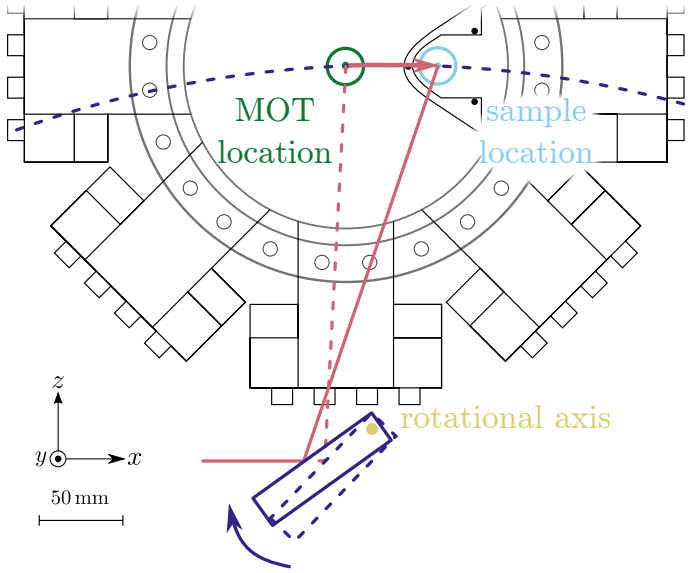

Figure 3.16.: Off-axis mirror rotation for beam steering. The focus of the dipole trap beam, shown in pink, is displaced from the green MOT location to the light blue sample location, along a dark blue, dashed trajectory.

3.4.2. Lattice

The lattice lasers are a commercial off-the-shelf product*. They follow the same operation principle as the MOT diode lasers that are discussed in the Section 3.3.2. To achieve a higher output power, the laser light is subsequently amplified in a tapered amplifier.

The fine positioning of the atoms is done by moving an optical lattice. The motion can be decomposed to a vertical component, and motion in the horizontal plane.

The vertical movement is achieved through moving the optical lattice by detuning the two lattice laser beams with respect to each other. We refer to the part of the setup that achieves this as the *elevator*.

* Toptica Photonics TA pro

After the frequency difference is imprinted, the beams pass through an optical setup that collinearly displaces the beam pair in the horizontal plane. We refer to this part of the setup as the *scanner*.

Elevator

As mentioned above, the elevator is set in motion by imposing a frequency difference Δf between the vertical lattice beams. The speed v_e with which the elevator travels is determined by the centre wavelength of the beams λ_c and the time $T_{\text{beat}} = 1/\Delta f$ that it takes for one cycle of the beat. The beat pattern moves a distance of λ_c in the time of one beat cycle T_{beat} with a velocity of

$$v_e = \frac{\lambda_c}{T_{\text{beat}}} = \lambda_c \cdot \Delta f.$$

The lattice lasers are operating about half a nanometer detuned from the D_2 transition of ^{87}Rb at a centre wavelength of $\lambda_c = 780.525\,\text{nm}$.

The setup is depicted in Figure 3.17. First the laser beam passes a telescope to match the mode profile of the fibre/coupler combination. A subsequent optical isolator ensures no light gets reflected back into the tapered amplifier since this would cause instability or might even destroy the semiconductor. A following rubidium cell of 100 mm length is heated to 120 °C to increase the partial vapour pressure inside. The rubidium atoms in the cell absorb the on-resonant spectral components of the amplified spontaneous emission light that the tapered amplifier emits.

A combination of a $\lambda/2$-waveplate and a Polarizing Beam Splitter (PBS) cube then separates the beam into top and bottom beam of the lattice. Both beams then pass their respective AOMs in a double pass configuration; the first AOM orders are focused by a lens onto retro-reflecting mirrors. This way the angle differences imposed by the AOMs are translated into mere beam displacements. The retro-reflected beams are always collinear to the incoming beams, regardless of AOM frequencies and deflection angles. Irises block the zeroth orders before the mirrors. The beams pick up frequency shifts of twice their respective AOM frequencies. The RF frequencies for the AOMs are generated by a DDS (Direct Digital Synthesizer).

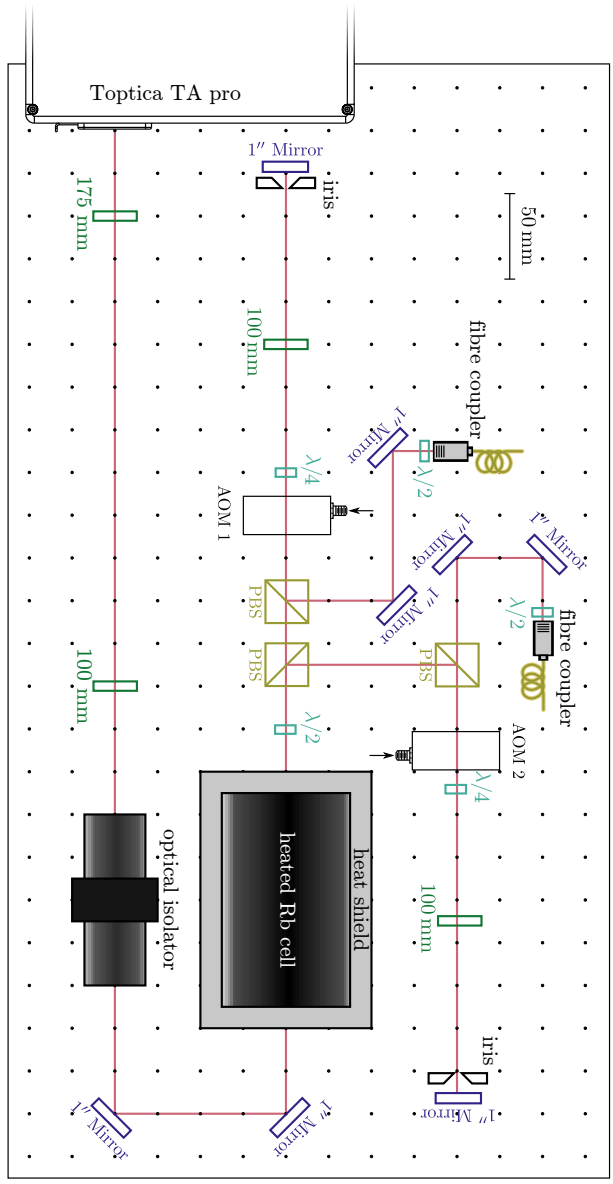

Figure 3.17.: Layout of the lattice laser table. Two double-pass AOM setups provide frequency control for the top and bottom beam.

The outgoing beams are then separated from the incoming beams by a combination of $\lambda/4$-waveplates and PBSs. Upon passing the waveplates twice, the polarizations change from linear to circular back to linear but turned 90° with respect to the incident polarization. The PBSs thus separate them from the incoming beams. Two mirrors are then used to couple the light into their respective polarization-maintaining fibres, while $\lambda/2$-waveplates ensure that the light polarization matches the birefringence axis of their fibre.

On the experimental table, the light from the fibres is coupled out again. Both beams pass through their respective arms of the scanner, before meeting in the centre of the vacuum chamber and forming a lattice. The lattice motion imprinted by different AOM frequencies is preserved in this process.

Table 3.2 lists the lattice parameters and Figure 3.18 shows a two-dimensional cross cut of the trap potential. The trap potential and scattering rate of the lattice are given by [GWO99]

$$U_{\mathrm{dip}}(r) = -\frac{3\pi c^2}{2\omega_0^3}\left(\frac{\Gamma}{\omega_0-\omega}+\frac{\Gamma}{\omega_0+\omega}\right) I(r) \tag{3.1}$$

and

$$\Gamma_{\mathrm{sc}}(r) = -\frac{3\pi c^2}{2\hbar\omega_0^3}\left(\frac{\omega}{\omega_0}\right)^3\left(\frac{\Gamma}{\omega_0-\omega}+\frac{\Gamma}{\omega_0+\omega}\right) I(r). \tag{3.2}$$

Scanner

The scanner moves the beam pair of the optical lattice collinearly in the horizontal plane. It consists of a cascade of $4f$-telescopes with mirror galvanometers or "galvo mirrors" in the imaging planes. These mirrors are rotatable; a servo system keeps the mirrors at an angle that is linearly proportional to the applied voltage.

A single lens can be used for $1:1$ imaging. When the object is twice the focal length f away from the lens, an image with the same dimensions appears also at $2\cdot f$ distance on the other side of the lens. Beam divergence or direction, however, is not preserved. A $4f$-telescope can be

centre wavelength	λ	$780.6368 \pm 0.0012\,\mathrm{nm}$
centre frequency	ω	$384.0358 \pm 0.0003\,\mathrm{THz}$
detuning	$\Delta\omega$	$192.3 \pm 0.3\,\mathrm{GHz}$
natural line width	γ	$2\pi \cdot 6.065\,\mathrm{MHz}$
beam waist	w_0	$33.0 \pm 0.3\,\mu\mathrm{m}$

Table 3.2.: Specifications of the optical lattice. Typical beam powers of $2{\cdot}50\,\mathrm{mW}$ result in a trap depth of $-7.9\,\mathrm{mK}$ and trap frequencies of $\omega_{x,z} = 8.4\,\mathrm{kHz}$ in the radial direction and $\omega_y = 789\,\mathrm{kHz}$ in the longitudinal direction.

used to overcome this, as depicted in Figure 3.19. An object at distance f to the first lens is imaged at distance f from the second lens. Except for mirroring, the object as well as beam divergences and directions are preserved.

The $4f$-telescopes are used to project the two mirror galvanometers onto each other. The rotation axes of these galvo mirrors are perpendicular to be able to scan the beam in two dimensions independently.

The final lens of each arm is then used to translate the angular differences into a displacement on the sample. The beam always impinges perpendicularly on the sample surface. A scanning of the mirror galvanometers thus translates into a horizontal displacement of the beams. The beams of both arms oppose each other collinearly, so the resulting lattice can be scanned in the horizontal plane without losing beam overlap.

Experimental Realization of the Scanner

Figure 3.20 shows the optical setup of the top arm of the lattice. The laser is coupled out of the fibre with a fibre coupler. A $\lambda/2$-waveplate ensures the right polarization direction. The beam passes a $5:1$ telescope to reduce the beam waist down to $w = 500\,\mu\mathrm{m}$. It then passes the AOM used for positional stabilization, followed by the cascade of $4f$-telescopes and mirror galvanometers. A PBS before the first mirror galvanometer is

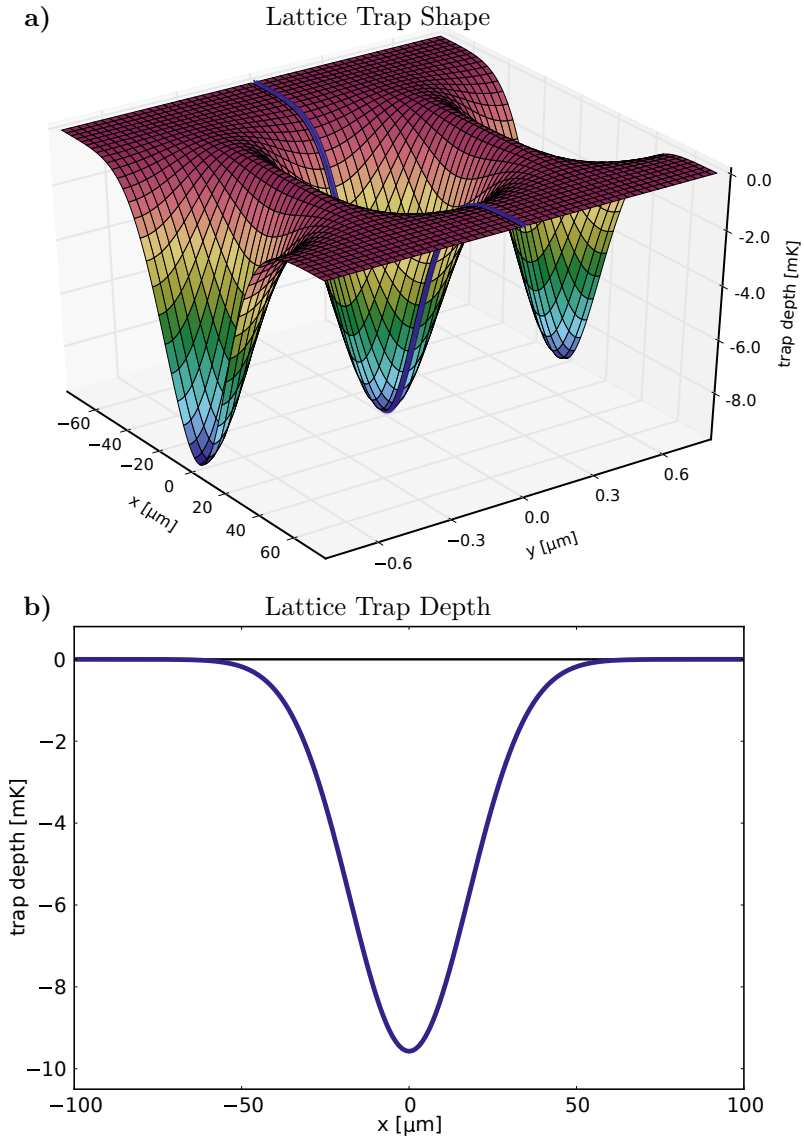

Figure 3.18.: Lattice trap shape. **a)** Potential landscape in the vertical plane. **b)** Cross section of the horizontal x-z-plane.

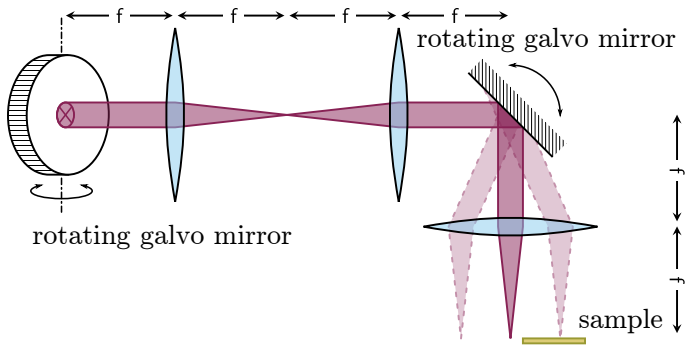

Figure 3.19.: The working principle of the scanner. Two-dimensional beam steering is achieved with a pair of galvo mirrors. The beams are always perpendicular to the sample surface.

used as a port for imaging. The image is scanned together with the top beam.

A set of three mirrors, not shown in Figure 3.20, folds the beam down into the main chamber, while maintaining the possibility to walk the beam path to match the bottom beam.

The bottom arm of the scanning lattice is shown in Figure 3.21. It effectively mirrors the top beam setup without the AOM. Another difference is the flipped second mirror galvanometer to match the scanning direction and a different orientation of the PBS. The cube is facing up and is used to inject the probe beam, as discussed in Section 3.5.

Lattice Stabilization

When moving the lattice over a reflecting sample, the bottom beam is blocked by the sample. It is replaced by the reflection of the top beam off the sample, now forming a standing wave. Figure 3.22 shows this process. At this point, the lattice is rigid, as the top beam and its reflection have the same frequency.

To keep the trap sites of the lattice intact, there should always be a

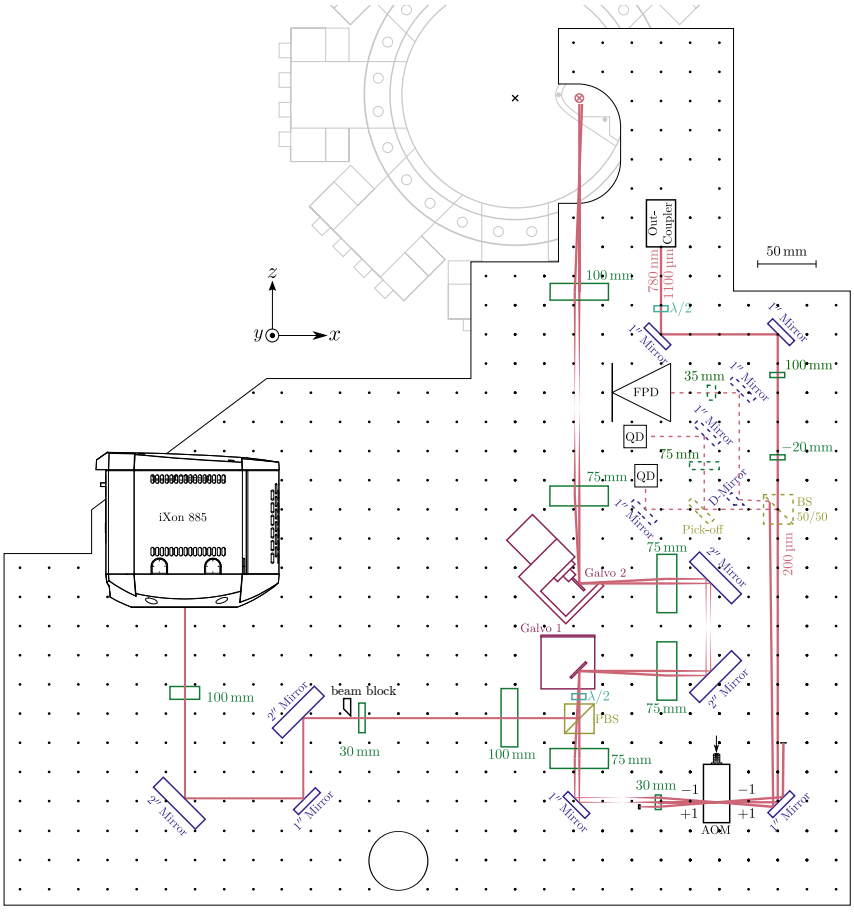

Figure 3.20.: Top layer of the scanner setup. Two galvo mirrors steer the top lattice beam. The same beam path is used for imaging as well.

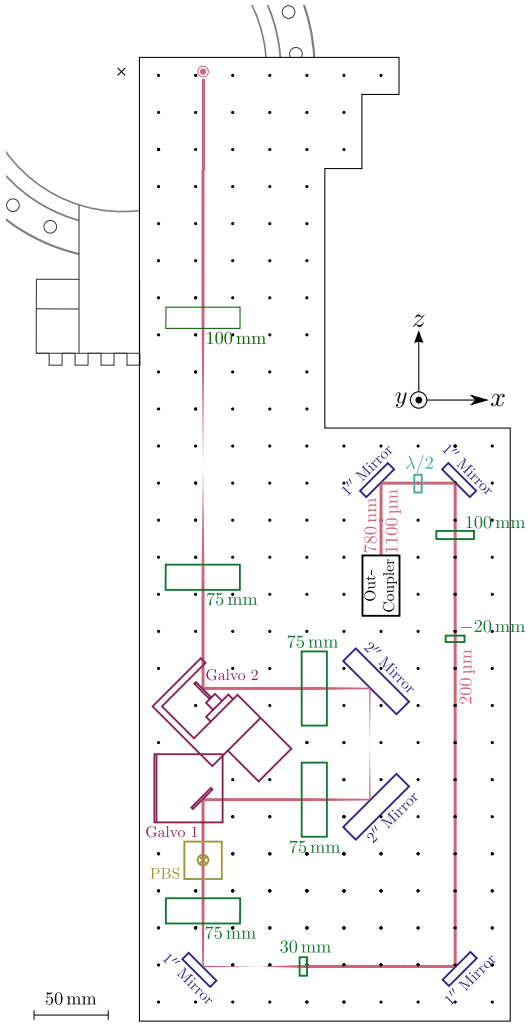

Figure 3.21.: Bottom layer of the scanner setup. Two galvo mirrors steer the bottom beam. A probe beam is injected into the same beam path with a PBS.

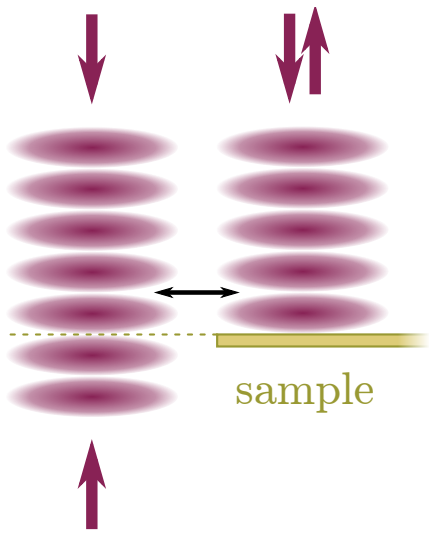

Figure 3.22.: There should always be a node at the sample height to keep the lattice intact when moving onto the sample.

node at the height of the surface during the transfer. The position of the lattice relative to the sample surface must therefore be known with sub-wavelength accuracy.

The following is a concept of an active feedback scheme to control the height of the elevator. It is not implemented yet, but it can integrate seamlessly with the existing setup. Figure 3.23 shows the schematics. The feedback is engaged when the lattice is very close to a sample with a reflective surface. Both laser beams have the frequency ω. An AOM at frequency Ω splits off a weak "pilot beam" off the top beam. It reflects off the sample surface and passes back straight through the AOM. By now the beam experienced a frequency shift of Ω from the first deflection.

The bottom beam, passing the sample, also gets deflected in the AOM, picking up a frequency shift of $-\Omega$. The reflected top beam and the bottom beam overlap and create a beat note on a fast photodiode. The difference frequency is 2Ω. This signal is mixed with the frequency-doubled

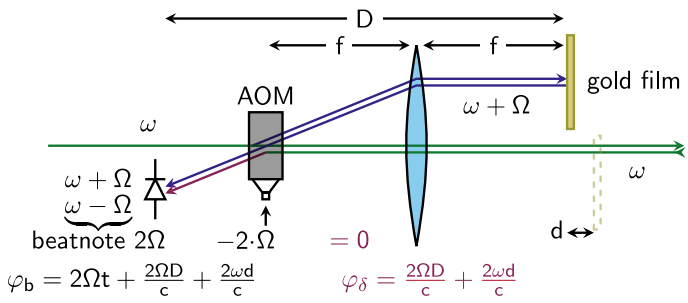

Figure 3.23.: The lattice beams, depicted in green, get refracted in an AOM. The resulting beam is indicated in violet. It then interferes with light reflected off the sample, as shown in dark blue. A photodiode detects the beat pattern from which a locking signal can be derived.

AOM driving signal, resulting in zero beat frequency. Remaining is, however, a non-zero DC offset depending on the phase difference φ_δ between the top and bottom beam.

This phase difference φ_δ has two contributions, the phase difference acquired due to the AOM $\frac{2D\cdot\Omega}{c_0}$ and the actual phase difference at the sample position $\frac{2d\cdot\omega}{c_0}$. It results to

$$\varphi_\delta = \frac{2D\cdot\Omega}{c_0} + \frac{2d\cdot\omega}{c_0}.$$

Here D is the optical distance between the sample and the photodiode, d is the distance between two nodes in top and bottom beam and c_0 is the speed of light. After careful calibration, the DC offset can be used to determine the node positions of the lattice with respect to the sample surface. The feedback then ensures that there is always a node at the height of the sample surface. This preserves the lattice sites during transfer.

3.5. Probing Section

Probing is possible in two locations of the setup: at the MOT position in the centre of the chamber and at the sample site, through the scanner optics.

The probe beam for the centre of the chamber is injected with a PBS into one of the vertical MOT beams. Since the MOT beams are circularly polarized with a $\lambda/4$-waveplate, so is the probe beam. Another $\lambda/4$-waveplate on top of the chamber changes the polarization of the probe beam to linear again. It is now again orthogonally polarized with respect to the MOT beam. Another PBS is used to separate the probe beam and send it to a camera.

The simple optical setup for probing at the sample site is depicted in Figure 3.24. A fibre coupler couples the light out of the optical fibre. A subsequent shutter blocks the beam by default and only opens for probing, as scattering of the on-resonant light would heat the rubidium atoms even when the controlling AOM is off.

A $\lambda/2$-waveplate and a PBS are used for power control. A mirror folds the beam down through a 200 mm lens to match the beam divergence of the bottom beam. The probe beam is overlapped with the bottom beam on a PBS, as shown in Figure 3.21 and described above.

The lattice beams are intense compared to the probe beam. They are still visible on the camera, even after the double-pass AOMs are switched off. To prevent this, the probe beam is aligned to have a small angle with respect to the lattice beams on the sample surface. This does not significantly affect the imaging, but it translates to a displacement between the beams in the Fourier plane of the imaging path. A razor blade as a beam block then skims off the lattice beam, as depicted in Figure 3.25. This protects the camera from the very intense and focused lattice light and makes imaging on this axis possible. Note that Figure 3.25 is simplified, as the beam block only removes the remnant of the lattice beams *after* being reflected towards the camera as depicted in Figure 3.20. Therefore the beam block does not obstruct the actual lattice.

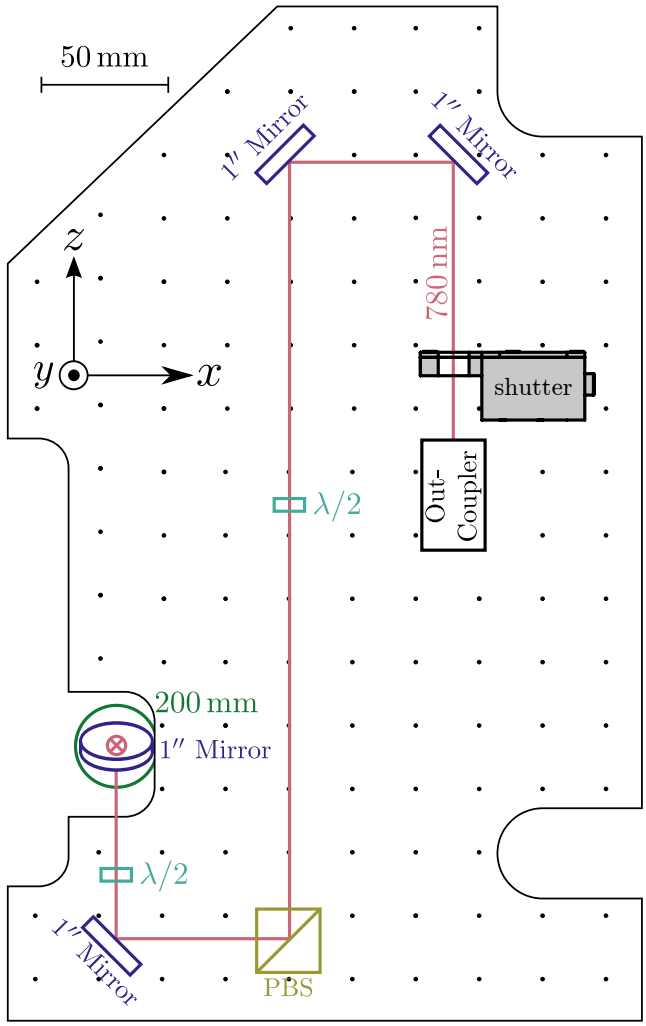

Figure 3.24.: Middle layer of the scanner setup. An imaging beam is injected downwards into the beam path of lower layer, depicted in Figure 3.21.

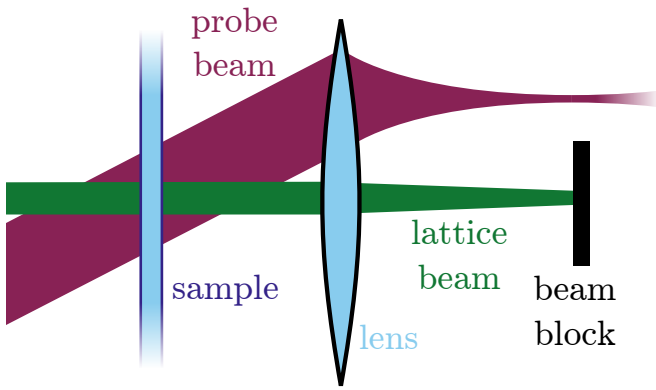

Figure 3.25.: Simplification of the imaging optics. The probe beam, shown in violet, has an angle with respect to the lattice beams, here depicted in green. Therefore both are separated in the Fourier plane and the lattice beams can be blocked to protect the camera.

4. Characterization

This chapter describes the loading and the performance of the traps used. Figure 3.1 on page 16 gives an overview of the different stages the atoms encounter. First the atoms evaporate from a solid piece of rubidium. The atomic vapour is then gathered in a two-dimensional magneto-optical trap. The so-called 2D-MOT then loads a following three-dimensional MOT, named 3D-MOT. Here the atoms are collected and cooled. The behaviour of both MOTs are studied in Section 4.1. From the 3D-MOT the atoms are loaded into an optical dipole trap for transport and cooling. The imaging of atoms in this trap is discussed in Section 4.2, while the loading is characterized is Section 4.3.

The last trap stage is an optical lattice. From here the atoms are transported downwards onto the sample surface. The imaging and the loading of the atoms into the lattice are discussed in Sections 4.4 and 4.5, respectively. The temperature of atoms in the lattice is examined in Section 4.6. In Section 4.7 the behaviour of the atoms in a moving lattice is analysed. Finally, conclusions are drawn in Section 4.8.

4.1. MOT Performance

The sole purpose of the 2D-MOT is loading the 3D-MOT. The crucial measure for the 2D-MOT is therefore the loading flux, measured in [atoms/s]. This is determined by how fast the 3D-MOT is filled with atoms. It is thus necessary to measure the atom number in the 3D-MOT to determine the performance of both the 2D-MOT and the 3D-MOT.

4.1.1. MOT Atom Number

Scattered 3D-MOT light is used to determine the atom number N_{Rb}. The light is detected using a silicon (Si) photodiode. This section explores the relation between the measured photodiode output voltage and the atom number.

The number depends on the scattering rate of the atoms Γ_{sc}, the photon detection rate Γ_{ph} and the fraction of photons $\frac{\Omega}{4\pi}$ that actually fall onto the detector. Here Ω is the solid angle around the MOT that is used for detection. With the assumption that no light gets lost at optical elements, the atom number is

$$N_{\mathrm{Rb}} = \frac{4\pi}{\Omega}\,\frac{\Gamma_{\mathrm{ph}}}{\Gamma_{\mathrm{sc}}}. \tag{4.1}$$

Note that this is an underestimation of the number of atoms, as in an optically dense sample, atoms in the centre of the MOT are shielded from the incident light. A lens collects the scattered light and focuses it on a Si photo diode. Mounted $d_0 = 200\,\mathrm{mm}$ away from the MOT, the lens has an aperture of $d_{\mathrm{lens}} = 22.9\,\mathrm{mm}$. As $d_0 \gg d_{\mathrm{lens}}$, the photodiode detects light from the solid angle

$$\Omega = \pi\,\frac{(\frac{d_{\mathrm{lens}}}{2})^2}{d_0^2} \approx 0.01.$$

For light with a photon wavelength of $\lambda = 780\,\mathrm{nm}$ the Si photodiode has a responsivity of $0.478\,\mathrm{A/W}$. A resistor and a gain stage give an output of $2.38 \times 10^5\,\mathrm{V/A}$ [Tho15]. The energy of a single photon is $E_{\mathrm{ph}} = hc_0/\lambda$. Here h is the Planck constant, c_0 the speed of light in vacuum and $\lambda = 780\,\mathrm{nm}$ the wavelength of the light. With the photodiode output voltage U_{pd} the photon detection rate results to

$$\begin{aligned} R_{\mathrm{ph}} &= \frac{U_{\mathrm{pd}}}{2.38 \times 10^5\,\mathrm{V/A} \cdot 0.478\,\mathrm{A/W}} \cdot \frac{780\,\mathrm{nm}}{hc_0} \\ &= U_{\mathrm{pd}} \cdot 3.452 \times 10^{13}\,\mathrm{s^{-1}\,V^{-1}}. \end{aligned}$$

The steady state photon scattering rate of a specific transition can be approximated as [MvdS12]

$$R_{\mathrm{sc}} = \left(\frac{\Gamma}{2}\right) \frac{(I/I_{\mathrm{sat},0})}{1 + 4\,(\Delta/\Gamma)^2 + (I/I_{\mathrm{sat},0})}.$$

Here $\Gamma = 2\pi \cdot 6.07\,\mathrm{MHz}$ is the natural decay rate of the excited state, Δ is the detuning of the MOT light from resonance, I_{sat} is the saturation intensity of the transition and I denotes the intensity of the six MOT beams combined. The cooling transition is the $F = 2 \rightarrow F' = 3$ transition with a saturation intensity of $I_{\mathrm{sat},0} = 1.669\,\mathrm{mW\,cm^{-2}}$ using $\sigma^{\pm}$-polarized light [ME88, TVH$^+$06].

The saturation intensity $I_{\mathrm{sat},\sigma^+}$ is used for the strongest transition $F = 2, m_{\mathrm{F}} = 2 \rightarrow F' = 3, m_{\mathrm{F}} = 3$ for σ^+-polarized light. It has a relative transition strength of 60. However, in a MOT the atoms are not in a single magnetic sub-state and the photons that they absorb can have any direction and polarization. For atoms in a MOT, the saturation intensity thus has to be modified. The relative transition strengths of the $F = 2 \rightarrow F' = 3$ transition for π-polarized light are 20, 32, 36, 32 and 20, respectively, with an average of $\frac{20+32+36+32+20}{5} = 28$. The correction factor is the average transition strength of $\alpha = \frac{60}{28}$. Therefore a larger power of $I_{\mathrm{sat}} = I_{\mathrm{sat},\sigma^+} \cdot \alpha = 3.576\,\mathrm{mW\,cm^{-2}}$ is necessary to saturate the atoms [MvdS12].

With an intensity of $I_{\mathrm{ind}} = 11.5\,\mathrm{mW}/3.45\,\mathrm{cm^2} = 3.32\,\mathrm{mW\,cm^{-2}}$ per one of the six individual MOT beams, and a detuning of $\Delta = 18.8\,\mathrm{MHz}$, the scattering rate results to

$$\begin{aligned} R_{\mathrm{sc}} &= \frac{2\pi \cdot 6.07\,\mathrm{MHz}}{2} \cdot \frac{6 \cdot \frac{3.32\,\mathrm{mW\,cm^{-2}}}{3.576\,\mathrm{mW\,cm^{-2}}}}{1 + 4\left(\frac{2\pi \cdot 18.8\,\mathrm{MHz}}{2\pi \cdot 6.07\,\mathrm{MHz}}\right)^2 + 6 \cdot \frac{3.32\,\mathrm{mW\,cm^{-2}}}{3.576\,\mathrm{mW\,cm^{-2}}}} \\ &= 2.364 \times 10^6\,\mathrm{s^{-1}}. \end{aligned}$$

Inserting these numbers into Equation 4.1 gives a relation of the atom number depending on the photodiode voltage. It results to

$$\begin{aligned} N_{\mathrm{Rb}} &= U_{\mathrm{pd}} \cdot \frac{4\pi}{0.0103} \cdot \frac{3.452 \times 10^{13}\,\mathrm{s^{-1}}}{2.364 \times 10^6\,\mathrm{s^{-1}}}\mathrm{V^{-1}} \\ &= U_{\mathrm{pd}} \cdot 1.782 \times 10^{10}\,\mathrm{V^{-1}}. \end{aligned} \tag{4.2}$$

4.1.2. MOT Loading Curve

Figure 4.1 shows a typical loading curve. With the relation of Equation 4.2 the approximate 3D-MOT atom number can be deduced from the voltage of the photodiode used to capture scattered light from the MOT.

The 2D-MOT provides a rate of about 4×10^9 atoms/s that can be captured by the 3D-MOT. After a loading time of 4 s, the number of atoms in the 3D-MOT is approximately 8×10^9 atoms. This is an underestimation, since we do not account for the optical density of the atom cloud. It should thus be understood as orders of magnitude. A longer loading time provides more atoms, but turns out not to improve the loading into the dipole trap, which is the next step.

4.2. Dipole Imaging

The dipole trap is far detuned to not heat the atoms. A side effect of this is that the atoms do not fluoresce and thus have to be imaged using a different technique: absorption imaging. A top hat beam with an intensity of $I = 13.4\,\mu\mathrm{W\,cm^{-2}}$ illuminates the atoms in the dipole trap. A lens with focal length of $f = 50\,\mathrm{mm}$ is placed $d_0 = 188\,\mathrm{mm}$ away from the trap and images the atom cloud onto a camera.* This imaging system has a magnification M of

$$M = \frac{f}{f - d_0} = -0.36.$$

For each atom number measurement, three images are taken. Two images are taken with probe light: one image with the atoms, one reference image without the atoms. A background image without probe light is taken to subtract stray light and other effects in the camera signal. The optical column density ρ_o along the imaging axis is calculated from the images using

$$\rho_\mathrm{o} = -\ln\left(\frac{I_\mathrm{atoms} - I_\mathrm{background}}{I_\mathrm{reference} - I_\mathrm{background}}\right).$$

* Prosilica EC650

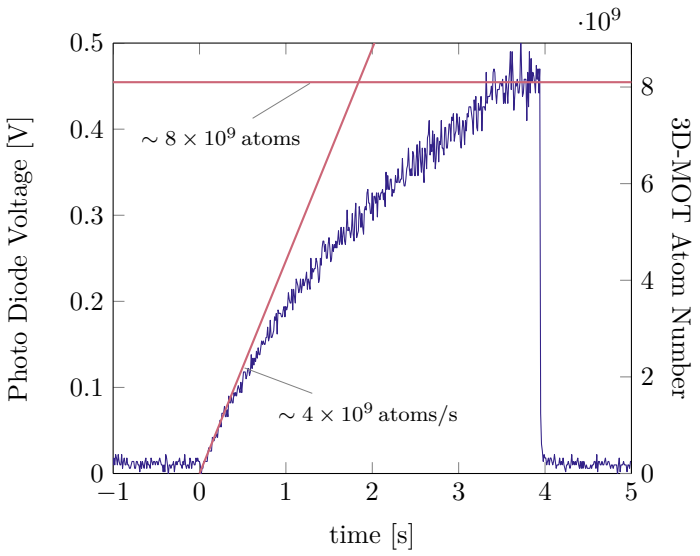

Figure 4.1.: Loading curve of the 3D-MOT. The 2D-MOT emits about 4×10^9 atoms/s that can be recaptured. Within 4 s a total of approximately 8×10^9 atoms are loaded into the 3D-MOT.

From the optical column density, the number of atoms N_{ODT} in the image can be calculated using [Gre13]

$$N_{\mathrm{ODT}} = \frac{M A_{\mathrm{pixel}}}{\sigma} \sum_n \rho_{\mathrm{o}}(x_n, y_n). \tag{4.3}$$

Here, n is the number of the pixel and $\rho_{\mathrm{o}}(x_n, y_n)$ its respective optical column density. The pixel area is $A_{\mathrm{pixel}} = 55\,\mu\mathrm{m}^2$. The absorption cross section σ is compensated for saturation effects, according to

$$\sigma = \frac{\sigma_0}{1 + \frac{I}{I_{\mathrm{sat}}}}.$$

The saturation intensity $I_{\mathrm{sat}} = \frac{I_{\mathrm{sat},0}}{\alpha}$ depends on the dimensionless transition strength α, which in turn depends on the occupation of the possible m_{F}-states of the atom ensemble. While exposed to the probe light,

the m_F-states change. It is, however, possible to numerically calculate a time-averaged overall transition strength, as depicted in Figure 4.2. The average transition strength is calculated as $\alpha = 0.524$ for an exposure time of 50 ms and an intensity of $I = 13.4\,\mu\mathrm{W\,cm^{-2}}$.

Furthermore, $\sigma_0 = 2.907 \times 10^{-9}\,\mathrm{cm^2}$ is the absorption cross section and $I_{\mathrm{sat},0} = 1.669\,\mathrm{mW\,cm^{-2}}$ is the saturation intensity, both for ^{87}Rb on the $F = 2 \rightarrow F' = 3$ cycling transition for $\sigma^{\pm}$-polarized light [MvdS12, TVH$^+$06, ME88].

Finally, the number of atoms in the image results to

$$N_{\mathrm{ODT}} = \frac{MA_{\mathrm{pixel}}}{\sigma_0}\left(1 + \frac{\alpha I}{I_{\mathrm{sat},0}}\right)\sum_n \rho_{\mathrm{o}}(x_n, y_n). \tag{4.4}$$

Figure 4.3 shows typical images of the transmittance and the optical density of atoms in the dipole trap. The image of the optical density also includes a mask, enclosing the area that contains atoms. The outside is used to subtract a possible non-zero background due to shot-to-shot fluctuations of the probe light.

4.3. Dipole Trap Loading

During the loading of the 3D-MOT, the capture efficiency depends on the scattering rate. A high scattering rate is preferable, since the thermal atoms coming from the 2D-MOT need to scatter many photons to lose their kinetic energy. Yet a high scattering rate limits dropping the temperature and increasing the density of a MOT.

The reabsorption of scattered photons leads to a repulsive radiation pressure. At high scattering rates there are collisions between ground- and excited-state atoms that can transfer excitation energy into kinetic energy and thus cause heating [GKC92].

The optimization of loading an optical dipole trap from a MOT has been discussed extensively [KCM$^+$00, CRGW03]. Different methods are combined to achieve a high transfer efficiency.

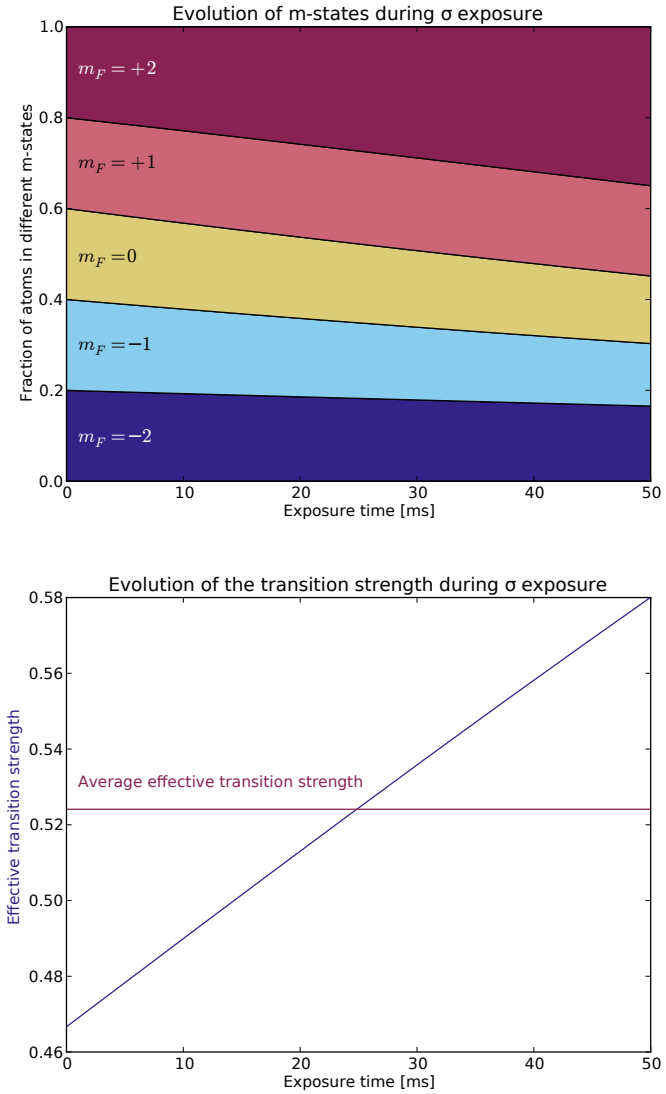

Figure 4.2.: Evolution of the m_F-states and the transition strengths during 50 ms of σ^+-light exposure with an intensity of $I = 13.4\,\mu W\,cm^{-2}$. This describes the dipole trap imaging in the centre of the chamber.

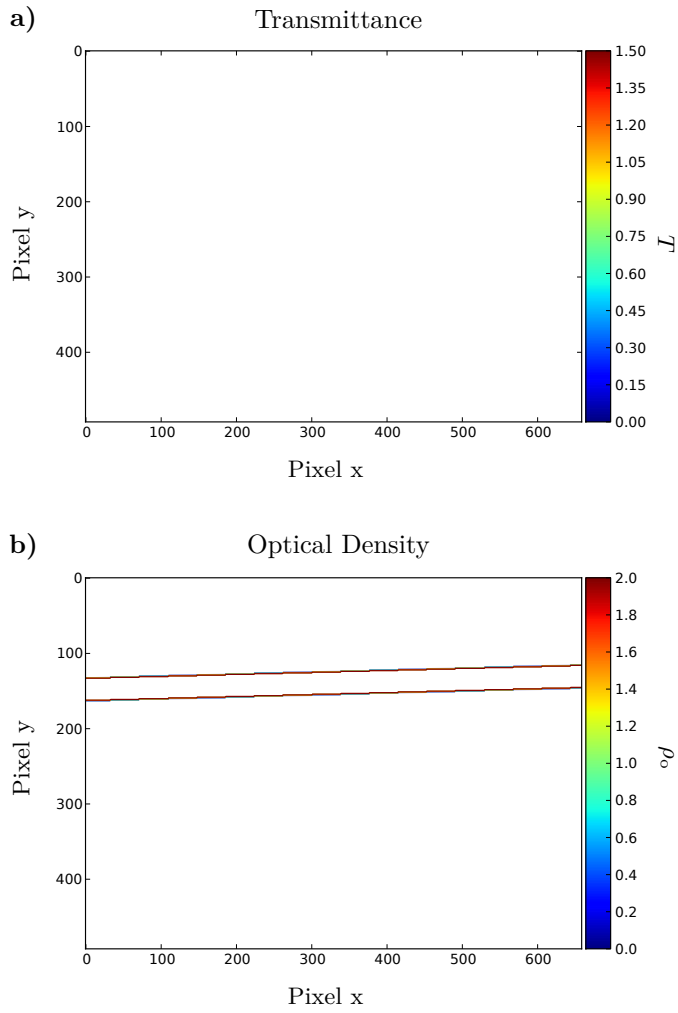

Figure 4.3.: Images of about 1.3 million atoms in the dipole trap. **a)** Image of the transmittance. The yellow background shows probe light with $T = 1$ and the atoms as a blue stripe with reduced transmittance. **b)** The same data expressed as optical density ρ_0. The atoms show as increased ρ_0 in yellow. The orientation of the atom cloud is determined (dashed white line) and a mask is placed around it for background normalization.

Shortly before the transfer the detuning of the cooling light is increased. At the same time, the repump light intensity is reduced to keep the atoms mostly in the "dark" hyperfine level ($F = 1$), a technique first explored by Pritchard et al. [KDJ+93]. Finally, the repump light is switched off shortly before the cooling light to transfer *all* the atoms into the $F = 1$ state. This prevents trap losses due to spin-exchange collisions in the loaded dipole trap.

These approaches, however, greatly reduce the scattering rate and thus the ability to capture thermal atoms from the 2D-MOT. It is therefore important to apply them only after a large number of atoms have already been loaded into the 3D-MOT.

To increase the loading efficiency further, the MOT is compressed during loading by ramping up the magnetic field. This will increase the atom density as well as the fractional trap volume overlap.

To test which of these techniques improve the loading efficiency, an experiment is conducted. All the permutations of

- Increase of Cooling Light Detuning
- Repump Intensity Reduction
- Repump Pre-Off
- Magnetic Compression

are explored at holding times of $t_{\mathrm{hold}} = 150\,\mathrm{ms}$ to $1000\,\mathrm{ms}$ to ensure the atoms in the dipole trap are fully thermalized. Five measurements per parameter combination are taken to reduce shot-to-shot fluctuations.

Figure 4.4 summarizes the results. The increase of the detuning of the cooling light frequency and the reduction of the repump light intensity greatly enhance the loading efficiency. Switching off the repump light before the cooling light causes a small increase of loaded atoms, whereas the magnetic compression has an adverse effect. With the right set of loading parameters, more than 2.2×10^6 atoms can be loaded into the dipole trap.

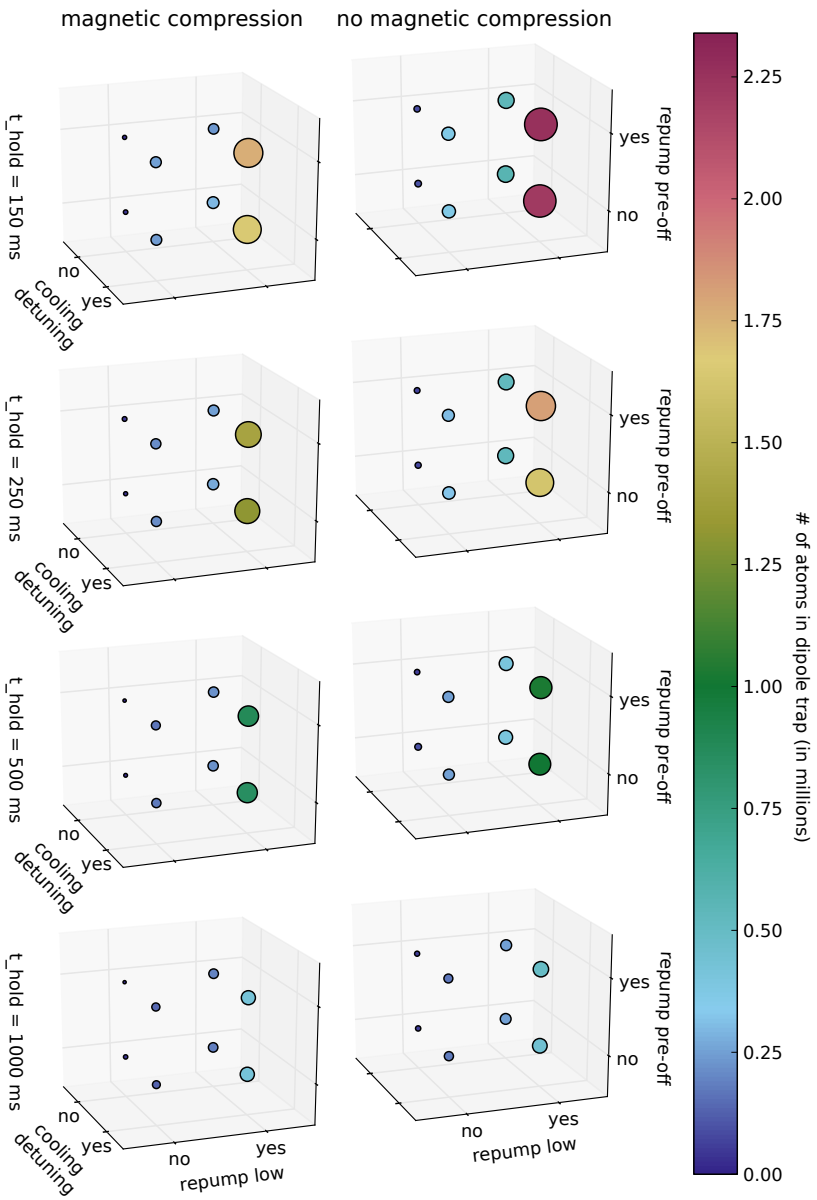

Figure 4.4.: Atom number measurement for different permutation of dipole trap loading parameters.

4.4. Lattice Imaging

Imaging on atoms in the lattice happens analogously to the dipole imaging described in Section 4.2. Just as in Equation 4.4, the number of atoms in the lattice is given by

$$N_{\text{lattice}} = \frac{M A_{\text{pixel}}}{\sigma_0} \left(1 + \frac{\alpha I}{I_{\text{sat},0}}\right) \sum_n \rho_{\text{o}}(x_n, y_n). \tag{4.5}$$

In this setup, the magnification is $M = 4.4$ and the pixel area equals to $A = 64\,\mu\text{m}^2$. Figure 4.5 shows that the average transition strength is calculated to be $\alpha = 4.33$ for an exposure time of 50 ms and an intensity of $I = 1.20\,\text{mW}\,\text{cm}^{-2}$.

4.5. Lattice Loading

After the rotation stage moved the dipole beam towards the sample site, the loading into the lattice starts. Two different techniques can be used to load the atoms: *Double Loading* and *Cascade Loading*.

Double Loading

Both lattice beams are ramped up synchronously. They are linearly ramped up in a time of $t_{\text{load}} = 50\,\text{ms}$ before the dipole beam switches off. The atoms are loaded from the dipole trap directly into the lattice.

Cascade Loading

The top beam is ramped up first. It follows the same procedure as above, being ramped up in $t_{\text{load}} = 50\,\text{ms}$ before the dipole beam is switched off. The bottom beam, however, is ramped up in the last 400 µs of the loading process. Without a lattice, the atoms accumulate inside the overlap volume. When the bottom beam is switched on, they distribute themselves along the lattice sites.

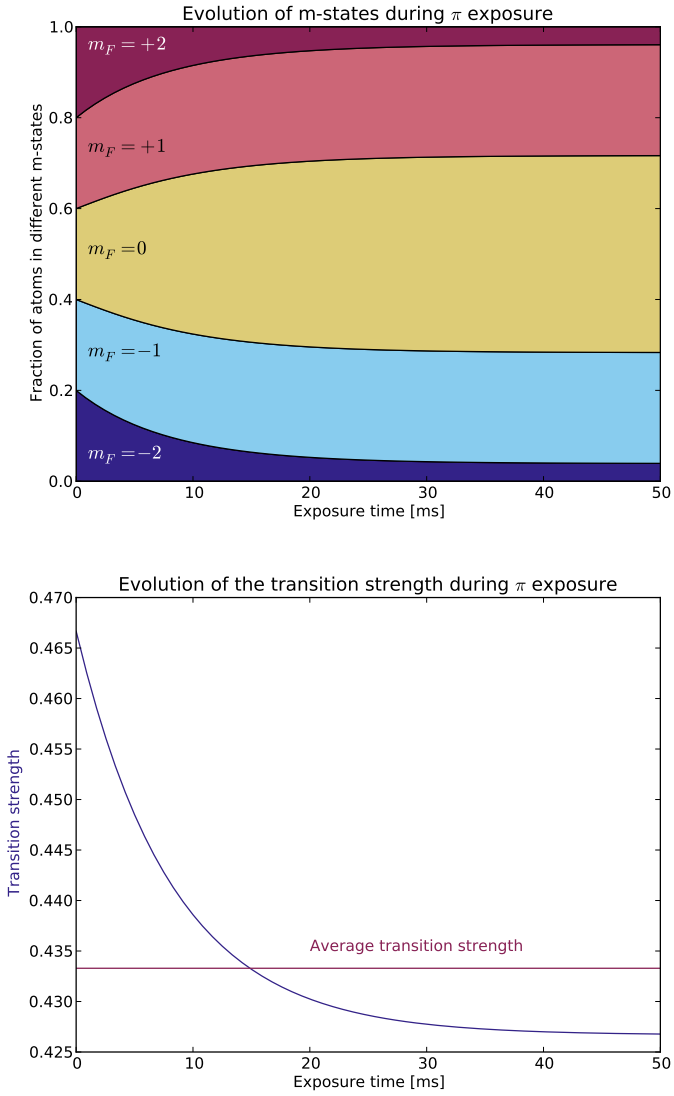

Figure 4.5.: Evolution of the m_F-states and the transition strengths during 50 ms of π-light exposure with an intensity of $I = 1.20\,\mathrm{mW\,cm^{-2}}$. This describes the lattice imaging at the sample site.

In general, using cascade loading will result in a higher atom number in the lattice. The atoms are, however, not as well confined in the lattice. They can spread along the axial direction of the top beam and therefore will occupy more sites in the final lattice, as described in the following sections. The choice of loading type depends on the experiment. For a higher overall atom number, cascade loading is preferable. For a more compact packet of atoms in the lattice, double loading should be employed. Unless otherwise noted, double loading is used for the experiments in this thesis.

Figure 4.6 shows a typical transmission measurement of atoms in the lattice above a sample. The sample in this case consists of arrays of pairs of Si_3N_4 membranes on a silicon substrate. Imaging light is therefore only visible above the membranes and blocked by the substrate everywhere else. Note that the atoms and the sample surface are not in focus at the same time. While the atoms are in focus, the edges of the membrane show fringes.

Table 4.1 shows the atom number of the different traps as well as the transfer efficiencies between them. The transfer between MOT and dipole trap is rather inefficient, because of a big MOT and small overlap volume between the two traps.

With a beam waist of $w_0 = 23.5\,\mu\text{m}$, a wavelength for the lattice beams of $\lambda = 780.6\,\text{nm}$, see Tables 3.1 and 3.2, respectively, and an atom number of $N = 300\,000$, as seen in Table 4.1, the average lattice occupancy can be estimated to

$$\bar{N}_{\text{site}} = \frac{N}{2\,w_0/\lambda} \approx 5000.$$

4.5.1. Dipole-Lattice Overlap

The loading efficiency of the lattice also depends on the overlap of the dipole beam and the lattice beams. Figure 4.7 shows the results of an experiment that explores this parameter. The transfer efficiency does not scale linearly with the overlap volume. A perfect overlap of the traps causes less atoms to be loaded into the lattice than with a slight mismatch. There are two hypotheses for this dip: Critical Density or Waterfall.

trap	3D-MOT	dipole trap	optical lattice
atom number	8×10^9	1.5×10^6	3×10^5
transfer eff.	2×10^{-4}		0.2

Table 4.1.: Transfer efficiencies between the traps.

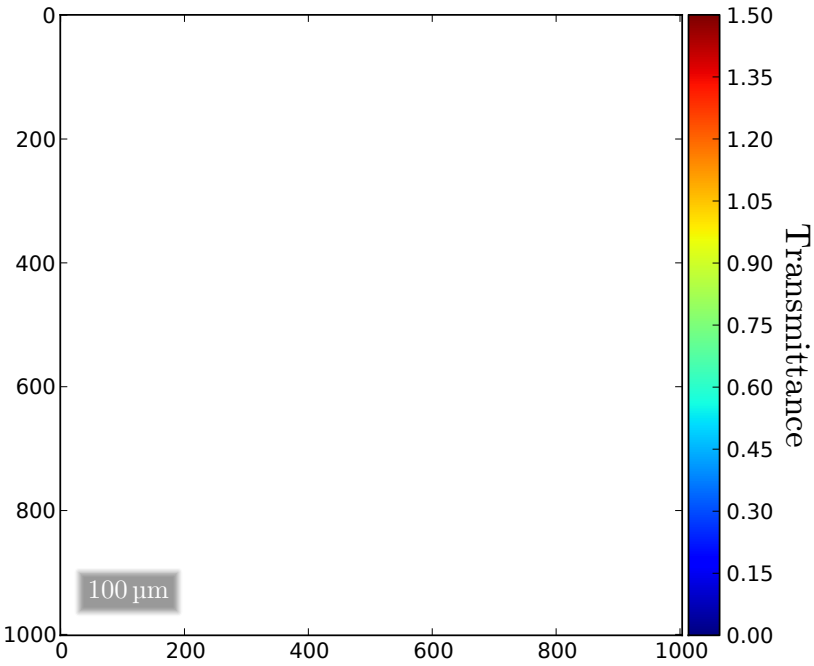

Figure 4.6.: Transmittance measurement of about 300 000 atoms in the lattice above two 1 mm × 100 µm Si_3N_4 membranes. The atoms appear as a blue dot ($T \approx 0$) above the left membrane (yellow, $T = 1$). Imaging happens in the axial lattice direction.

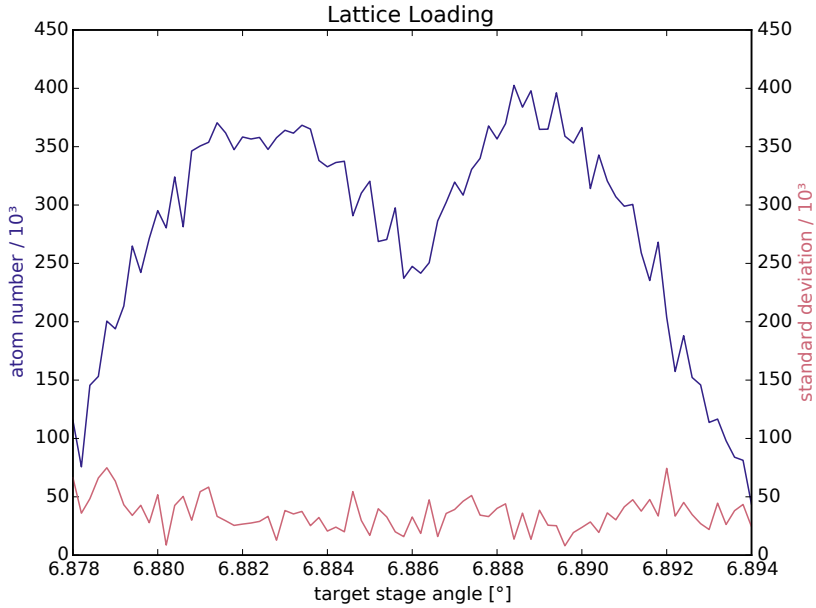

Figure 4.7.: Number of atoms, shown in blue, transferred from the dipole trap to the lattice. The best transfer is achieved with a slight mismatch in overlap between the dipole beam and the lattice beams.
The pink standard deviation does not scale with the atom number, indicating that the biggest contribution of noise might originate from other sources, for example from the imaging system.

Critical Density

With good overlap of the dipole trap and the lattice beams, many atoms are forced into the overlap volume. Their combined potential is deep, causing a high density of atoms in the overlap region. However a too high density causes increased three-body losses [SGOD+99].

Waterfall

During the cascade loading described in Section 4.5 an overlap mismatch could cause the atoms to fall out of the dipole trap and into the lattice beam. They are not confined in the horizontal plane anymore and thermally expand into the top lattice beam. The density in the overlap region would stay low as the atoms fill the lattice beam. The imaging direction is collinear with the lattice beams, so any expansion in the axial direction is not directly visible.

Atom transport measurements can be used to sample the cloud dimensions and gather evidence for either hypothesis. This will be discussed in Section 4.7.

4.6. Temperature in the Lattice

We can measure the radial temperature of the atom cloud by varying the time of flight. This is the time between releasing the atoms from the trap and taking the image of the atoms. Figure 4.8 shows an example of such a measurement. Fit parameters in this graph are the initial width $\sigma_0 = \sigma(t = 0)$ and the temperature T. The temperature can be derived by fitting the atom cloud width [GOSDD98]

$$\sigma(t) = \sqrt{\sigma_0^2 + \frac{k_\mathrm{B} T}{m_\mathrm{Rb}} t^2}.$$

Here k_B is the Boltzmann constant and m_Rb is the mass of a ^{87}Rb atom.

To verify whether the atoms are thermalized in the lattice, we measure the temperature as a function of lattice depth. It has been shown that

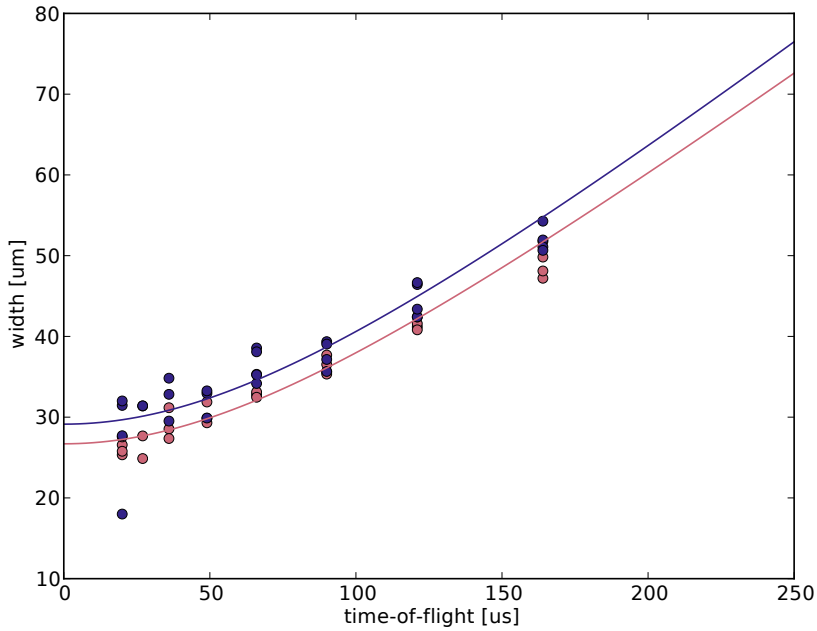

Figure 4.8.: Atom cloud size in x- and y-direction after time of flight, shown in blue and violet, respectively. The radial temperature of the atom cloud can be derived from the slope of the fit.

thermalized atoms have a temperature of about 13 % of the trap depth [MDS+88]. Figure 4.9 shows the temperature of the atoms normalized to the theoretical lattice depth as a function of the power in the lattice beams. As can be seen, the data show that this is more or less constant, indicating that the atoms are indeed thermalized. However, the temperature is about 9 % of the theoretical depth rather than 13 %, which we attribute to imperfections in the lattice due to, for example, a slight mismatch between the top and the bottom-beam of the lattice.

The lasers we use are not intensity stabilized yet. Intensity fluctuations can cause parametric heating [SOT97]. To exclude unnecessary heating,

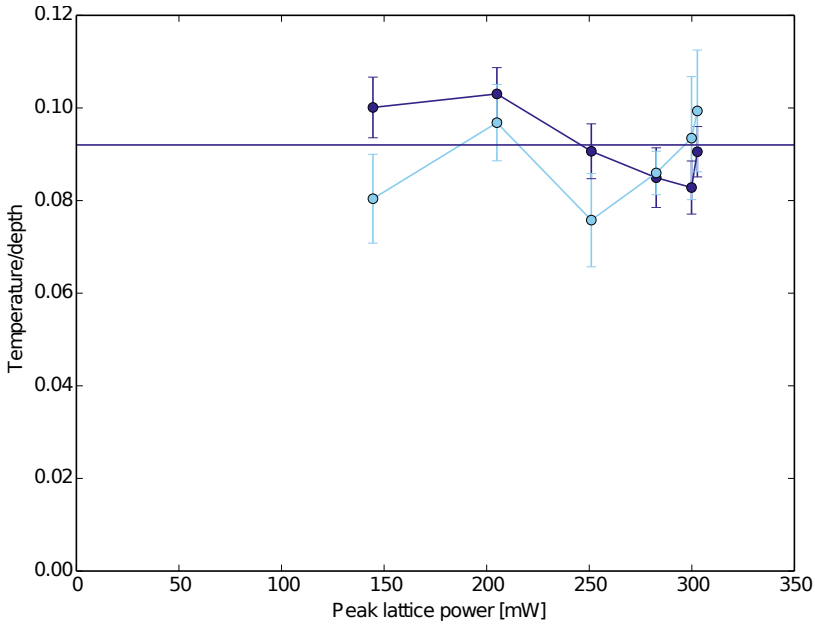

Figure 4.9.: The radial temperature of the atoms in x- and y-direction, shown in dark blue and light blue, respectively. The temperature of the atoms in the lattice scales linearly with the lattice depth, an indication for well thermalized atoms. The horizontal straight line indicates the average ratio of 9.2 %.

the noise spectrum of the lasers should be analysed. The intensity can then be stabilized, if necessary. This can be done with a photodiode and an AOM (Acousto-Optical Modulator). A part of the laser beam is split of and set to a photodiode. The photodiode provides a feedback signal for the AOM, with which the laser can be kept at a stable intensity.

4.6.1. Parametric Heating

Parametric heating is the process that occurs when periodically modulating a trap at a modulation frequency close to the trap frequency [SOT97]. At the right modulation frequencies the atoms resonantly gain energy; they are heated and can even escape from the trap. By measuring the atom losses as a function of the modulation frequency, we can thus deduce the effective trap frequencies to characterize the lattice further.

All parametric heating experiments presented in this section are done in a static lattice by modulating the trap depth periodically for 1 ms. After the trap modulation, the remaining atom number is measured. Figure 4.10 shows atom losses over a wide range of modulation frequencies. Losses occur in a narrow range in the kHz regime as well as in a broad range in the MHz regime. In both cases the resonances are very broad, since the trap is anharmonic.

The lattice experiences a modulation proportional to four times the driving frequency. The light in both arms of the lattice are modulated with opposing detunings. This corresponds to a factor of two. Furthermore, the light of each arm double-passes an AOM and picks up twice the AOM driving frequency, contributing another factor of two and resulting in a factor of four in total. So we hit a trap resonance ω_0 with a driving frequency of $\omega_{\text{drive}} = \frac{1}{4}\omega_0$. The trap potential is symmetric, so we expect parametric heating to occur not at the fundamental trap frequency, but at the higher harmonics starting from $\omega_{\text{harm}} = 2 \cdot \omega_0$. The first parametric heating should then occur starting at $\omega_{\text{drive}} = \frac{1}{4}\omega_{\text{harm}} = \frac{1}{2}\omega_0$ and even higher harmonics.

Low-frequency range Figure 4.11 shows a detailed study of the parametric heating in the low-frequency range, corresponding to excitations in the weak, radial trap direction. Plotted are the peak optical density, used as an indication of the atom number, and the atom cloud width as a function of the modulation frequency. The different subplots show parametric heating experiments for various lattice powers. Since the trap potential is symmetric, a parametric depth modulation should result in

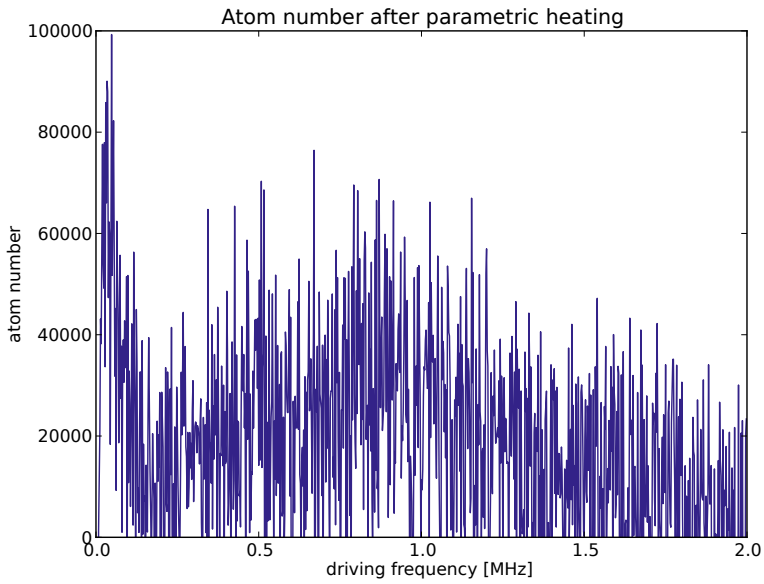

Figure 4.10.: Atom loss as a function of lattice modulation frequency. There are two separate regimes of losses, one for low frequencies (kHz) and one for high frequencies (MHz).

resonant heating at twice the trap frequency [Gri05]. There is a double dip structure in the atom losses at the first harmonic and the weaker third harmonic.

Apart from larger noise, the initial cloud width stays constant at the resonance frequencies. The atom cloud thus stays well thermalized and hot atoms get lost from the trap.

Furthermore, the frequency at which atom losses occur shifts with lattice power. This is expected, as the trap shape stays Gaussian and a shallower trap will have a lower resonance frequency. The resonance frequency shift is now analysed further.

The resonance frequency ω of a trap with a Gaussian shape is given by [GWO99]

$$\omega = \sqrt{\frac{-4U_{\max}}{mw_0^2}}.$$

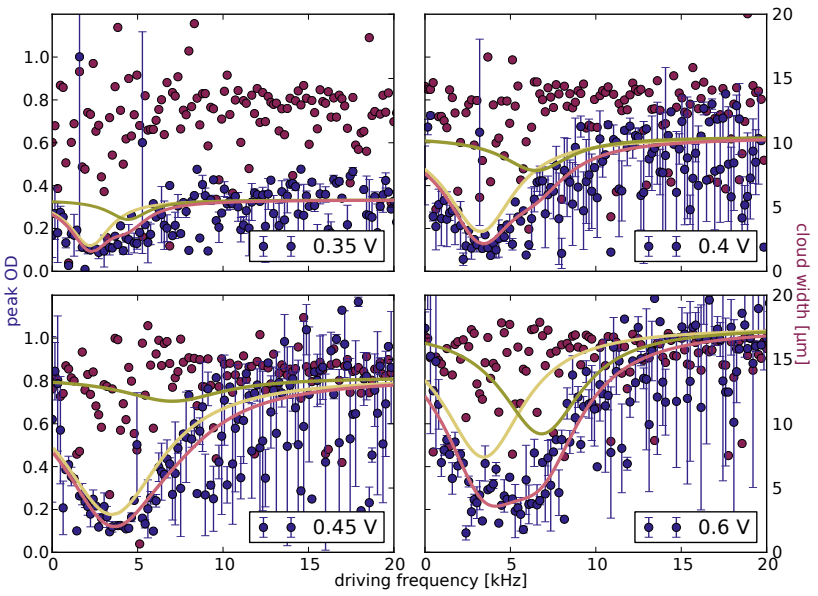

Figure 4.11.: Atom loss, plotted in blue, as a function of low lattice modulation frequencies. The position of the double dip scales with the trap depth, while the cloud width, indicated in pink, stays constant.

Here U is the trap potential, w_0 is the waist of the Gaussian beam and m is the mass of a ^{87}Rb atom.

The depth of an optical trap is [GWO99]

$$U_{\mathrm{dip,max}} = -\frac{3\pi c^2}{2\omega_0^3}\left(\frac{\Gamma(\omega_0/\omega)^2}{\omega_0-\omega}+\frac{\Gamma(\omega_0/\omega)^2}{\omega_0+\omega}\right) I_{\mathrm{max}}.$$

Here c is the speed of light, ω_0 is the resonance frequency of the atom, ω is the laser frequency, Γ is the natural line width of the atom and I_{max} the peak intensity of the laser beam. With the beam power $P_0 = \frac{1}{2} I_{\mathrm{max}} \pi w_0^2$ of a Gaussian beam with beam waist w_0, we can rewrite the resonance frequency to

$$\omega = C\sqrt{P_0}, \tag{4.6}$$

where

$$C = \sqrt{\frac{12\pi c^2 \left(\frac{\Gamma(\omega_0/\omega)^2}{\omega_0-\omega} + \frac{\Gamma(\omega_0/\omega)^2}{\omega_0+\omega}\right)}{\pi m w_0^4 \omega_0^3}}.$$

In Figure 4.12, the fundamental resonance frequency is plotted against the peak lattice power and Equation 4.6 is fitted to the data, using C as a fit parameter. The measured fundamental frequencies fit well within their standard deviations, but lie about 17 % below the predicted value from Table 3.2, where we used the theoretical value for C. The trap depth depends quadratically on the trap frequency, so this corresponds to a trap depth that is 31 % lower than theoretically expected. We again attribute this to beam imbalance or imperfect mode overlap.

We can now compare the results of the parametric heating experiment with the time-of-flight measurements. Both experiment give an indication of the trap depth, and for both it lies below the theoretical prediction. Figure 4.13 re-examines the time-of-flight measurement from Figure 4.9. Added to the plot is now the theoretical prediction of a lattice filling fraction of 12.9 % [MDS$^+$88] and the same value reduced by 31 % to account for the lattice deficiencies determined in the parametric heating experiment. The determined trap depths for both experiments are in excellent agreement with each other, they differ by less than 4 %! This is remarkable, since these are two very different sets of experiments. It gives confidence in our measurement approach.

High-frequency range A closer study of the losses in the high-frequency range is shown in Figure 4.14. Plotted are again the peak optical density and the atom cloud width as a function of the driving frequency. This frequency range corresponds to excitations in the tight trap direction, i.e. along the lattice.

Compared to the low-frequency experiment the peak optical density reduces less strongly. One remarkable feature of the high-frequency parametric heating experiment is that the initial atom cloud width actually changes significantly. This is because the atoms are excited *in the direction of the lattice* and start to populate higher bands. Due to the sinusoidal

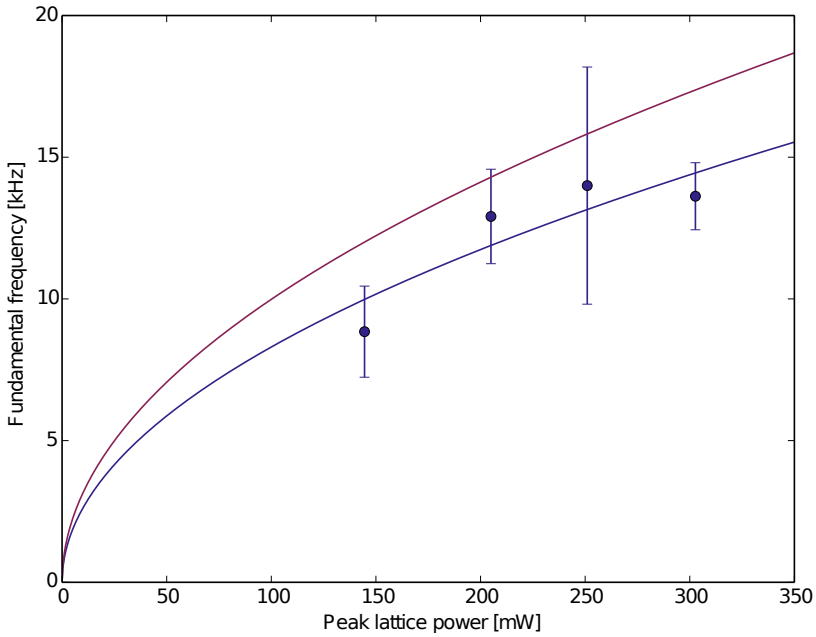

Figure 4.12.: In this parametric heating experiment, the trap frequency changes with lattice power. The blue solid line is a fit to the data. It is about 17 % below the violet theoretical prediction, indicating lattice imperfections.

trap potential, the atoms experience a shallower trap there. They are thus also more weakly confined in the radial direction, leading to an increase in the initial width of the atom cloud. The radial temperature of the lattice (not shown) shows no significant change.

This indicates that there is a lack of thermal equilibrium between the tight and the weak direction of the lattice. Consequently we have to be very careful when talking about the temperature of atoms in the lattice.

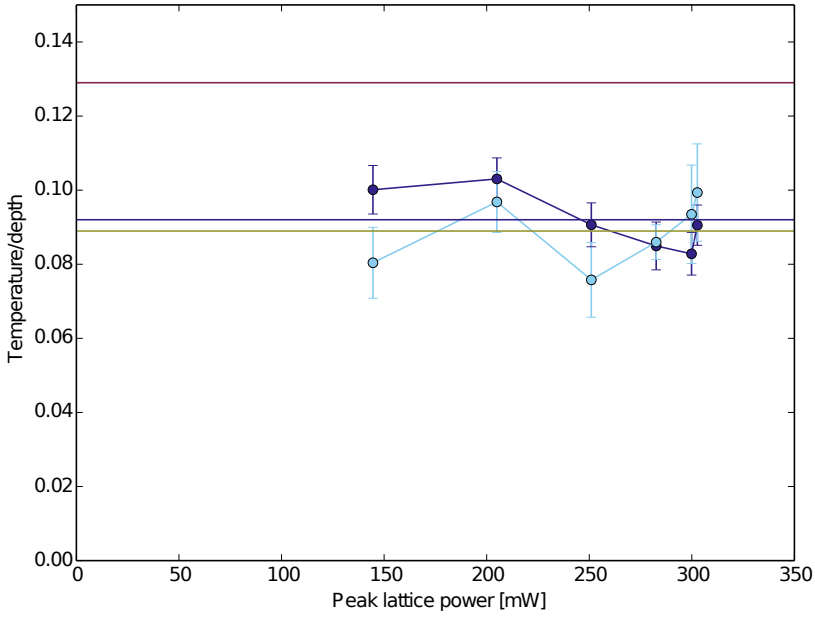

Figure 4.13.: The radial temperature of the atoms in x- and y-direction, shown in dark blue and light blue, respectively. The violet theoretical prediction of 12.9 % reduced by the lattice deficiency (shown in olive) agrees well with the measured average, indicated in dark blue.

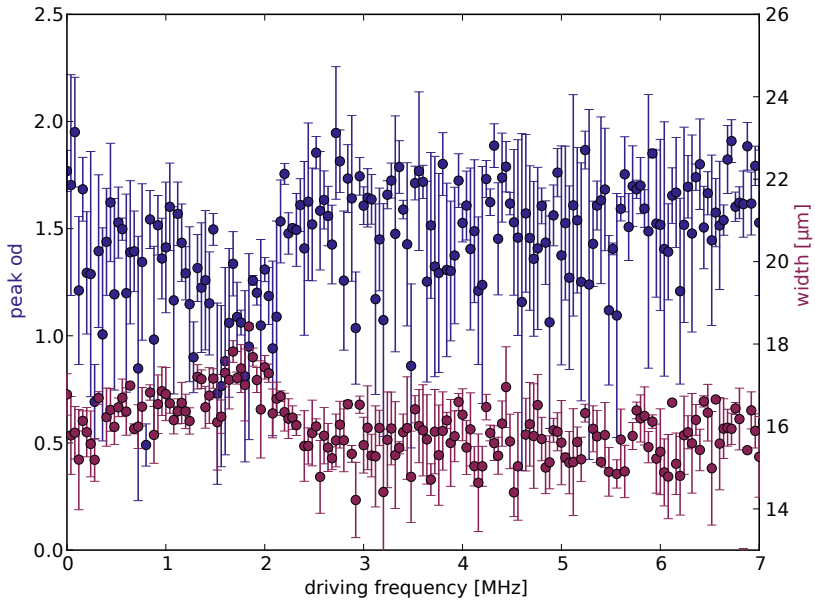

Figure 4.14.: Parametric heating of the atoms in the lattice for large frequencies. The remaining atom number varies greatly with the frequency.

4.7. Lattice in Motion

To transport the atoms down to the sample surface, the lattice has to move. As described in Section 3.4.2, this is done by imposing a frequency difference Δf between the two lattice lasers.

The lattice travels the distance λ per time $t = 1/\Delta f$. The lattice velocity is thus

$$v(t) = \Delta f(t) \cdot \lambda.$$

The velocity profile is usually a trapezoid, as illustrated in Figure 4.15. The assumption is that by accelerating slowly enough the atoms will follow the lattice adiabatically. The overall distance travelled is then

$$d = \int_0^{t_{\mathrm{hold}}} v(t)\,\mathrm{d}t.$$

Figure 4.16 shows the atom number measured as a function of this distance d. The atoms are moved towards a sample, an uncoated BK7 glass slide. The total holding time stays constant at 2 ms or 3 ms while the distance is controlled by changing v_{max}.

When the lattice moves down towards the sample, indicated by positive distances, the measured atom number decreases sharply: once the atoms crash into the sample surface, they bond to the substrate. This changes their electron configuration such that they are not on resonance with the probe light anymore. The slope of the curve is, however, broader than expected. According to Table 3.1, the atom cloud delivered by the dipole trap should have a vertical extent of about 50 µm. However, the width of the slope in crash curve measurements is a few millimetres. On their way down to the sample, the atoms apparently spread out inside the lattice.

4.7.1. Spreading of Atoms in the Conveyor

A series of experiments is conducted to narrow down possible causes of the atom spreading in the lattice. Different aspects of the loading processes and lattice motion are investigated.

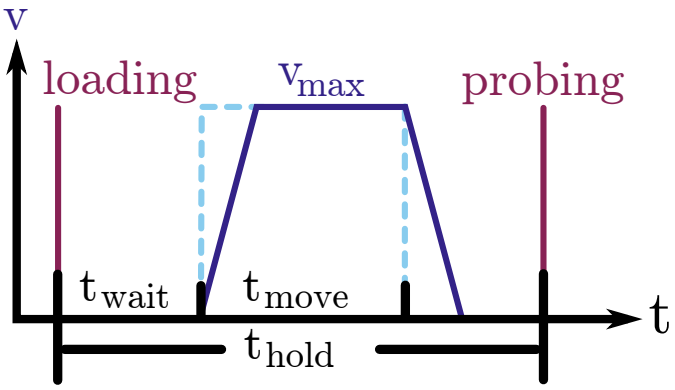

Figure 4.15.: The atoms are loaded into the lattice and held for a total time of t_{hold}. After a time of t_{wait} the atoms are moved with a trapezoidal velocity profile $v(t)$, shown in dark blue, for an effective move time of t_{move}.

Lattice Acceleration The first experiment tests whether the adiabaticity of the atoms following the lattice depends on the acceleration of the lattice, as a possible cause of the behaviour can be that the lattice accelerates too fast for the atoms to follow. Figure 4.17 shows the resulting crash curves for four different move times t_{move} that result in four different lattice accelerations.

In this experiment, the overall move time t_{move} is kept constant while the maximum lattice velocity is varied to yield the desired distance d. The same velocity trapezoids are applied for all move times. After rescaling the x-axis to "distance moved", all curves collapse onto the same trace, regardless of what parameter combination is used. Different accelerations therefore do not change the shape of the crash curve; it only matters how far the lattice actually moved. The hypothesis that the lattice moves too fast is thus falsified.

Lattice Loading A crash curve with a higher time resolution might give more insight in the mechanisms of the atoms spreading inside the lattice.

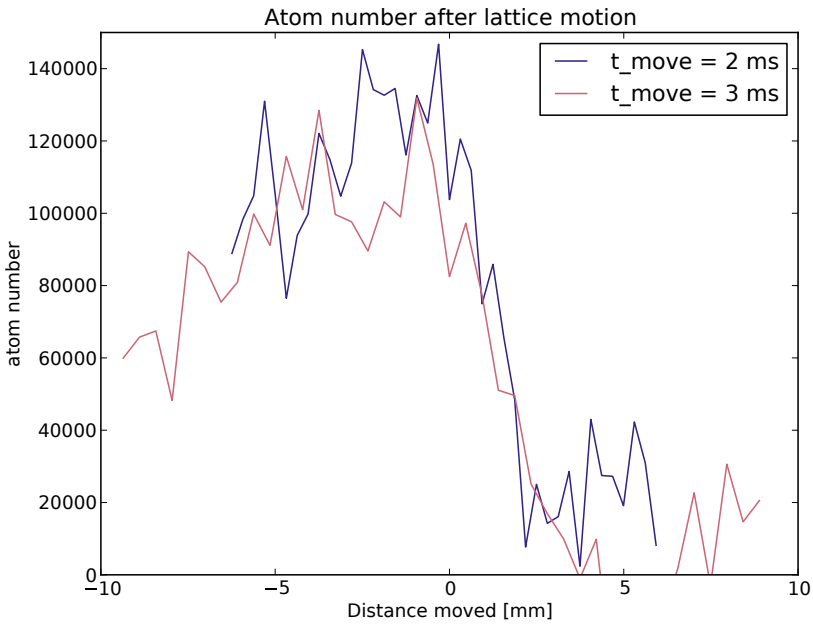

Figure 4.16.: Atom number measurement after lattice motion. The lattice beat frequency is varied, while the move time is kept constant. A positive distance means that the lattice is moving down towards the sample. The atom number sharply declines when the atoms hit the sample surface.

Figure 4.18 shows such a measurement. Within a fixed moving time of $t_{\mathrm{move}} = 10\,\mathrm{ms}$, the lattice is moved a variable distance. Again, this is done by changing the maximum difference frequency Δf applied to the lattice light and thus varying the maximum velocity of the lattice. At the same time we also test the influence of the two different loading techniques described in Section 4.5: cascade loading and double loading.

During cascade loading the atoms are first loaded into the overlap volume of the dipole trap and a single lattice beam within 50 ms. Then quickly within 400 µs the second lattice beam is ramped up. The lattice forms as both lattice beams interfere with each other and the atoms are

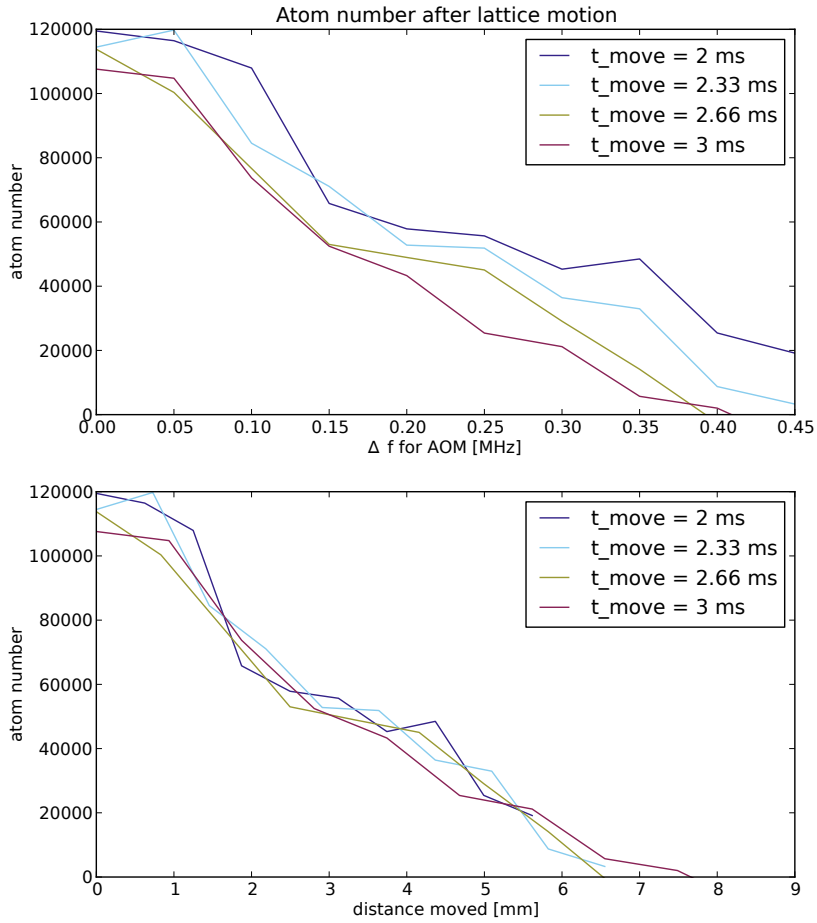

Figure 4.17.: Atom number after lattice motion using different moving times and accelerations. When scaled to total distance moved, the curves collapse onto each other. Using different accelerations does not influence the motion of the atoms contained in the lattice. It only matters how far the lattice actually moves.

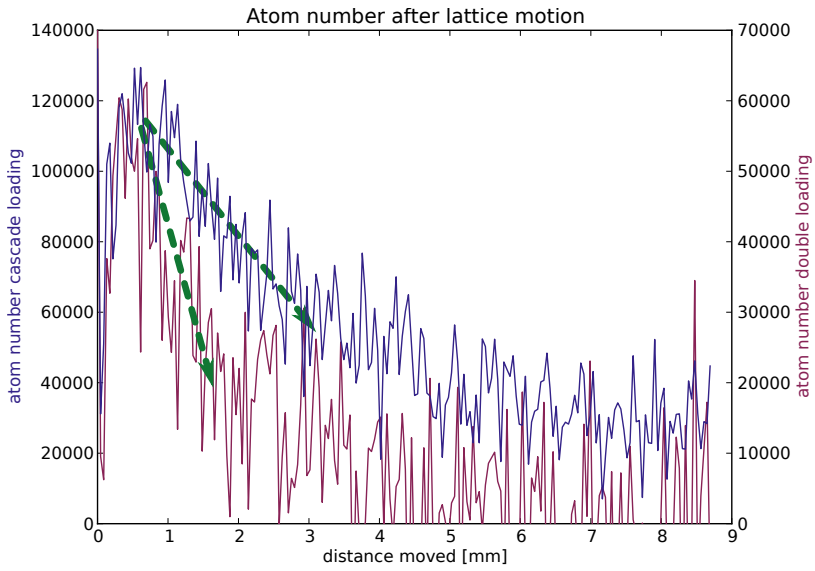

Figure 4.18.: Atom number as a function of distance moved. The overall moving time t_{move} stays constant, while the maximum of difference frequency between lattice beams Δf and thus the maximum velocity v are changed to reach different distances.
Observations are: Cascade loading loads more atoms. Cascade loading causes a gentler atom loss slope, as indicated by the green guide-to-the-eyes. There are high losses for short distances moved.

forced into the lattice sites. For double loading, both lattice beams are ramped up simultaneously in 50 ms. The three main observations from the lattice loading crash curves are:

1. Cascade loading loads more atoms than double loading. During the loading phase the single lattice beam has a larger overlap volume with the dipole trap than the lattice formed by both lattice beams. So more atoms are in the overlap volume of both lattice beams when the lattice is formed.

2. Cascade loading causes a gentler atom-loss slope than cascade loading. Using cascade loading atoms spread more inside the lattice, either during loading or during transport.

3. There are high losses for short distances moved for both loading types. At these short distances the atoms have not reached the sample surface yet, so there must be a different loss mechanism than adsorption on the sample surface.

Atom Recapturing In a related experiment we study the behaviour of the atoms when moving very small distances. In this experiment we avoid the lossy low-frequency regime discovered in the previously described experiment. After moving a few micrometres, the atoms are recaptured into the dipole trap. That way we measure how many atoms remain at the starting position; we are mapping the in-situ atom distribution of the lattice. Figure 4.19 shows the results for upward and downward motions.

A main lobe with radius of about 50 µm is distinguishable from a flatter background. The background remains high, indicating a spreading of the atom cloud in the lattice direction. The shapes of the curves for both loading techniques, however, are similar. This indicates that the spreading mechanisms for both loading techniques are the same. As expected, due to symmetry arguments the results for upward and downward motion are comparable; as long as the atoms do not reach the surface, moving up or down should give the same results.

With no distance moved, cascade loading still causes an overall higher atom number. The ratio between both loading techniques is about 20 %. This difference is much lower than at the previous experiment. For the lattice loading crash curve, shown in Figure 4.18, this difference is close to 50 %! While the two loading techniques cause a large difference in atom number in the whole lattice, they have a smaller impact on the atoms in the overlap region of the lattice and the dipole trap. This indicates that the atoms spread into the lattice already during double loading, which contradicts the above reasoning of identical spreading mechanisms.

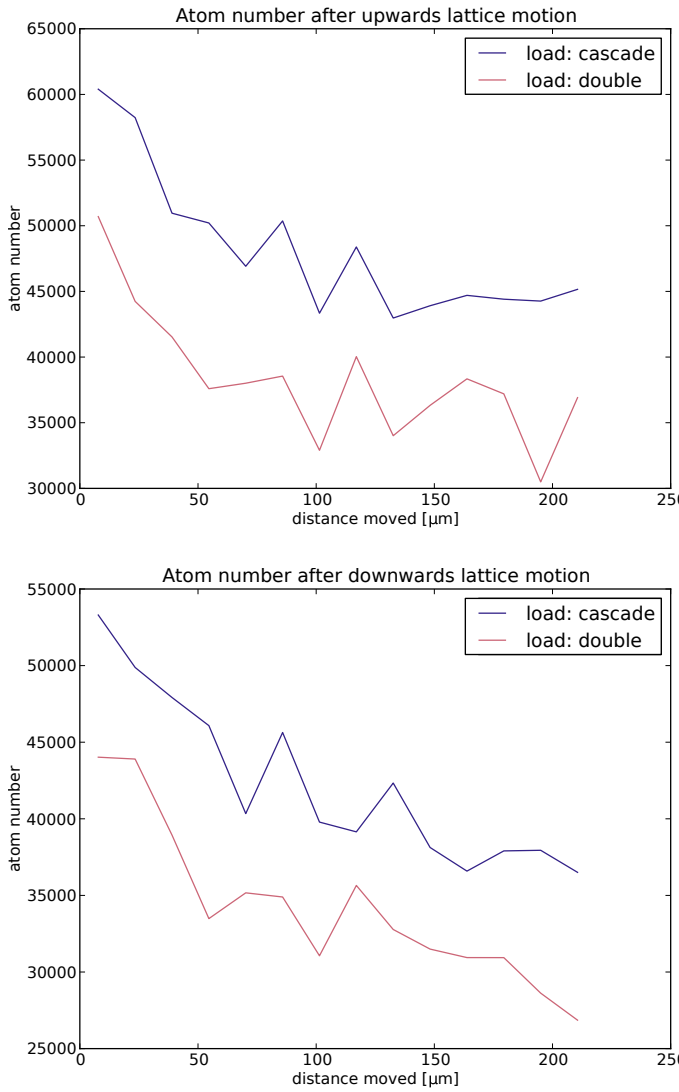

Figure 4.19.: Recapturing of the lattice atoms into the dipole trap after motion. This samples the cloud shape inside the lattice. The measurements of the upwards and downwards motion are symmetric.

Lifetime Measurements As another test for atom spread, a completely static lattice is used. In this experiment the atoms are held for a certain holding time and then recaptured in the dipole trap. This way we can sample the number of atoms that remain in the overlap volume. This is then compared with a holding time experiment without recapturing. Figure 4.20 shows the results.

There are obviously fewer recaptured atoms than atoms still in the lattice. But the atom number also decreases faster. Atoms thus tend to stay in the lattice, not in the overlap volume. They move within the lattice. Without any motion of the lattice, there is atom diffusion between the lattice sites.

Diffusion after Motion To test how much the atoms spread out after the motion of the lattice, we perform the following experiment. Within a holding time of $t_{\mathrm{hold}} = 10\,\mathrm{ms}$ the lattice is moved downwards. The motion lasts for $t_{\mathrm{move}} = 3\,\mathrm{ms}$ and is performed either at the beginning ($t_{\mathrm{wait}} = 0\,\mathrm{ms}$) or the end ($t_{\mathrm{wait}} = 7\,\mathrm{ms}$) of the 10 ms time frame. If the atoms do not spread after the lattice motion, the results for motion at the beginning or the end of the holding time should be the same.

The timing and the results of this experiments are shown Figure 4.21. The same experiment is conducted at different trap depths, indicated by different AOM voltages for the lattice beams. We see a significant difference in atom losses as a function of distance moved if the waiting time t_{wait} is varied. Therefore the atoms spread also after the lattice is moved.

For a follow-up experiment, the lattice is moved down for two millimetres within 3 ms. The velocity profile is kept constant, the only varying parameter is the starting time of the motion. Figure 4.22 shows the results: a longer waiting time before the motion t_{wait} causes less atom losses after the same lattice motion.

If we assume that less losses infer that there is less diffusion, then the amount of diffusion should scale with the time the atoms spend in the lattice *after* the lattice motion. The spreading of the atoms thus does

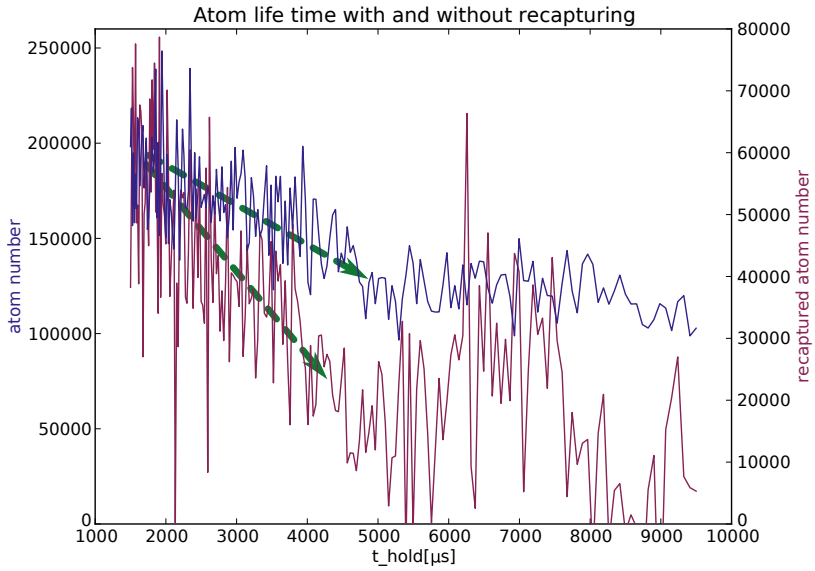

Figure 4.20.: Atom lifetime measurement with (violet) and without (dark blue) recapturing after holding. The atom number after recapturing decays faster, as implied by the green guide-to-the-eye. This indicates that the atoms spread through the lattice, even when the lattice is not moving.

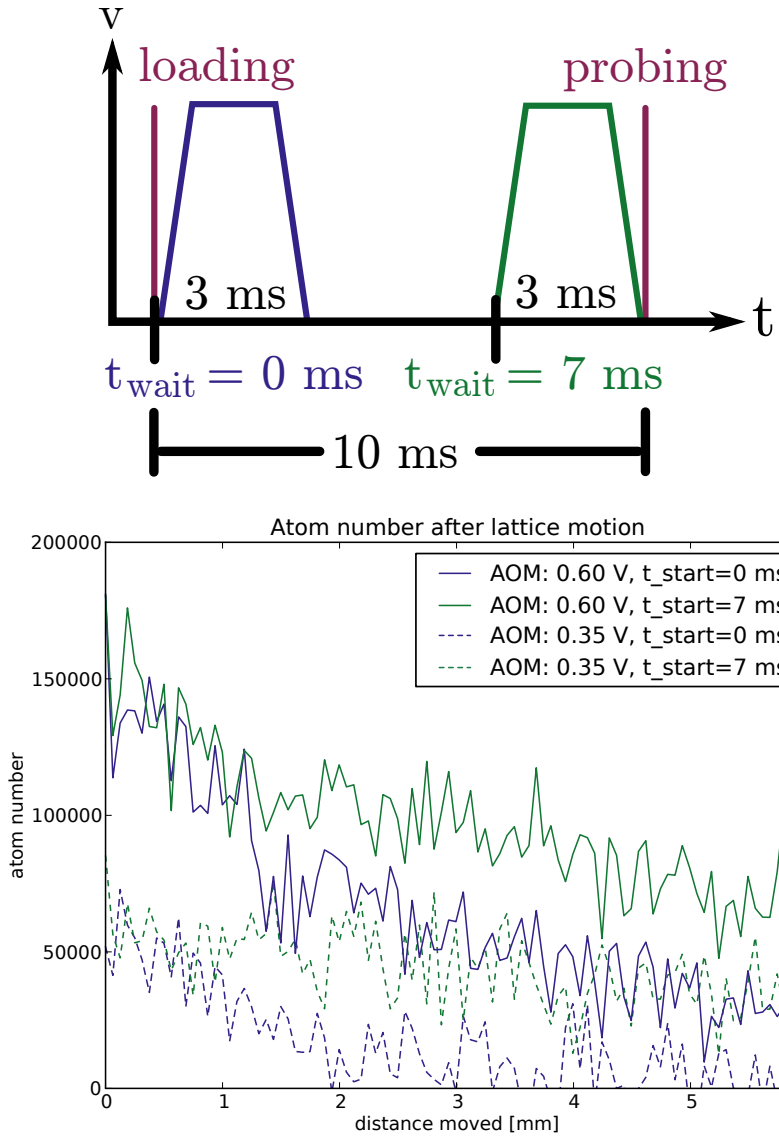

Figure 4.21.: Atom crash curve at two lattice depths with a total holding time of 10 ms. Less atoms disappear when the motion starts at the end of this time frame.

not only occur during motions. Rather, the motion increases the rate of spreading.

4.7.2. Summary

We can conclude that there is diffusion through the lattice even when the lattice is static. This diffusion most likely increases when the lattice is in motion and persists even when the lattice comes to a rest. Furthermore, there are substantial losses for specific difference frequencies Δf of the lattice beams.

4.8. Conclusion

We can successfully load atoms into a lattice. This lattice is movable in three dimensions, allowing for atom transport onto a sample surface.

There are still many questions with regards to the vertical transport of the atoms. The atoms diffuse inside the lattice. There are strong losses when the lattice is moved slowly. However, even without fine-grained control over the vertical motion, the setup can be used to transport atoms onto a sample surface.

Experiments alone are not sufficient to discover the cause of atom losses at low lattice speeds and atoms diffusing through the lattice. In Chapter 5 computational models are used to simulate the atom behaviour. This will also give more insight into variables that are so far unknown, such as the height of the atoms above the sample.

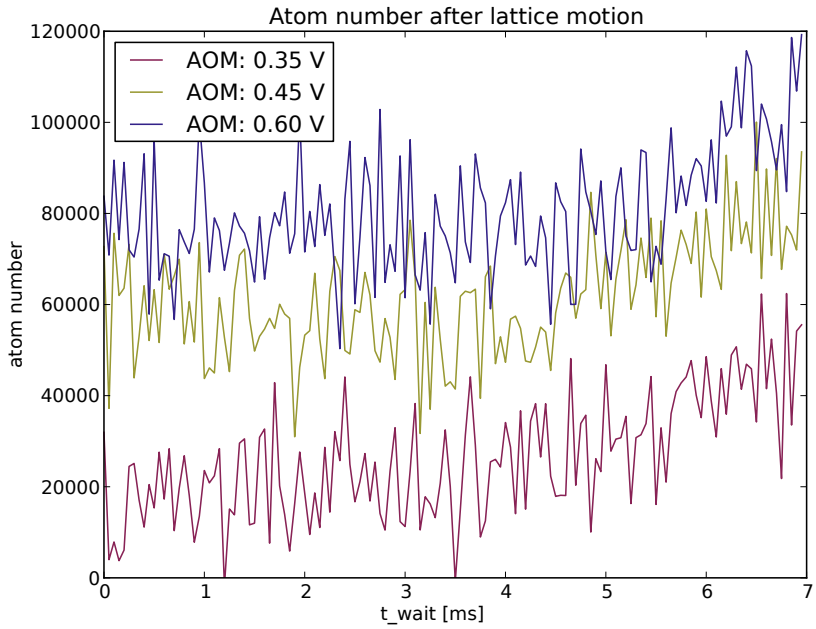

Figure 4.22.: Lattice motion of 2 mm towards the sample. The starting time is varied within a holding time frame of 10 ms. Despite a total move time of 3 ms, it takes the atoms 5 ms to all reach the sample.

5. Modelling

The previous chapter raised some questions about the vertical transport of the atoms. It is clear that the atoms spread inside the conveyor. Furthermore, there are regions of lattice velocities that cause strong atom losses.

To gain a better understanding of which mechanism is involved, numerical models are used to simulate the diffusion behaviour of the atoms through the conveyor.

5.1. Introduction

Before writing the first line of code, a few assumptions have to be made. Firstly, we have to formulate a hypothesis for the unexpected behaviour. Based on this hypothesis we can determine the physics to be modelled. Lastly, we have to decide which parameters can be fixed and which are variable.

5.1.1. Hypothesis

The experiments in the preceding chapter raised questions about the atom losses for low lattice velocities, i.e. low difference frequencies Δf between both lattice arms and about diffusion of the atoms between lattice sites. Both of these features were already encountered in the parametric heating experiments from Section 4.6.1. The experiments indicated losses for low frequencies as well as an increase in atom mobility in the lattice for higher frequencies. However, in the rest frame of the lattice, both lattice beams are Doppler shifted to have the same frequency. On these grounds, the

trapped atoms do not experience a difference frequency between the two lattice beams.

The coupling mechanism could be the presence of other weak, static lattices. The glass substrate of the sample is mostly transparent in the near-infrared regime, yet it reflects some light on each glass-vacuum interface. A quick estimation can be made using the Fresnel Equations. Using the refractive indices $n_1 = 1$ for vacuum and $n_2 \approx 1.5$ for BK7 glass at a wavelength of 780 nm [Sch15], the reflectance $R_\perp$ of a beam impinging perpendicularly on a glass-vacuum interface is thus [Hec15] $R_\perp = \left|\frac{n_1-n_2}{n_1+n_2}\right|^2 = 4\,\%$.

There are at least two static lattices, one from each glass-vacuum interface. When the lattice is set in motion, it moves across these weak static lattices, interfering with them and changing the overall lattice depth periodically with a frequency proportional to the difference frequency of the lattice beams. The weak, static lattices disturb the moving potential where the atoms are trapped in. This brings us to the hypothesis for the model:

Weak, static lattices induce parametric heating, causing losses and diffusion.

First we test with a microscopic model how much heating the static lattices can cause.

5.2. Microscopic Model

To investigate the effect of the above-mentioned static lattices, we first modelled the motion of 1000 independent atoms in a one-dimensional periodic potential by solving the classical equations of motion for these particles. The atoms each have a different initial velocity, ranging from 0 to $10 \cdot v_{\mathrm{th}}$, where v_{th} is the thermal velocity corresponding to the temperature we assume the atoms to have in the lattice.

The lattice is accelerated for 1 ms to a speed of 3.12 m/s, moves at constant speed for 2 ms and is decelerated again for another 1 ms, coming

to a rest. In this unperturbed case, all atoms remain in the lattice site they started in and thus end up at the target position.

This changes if a perturbation is added in the form of a weak static lattice. This static lattice interferes with the strong, moving lattice, disturbing its potential. Figure 5.1 shows histograms of the position of the atoms at several times during the motion of the lattice. We can distinguish three classes of atoms. About half of the atoms still stay within their starting lattice sites, as they did in the unperturbed case. Some atoms stay behind this main bulk and some are ejected in the forward direction.

We find that the initial velocity is not a good indicator of which class an atom ends up in. We also find that the velocity spread of atoms in the lattice is increasing by roughly a factor of two during the motion. The microscopic model shows therefore that a static lattice can cause considerable heating.

We can also calculate the shape of a crash curve, like the one shown in Figure 4.17. By discarding atoms that reach a distance of 3.5 mm we find the crash curve shown in Figure 5.1. The shape of this curve clearly does not match the experimental results. Something must therefore be missing in the model.

The model used here is a fully coherent system without coupling between the atoms. It thus cannot capture any interactions between the atoms, such as thermalisation. However, adding atom-atom interactions into the microscopic model is unfeasible. There are physical parameters that still need to be determined, so the model would need to be used as a fitness function in a fitting routine. This would be computationally too costly. This is why we have to make use of a macroscopic model.

5.3. Macroscopic Model

In the macroscopic model, the atoms are not treated individually. Rather, the model describes the lattice sites, an atom number n per lattice site and an energy c. The atoms are assumed to be instantly thermalised in

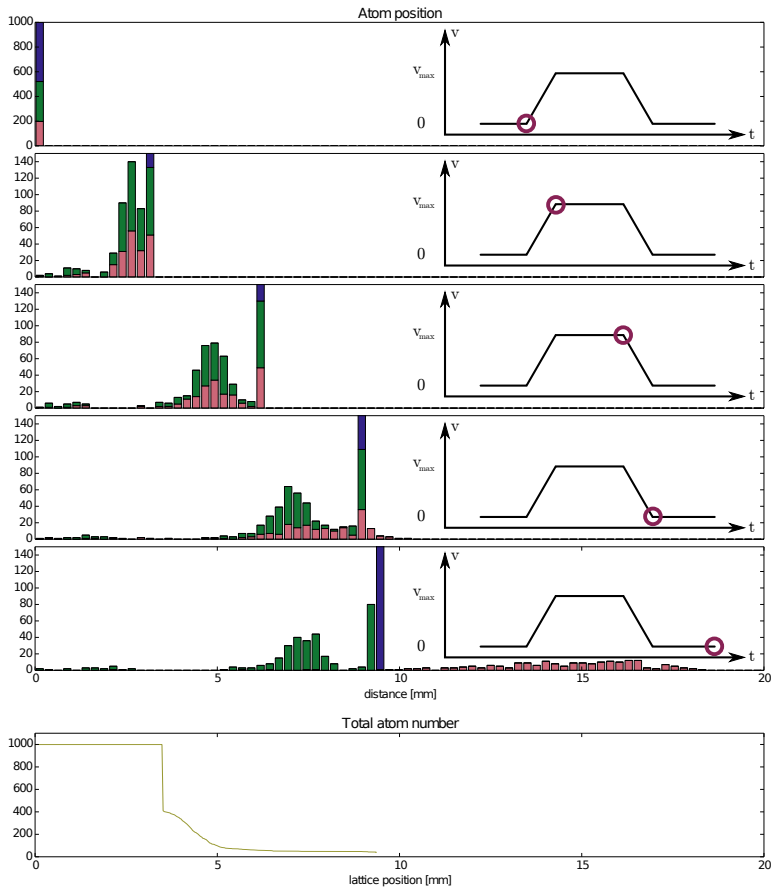

Figure 5.1.: Transport of 1000 atoms perturbed by a static lattice. Position histograms for different phases (violet) of the velocity profile. Half of the atoms always stay within their lattice position, shown in dark blue. After the starting position the y-axis is re-scaled to highlight the evolution of the mobile atoms. Some atoms start moving in the lattice during the acceleration (green), others during deceleration (pink). The atom number as a function of distance (plotted in olive) shows a sharp dip, followed by a small tail.

the lattice direction, since the energy c is associated with a lattice site, not with individual atoms.

5.3.1. Physics

The macroscopic model is based on a diffusion equation, including frequency-dependent losses and diffusion increase.

The time evolution of a certain number of atoms $n(x,t)$ of the lattice in the conveyor is given by

$$\frac{\partial n}{\partial t} = C\nabla^2 n. \tag{5.1}$$

For the general case, $C = C(x,t)$ is the diffusion matrix that describes the system.

The heating losses are assumed to happen predominantly through thermalisation or photoassociation. As these processes include two atoms, they depend on the local density n of atoms; specifically they scale as n^2. We can thus write the equation for the atom density as

$$\frac{\partial n}{\partial t} = -s_{\mathrm{L}}\ L(f)\ n^2, \tag{5.2}$$

where $L(f)$ is a frequency-dependent dimensionless loss function that can be derived from the parametric heating experiments. We use a fit of the data from the parametric heating experiment at low frequencies shown in Figure 4.14, invert it and normalize it to one. Figure 5.2 shows the resulting function. With $L(f)$ known from previous experiments, all that we still need is a scaling factor s_{L} that will be a fit parameter for our model.

The mobility of the atoms at lattice site i is determined by the average energy c_i of the atoms on that lattice site. The higher the energy, the higher bands they occupy. Higher band occupation leads to higher mobility.

It is important to keep in mind that this is *not* the temperature of the atoms because of the lack of thermalisation between the weak and the tight lattice direction, as discussed in Section 4.6.1. However, the

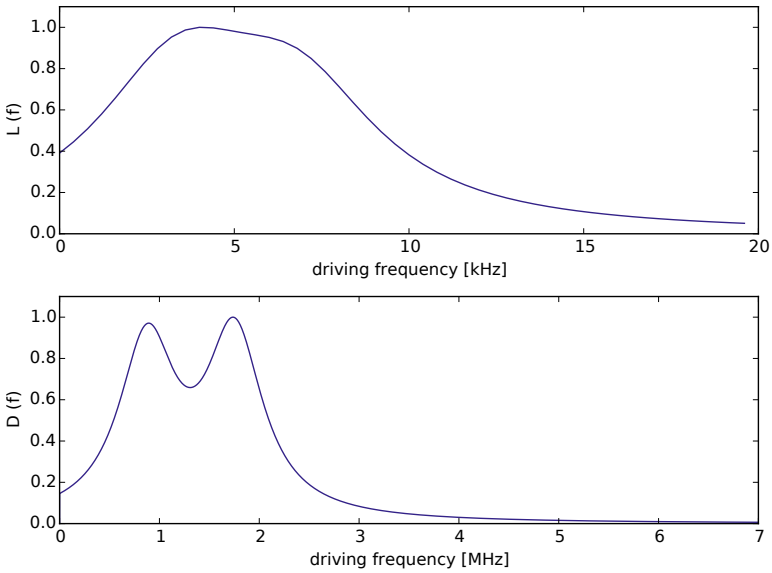

Figure 5.2.: The loss function $L(f)$ and the diffusion function $D(f)$ used in the model. Both are derived from fits to data from parametric heating experiments in Section 4.6.1.

formulaic description of the energy of the atoms in the lattice direction is that of a temperature and the involved variables have the unit Kelvin.

As in the case for losses, we can characterize the heating by a frequency-dependent dimensionless diffusion function $D(f)$, which is derived from the parametric heating experiment at high frequencies. The resulting function is also plotted in Figure 5.2. With a scaling factor s_{D}, we use the differential equation

$$\frac{\partial c_i}{\partial t} = s_{\mathrm{D}}\ D(f) \tag{5.3}$$

to describe the changes in energy. Both s_{D} and $D(f)$ are positive, so the energy of the atoms can only increase. Equation 5.3 also has an integration constant, corresponding to the initial diffusion D_0 in the system.

The Equations 5.1, 5.2 and 5.3 have to be discretized to be numerically treated. In Appendix 5.9 it is explained in detail how the equations change

to

$$\frac{\partial c_i}{\partial t} = s_\mathrm{D} D(f) \quad \Longrightarrow \quad B_{i,j+1} = B_{i,j} + s_\mathrm{D} D(f)\,\delta t \tag{5.4}$$

$$\frac{\partial n}{\partial t} = C\nabla^2 n \quad \Longrightarrow \quad \left[B^{-1}\right]_{ii'}\ n_{i',j+1} = n_{i,j} \tag{5.5}$$

$$\frac{\partial n}{\partial t} = -s_\mathrm{L} L(f)\, n^2 \quad \Longrightarrow \quad n_{i,j+1} = n_{i,j} - s_\mathrm{L} L(f)\, n_{i,j}^2\,\delta t. \tag{5.6}$$

The matrix B is closely related to the diffusion matrix and equates to

$$B = \frac{\delta t}{(\delta x)^2} \begin{pmatrix} 1-2c & c & 0 & \cdots \\ c & 1-2c & c & \cdots \\ 0 & c & 1-2c & \cdots \\ \vdots & \vdots & \vdots & \ddots \end{pmatrix}.$$

Some parameters of the model are known from experiments. The width of the atom cloud is measured to be $w_0 = 47\,\mu\mathrm{m}$. And as explained, the shapes of the resonances for the frequency-dependent losses and the diffusion are determined from previous experiments. These parameters are shared among all experiments.

Other parameters have to be determined on a per-experiment basis. The holding time of the atoms in the lattice t_hold and the induced frequency curve $f(t)$ are known, as they are set in the experimental scripts. Then there are the variable parameters. Firstly, the number of atoms before motion n_0 is not known for most experiments done in the past. Secondly, due to an overlap mismatch between the lattice beams, some atoms could be trapped in a single beam. These will not be affected by a moving lattice. The number of untrapped atoms n_free can also vary between experiments.

5.3.2. Parameters

The remaining fitting parameters are:

1. The initial separation of the atom cloud and the sample x_0.
2. The scaling parameter for losses s_L.

3. The scaling parameter for diffusion s_{D}.

4. The initial diffusion due to atom temperature and lattice imperfections D_0.

5.4. Experiments to Model

Different types of experiments are sensitive to different variables, so the variables are fitted to the results of two experiments at the same time. Both experiments are described in Section 4.7.1.

Lattice Loading The first experiment is the Lattice Loading experiment. It is shown in Figure 4.18. For a moving time of $t_{\mathrm{move}} = 10\,\mathrm{ms}$ the lattice is moved down towards the sample. The maximum difference frequency Δf between the two lattice beams, and thus the maximum lattice velocity, is varied to reach different distances. This experiment shows strong losses for short distances moved and is thus susceptible to the loss scaling s_{L}. The decrease in atom number for larger distances moved is highly dependent on the initial height of the atom cloud above the sample x_0.

Diffusion after Motion The second experiment is the first part of Diffusion after Motion, as depicted in Figure 4.21. Within a holding time $t_{\mathrm{hold}} = 10\,\mathrm{ms}$ the lattice is moved down towards the sample for a moving time of $t_{\mathrm{move}} = 3\,\mathrm{ms}$. The motion happens at the beginning ($t_{\mathrm{wait}} = 0\,\mathrm{ms}$) or the end ($t_{\mathrm{wait}} = 7\,\mathrm{ms}$) of the 10 ms holding time. These different conditions for diffusion make the experiment sensitive to the diffusion scaling s_{D} as well as the initial diffusion D_0. A graphical representation of the different times is given in Figure 4.15.

After determining the fitting parameters, two more experiments are used as a benchmark. They are *not* part of the fitting process and they describe different experimental conditions, so they are an independent test of the soundness of the determined parameters.

Crash Curve The first experiment is another Crash Curve like the High Resolution Crash Curve, but with a different set of parameters. The lattice is also moved downwards for $t_{\mathrm{move}} = 3\,\mathrm{ms}$, but with a shorter holding time of $t_{\mathrm{hold}} = 7\,\mathrm{ms}$ and a lower maximum difference frequency Δf between the lattice beams. The atoms move less far and we sample a different regime of the parametric heating frequency spectrum.

Diffusion after Motion The second experiment is the second part of Diffusion after Motion and is described in Figure 4.22. In this experiment the lattice is moved 2 mm in $t_{\mathrm{move}} = 3\,\mathrm{ms}$. This motion always uses the same velocity profile and happens after various waiting times t_{wait} within a holding time of $t_{\mathrm{hold}} = 10\,\mathrm{ms}$. Figure 4.15 depicts the times involved.

5.5. Complexity

Equation 5.5 is the most complex equation in the model. It is solved many times during simulation and fitting and has to be very efficient. The matrix B is only occupied on the primary and secondary diagonals and is thus sparse. This makes it easier to solve. The numerical solver* for equations of the type $x_i : Bx_i = b_i$ with $i = 1, \ldots, N$ is of manageable complexity $O(N)$, with typical values of $N = 2000$. The complexity is analysed in Figure 5.3.

This has to be calculated for every time step during one diffusion run. During the experiment the atom number is measured destructively after the lattice moved for varying distances. The simulation matches this behaviour, so each numerical experiment incorporates multiple diffusion runs.

Furthermore, several experiments can be fitted at the same time. For two experiments, 100 diffusion runs per experiment and 500 time steps per run the equations have to be solved 100 000 times. Combined with the above-mentioned size of the spatial parameter space of $N = 2000$, this makes for a costly fitness function! This poses a problem for classical

* Python: `scipy.sparse.linalg.spsolve`

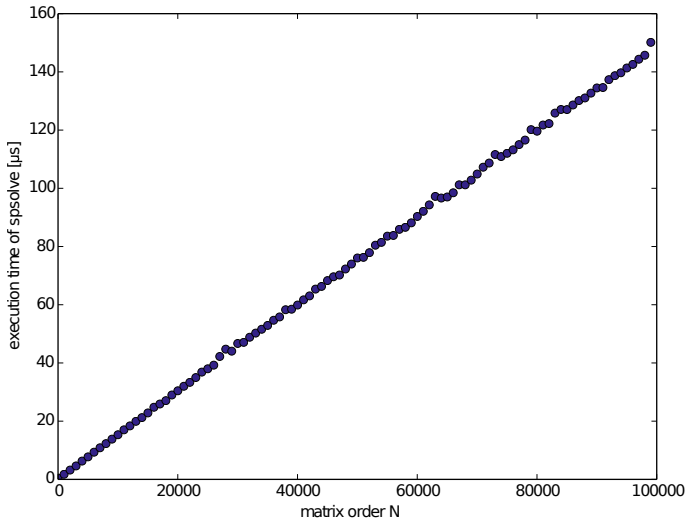

Figure 5.3.: Execution time of `scipy.sparse.linalg.spsolve` for varying matrix orders of a sparse sample matrix. The execution time depends linearly on the matrix order, so the complexity of the task is $O(N)$.

fitting routines like the method of least squares. Fitting for complex fitness functions takes a long time and there is the risk of being trapped in local optima.

5.6. Genetic Algorithm

The challenges mentioned above make Genetic Algorithms (GA)* a good candidate for a fitting routine. They are known for a fast determination of the global minimum in an unknown complex parameter space [SD07].

Each set of experiments starts with a certain "population" of different sets of fitting parameters. This is iterated over many generations, with parameter sets mutating, mating and evolving. Table 5.1 summarizes the

* Python: `pyevolve`

factor	multiplier
time steps	500
runs per experiment	100
number of experiments	2
population	80
generations	100
	800 Million

Table 5.1.: Number of times Equations 5.5, 5.4 and 5.6 have to be solved for the genetic algorithm.

many factors and multipliers.

For a complete fit, the Diffusion Equation 5.5 has to be solved close to 1 billion times. Multiprocessing greatly decreases the time needed. On a current* quad-core standard personal computer this usually takes a couple of days.

GAs have, however, some drawbacks compared to least squares. All the GA specific parameters — such as mutation rate or cross-over rate — have to be determined. GAs also have problems finding the *exact* optimum of the potential landscape, however their solution is a good approximation.

5.7. Least Squares Fit

After running the Genetic Algorithm, the determined parameters can be used as starting parameters for a least squares fit† to zoom into the optimum. The parameters are already close to the optimum, so the least squares fit only takes some hundreds of iterations to converge.

In contrast to the Genetic Algorithm, the least squares fit also provides the covariants for all free parameters. More details can be found in Appendix B.

* as of 2016 † Python: `scipy.optimize.curve_fit`

5.8. Results

As discussed in the previous Sections 5.6 and 5.7 a multi-step approach is used to determine the free parameters. Firstly, the possible parameter ranges are determined either from experiments or by manual diffusion runs. Secondly, a Genetic Algorithm is used to narrow down the free parameters and locate a global optimum. The fitness test of each genome includes a standard least squares fit to determine the experiment-specific parameters n_0 and n_{free}. Thirdly and lastly, the values of the fittest genome are used as starting parameters for a least squares fit. The additional step of separately fitting n_0 and n_{free} is included here as well.

5.8.1. Genetic Algorithm Results

In the terminology of genetic algorithms, the set of variables to optimize is called *genome*. The starting genome G_0 for this specific application consists of the four variables

$$G = [x_0, s_{\text{L}}, s_{\text{D}}, D_0].$$

A set of 80 genomes are allowed to evolve — mutate and crossover — for a total lifetime of 100 generations. Each of the genomes of the starting population has different values for these variables. Apart from these variables shared between experiments, there are "global" fixed parameters as well as fitting parameters individual to each experiment. Table 5.2 lists all of these variables and their allowed ranges, if applicable. Manual diffusion runs or previous experiments are used to determine the ranges.

After 62 generations the fittest genome can not be improved. Its variable values are listed in Table 5.3. Subsequently, in a second fitting step, the respective individual fitting parameters n_0 and n_{free} are used as free parameters in a least squares fit. Figure 5.4 shows the experimental data and diffusion simulation with the fittest genome and best individual parameters. The qualitative behaviour of the experimental data can already be reproduced.

fixed parameters

description	name	value
spatial interval	δx	10 µm
simulation size	$x_{\max}$	20 mm
time steps	N_t	500
sample points	N_{real}	100
atom cloud size	w_0	47 µm

shared fitting variables

description	name	range
atom cloud height above sample	x_0	0.3 to 8 mm
loss scaling	s_{L}	160 to 799 kHz
diffusion scaling	s_{D}	0 to 211 $\text{K}\,\text{s}^{-1}$
initial diffusion	D_0	0 to 21 mK

individual fitting variables

description	name	range
initial atom number "crash"	$n_{0,\text{c}}$	140 000 to 350 000
untrapped atom number "crash"	$n_{\text{free,c}}$	unrestricted
initial atom number "t_{start}"	$n_{0,\text{s}}$	140 000 to 300 000
untrapped atom number "t_{start}"	$n_{\text{free,s}}$	unrestricted

Table 5.2.: Genetic Algorithm parameters

		output parameters	
name	start. range	GA	least squares fit
x_0	0.2–10 mm	2.3 mm	3.4 ± 0.5 mm
s_L	0.16–8 MHz	0.57 MHz	1.0 ± 0.3 MHz
s_D	0–214 K/s	11 K s^{-1}	2.2 ± 0.7 K s^{-1}
D_0	0–21 mK	1 mK	1.1 ± 0.2 mK

Table 5.3.: Starting range and output parameters of the genetic algorithm (GA) and the least squarest fit.

As a benchmark test, the values of the fittest genome are used on two more experimental data sets that are *not* part of the genetic fitting process. Only the experiment-specific variables of n_0 and n_free are used for fitting. Figure 5.5 shows the experimental data and the fits. The trend of the experimental data can be reproduced, albeit not very well.

5.8.2. Least Squares Fit Results

The values of the fittest genome from the Genetic Algorithm are used as starting parameters for the Least Squares fitting. Since the GA found values close to the optimum, it only took the Least Squares fit a few hundred iterations to converge. Table 5.3 lists the final output parameters for the free, shared variables as well as their uncertainties. It is important to keep in mind that the scaling factors s_L and s_D should be viewed in context of the frequency-dependent loss and diffusion functions $L(f)$ and $D(f)$. These functions are both normalized to a maximum value of one. By themselves, s_L and s_D indicate the maximum possible loss and diffusion rate.

The Least Squares Fit results are analysed the same way as the GA results. Figure 5.4 shows the fits. The agreement is much better than with the results of the Genetic Algorithm alone. Figure 5.5 depicts the benchmark test for the Least Squares fit. Fit and data have a much better agreement as well.

In addition to the error in the variables, the covariance matrix of the least squares fit allows for the computation of the variable correlations as well. Analysing the correlation gives insight in how the variables are connected to each other. These are discussed in Appendix C.

5.9. Discussion

The numerical simulations provide answers to a lot of questions. First of all, we can quantify previously unknown variables. The height of the atoms above the sample x_0 eluded previous experimental measurements. Now we can quantify it to be $3.4 \pm 0.5\,\mathrm{mm}$.

Even more important than the fitting parameters is the fact that the macroscopic model is able to capture the features of the experimental data in the first place and that it can forecast the outcome of experiments that were not used in the fitting process. It has predictive power.

The macroscopic model is based on the hypothesis made in Section 5.1.1:

Weak, static lattices induce parametric heating, causing losses and diffusion.

We have now strong evidence that the presence of weak, static lattices perturb the atoms trapped in the moving lattice. Both type of lattices interfere with each other, causing the moving trapping potential to be periodically modulated.

The success of the macroscopic model strongly supports the idea that parametric heating is the cause of the unexpected behaviour during atom transport. A takeaway for experiments that do not require fine-grained control over the atom transport is to avoid the atom losses of the low-frequency regime.

At this point we do not know the origin of the weak, static lattices. Reflections that cause these lattices can originate from other optical elements as well, for example from flat surfaces such as beam splitter cubes or fibre tips. More experiments need to be conducted to find the cause or causes.

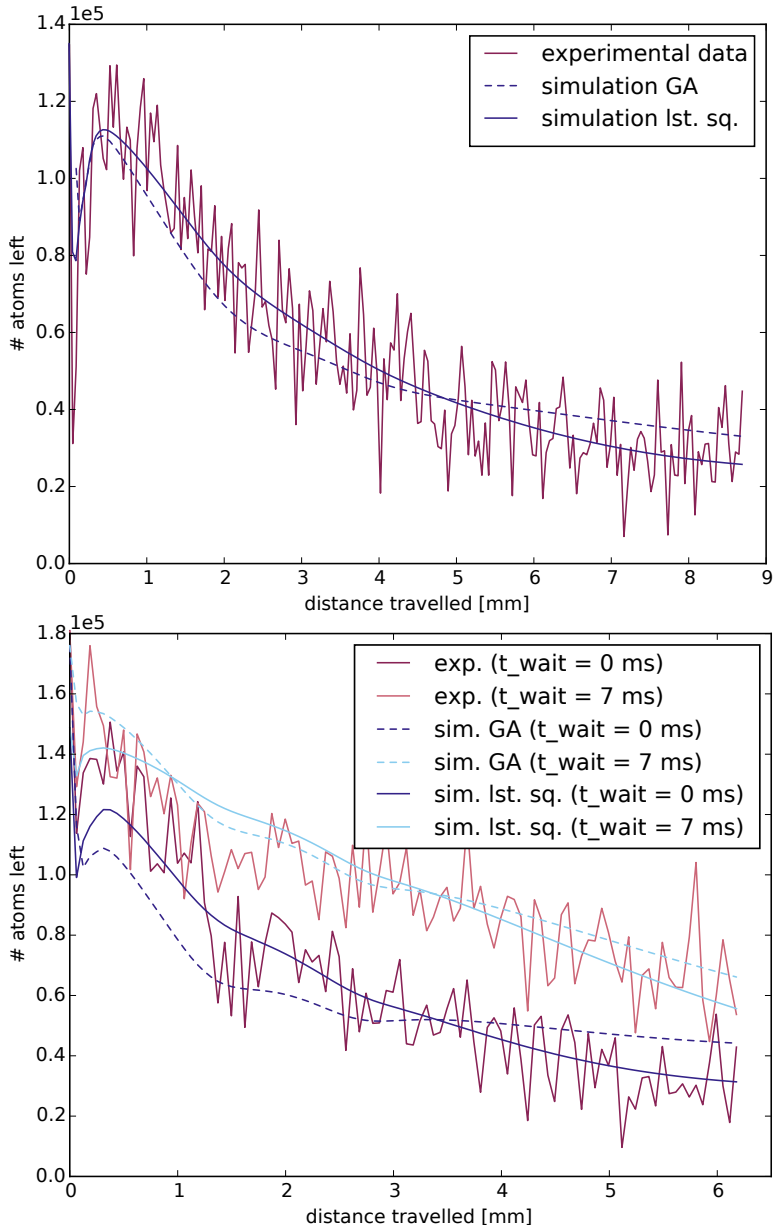

Figure 5.4.: Fitting result from the Genetic Algorithm and Least Squares Fit: diffusion simulation run with the fittest genome and best parameters.

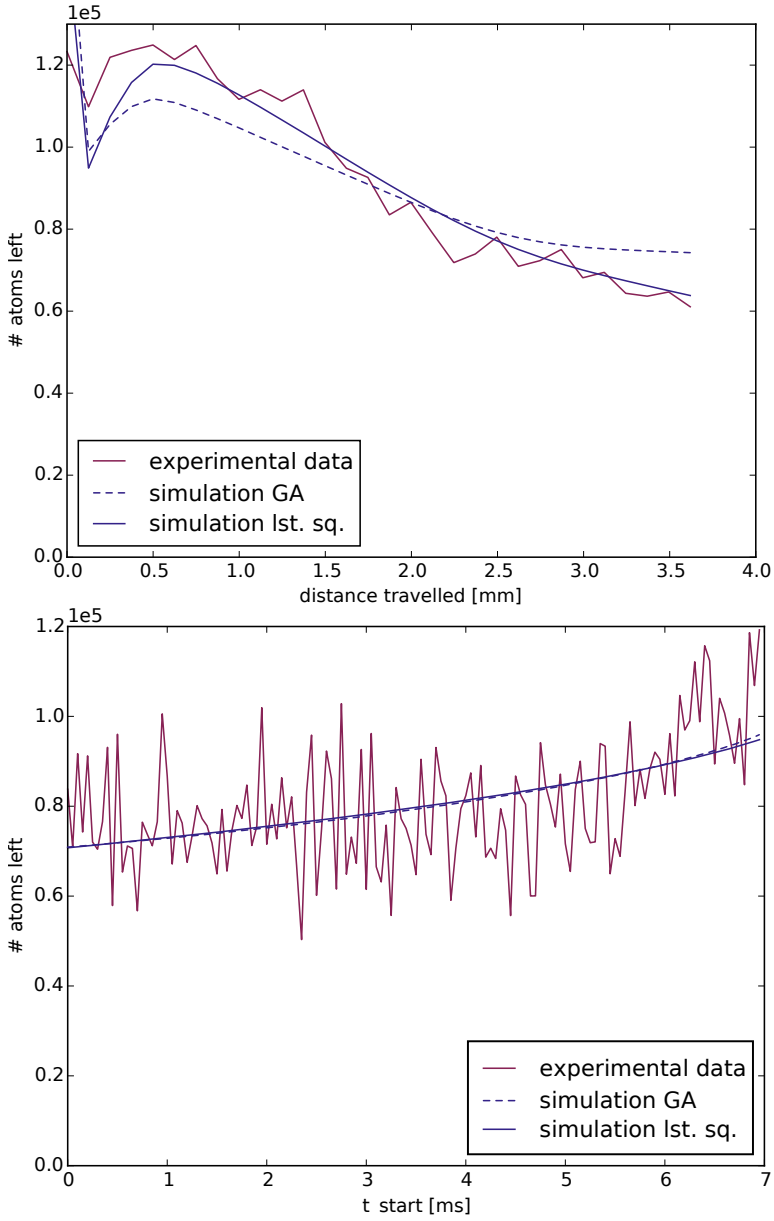

Figure 5.5.: Benchmark test for the Genetic Algorithm and the Least Squares Fit: Diffusion simulation run with the fittest genome and best parameters.

To prevent the atoms from spreading in the lattice, one should avoid rigorously all reflections of lattice light. Optical isolators should be used if possible. It also poses additional restrictions on the choice of sample substrate. Reflecting surfaces should be avoided; anti-reflection coated samples can be used instead. Another approach could be to avoid the substrate during transport altogether and let the lattice pass through a hole in a membrane, sample structure permitting.

Appendices

A. Numerical Diffusion Equation

In the infinitesimal limit, a diffusion equation is rather simple. In Section 5.3.1 we used

$$\frac{\partial n}{\partial t} = C\nabla^2 n, \tag{A.7}$$

with $n(x,t)$ being the number of atoms per lattice site in the conveyor and C being the diffusion matrix. Numerical models work with a discretized time and space domain, so an adapted version of Equation A.7 has to be used.

Both variables x and t are discretized as depicted in Figure A.6 such that

$$x \to x_i = i\,\delta x$$
$$t \to t_j = j\,\delta t.$$

The density is evaluated on the grid spanned by x_i and t_j and is denoted by the abbreviation

$$n_{i,j} = n(x_i, t_j).$$

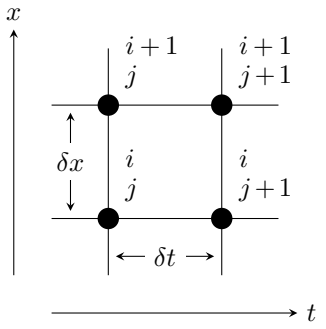

Figure A.6.: Discretization

Leonhard Euler described in his work *Institutiones Calculi Integralis I* (1768, Caput VII) a method to approximate differentiation [Eul68, HNW08]. His idea was to divide the interval of integration and approximate the solution within each subinterval by the first term of its Taylor series. This now-called Euler method is used to numerically solve Equation A.7.

A.1. Discretizing the Diffusion Equation

By the definition of derivation, a single derivative can also be written as

$$\frac{\partial n}{\partial x} = \lim_{\Delta x \to 0} \frac{\Delta n}{\Delta x}.$$

Following the same rationale, the second derivative will be

$$\frac{\partial^2 n}{\partial x^2} = \lim_{\Delta x \to 0} \frac{\Delta \frac{\partial n}{\partial x}}{\Delta x}.$$

As an intermediate step, the spatial derivative of n between grid points centred around (x, t) would be

$$\left.\frac{\partial n}{\partial x}\right|_{x_{i+1/2}, t_j} = \frac{n_{i+1,j} - n_{i,j}}{\delta x}$$

$$\left.\frac{\partial n}{\partial x}\right|_{x_{i-1/2}, t_j} = \frac{n_{i,j} - n_{i-1,j}}{\delta x}.$$

Using this, the second spatial derivative at (x, t) results to

$$\left.\frac{\partial^2 n}{\partial x^2}\right|_{x_i, t_j} = \frac{\left.\frac{\partial n}{\partial x}\right|_{x_{i+1/2}, t_j} - \left.\frac{\partial n}{\partial x}\right|_{x_{i-1/2}, t_j}}{x_{i+1/2} - x_{i-1/2}} = \frac{n_{i+1,j} - 2n_{i,j} + n_{i-1,j}}{(\delta x)^2}. \quad \text{(A.8)}$$

The same line of thoughts can be applied for the time derivative, so we can write analogously

$$\left.\frac{\partial n}{\partial t}\right|_{x_i, t_j} = \frac{n_{i,j+1} - n_{i,j}}{\delta t}. \quad \text{(A.9)}$$

Using Equations A.8 and A.9, the discretized diffusion equation can be written to

$$\frac{n_{i,j+1} - n_{i,j}}{\delta t} = c_{i,i'} \frac{n_{i+1,j} - 2n_{i,j} + n_{i-1,j}}{(\delta x)^2}$$

$$n_{i,j+1} = n_{i,j} + c_{i,i'} \frac{\delta t}{(\delta x)^2} \left(n_{i+1,j} - 2n_{i,j} + n_{i-1,j}\right), \quad \text{(A.10)}$$

with $c_{i,i'}$ being the coefficients of C. This iteration through time-steps can be also written in matrix form. We use a few assumptions. The

diffusion matrix is diagonal, spatially constant and only changes in time. We can thus treat its coefficients as scalars $c_{i,i'} = c(t)$. Furthermore, the boundaries are lossy; all atoms outside the grid area are lost. Using the Einstein notation we can write Equation A.10 as

$$\begin{aligned} n_{i,j+1} &= \frac{\delta t}{(\delta x)^2} \begin{pmatrix} 1-2c & c & 0 & \cdots \\ c & 1-2c & c & \cdots \\ 0 & c & 1-2c & \cdots \\ \vdots & \vdots & \vdots & \ddots \end{pmatrix} n_{i,j} \\ &\equiv \frac{\delta t}{(\delta x)^2} A_{ii'}\ n_{i',j}. \end{aligned} \tag{A.11}$$

The matrix $\frac{\delta t}{(\delta x)^2} A$ plays a role in the stability of solving the above differential equation. Solving the *explicit* formulation used in Equation A.11 is only conditionally stable for satisfying the Courant-Friedrichs-Lewy condition [Ise09, HF01]

$$\frac{\delta t}{(\delta x)^2} A_{ii'} \leq \frac{1}{2}$$

for all grid points i. Especially the square contribution $(\delta x)^2$ poses computationally expensive restrictions on the choices of the time- and spatial steps. For doubling the spatial resolution $\delta x' = 2\,\delta x$ we need to quadruple the time resolution $\delta t' = 4\,\delta t$ to achieve the same stability. This leads to an overall increase of complexity by a factor of eight for doubling the spatial resolution.

Instead, the unconditionally stable *implicit* formulation can be used [HF01]. It is important to clearly separate the stability of the process and the error of the solution. Though different in stability, the error of both the implicit and explicit Euler method are equal in magnitude, yet opposite in sign [GP08]. With absorbing the prefactor into the matrix $B = \frac{\delta t}{(\delta x)^2} A$ the explicit equation is of the form

$$n_{i,j+1} = B_{ii'}\ n_{i',j},$$

whereas the implicit formulation would be written as

$$\left[B^{-1}\right]_{ii'}\ n_{i',j+1} = n_{i,j}. \tag{A.12}$$

A.2. Discretizing Losses and Changes in Diffusion

By using the above described method, it is now trivial to discretize the Differential Equations 5.2 and 5.3 for the atom density n and the diffusion matrix C, respectively, to

$$\frac{\partial C}{\partial t} = s_{\mathrm{D}} D(f) \quad \Longrightarrow \quad B_{i,j+1} = B_{i,j} + s_{\mathrm{D}} D(f)\, \delta t \tag{A.13}$$

$$\frac{\partial n}{\partial t} = -s_{\mathrm{L}} L(f)\, n^2 \quad \Longrightarrow \quad n_{i,j+1} = n_{i,j} - s_{\mathrm{L}} L(f)\, n_{i,j}^2\, \delta t. \tag{A.14}$$

For performance reasons we mix implicit and explicit equations, so for every time step δt the Equations A.12 to A.14 are applied sequentially. Firstly Equation A.13 is solved. This temperature equation determines the new diffusion constant. Secondly Equation A.12 is solved. It applies diffusion and determines the new density distribution. In a third step the Equation A.14 is solved, it applies frequency-dependent losses. During a fourth and last step, the atom distribution is truncated where the atoms hit the sample surface. This is treated as a hard edge, so no equations have to be solved for this step.

B. Covariant Matrix

For a number of z parameters, the covariant matrix M_{cov} is of dimension $(z \times z)$ and has the form

$$M_{\text{cov}} = \begin{pmatrix} \sigma_{11} & \sigma_{12} & \cdots & \sigma_{1z} \\ \sigma_{21} & \sigma_{22} & \cdots & \sigma_{2z} \\ \vdots & \vdots & \ddots & \\ \sigma_{z1} & \sigma_{z2} & & \sigma_{zz} \end{pmatrix}.$$

With E being the expected value operator, the covariants are defined as [Dee06]

$$\sigma_{xy} = E\left[(X - E[X])\,(Y - E[Y])\right].$$

The on-diagonal element $\sigma_{xx} = E\left[(X - E[X])^2\right] \equiv \sigma_x^2$ is the variance of variable x and the square of its standard deviation. Normalizing the covariants with their corresponding variances yields the correlation coefficients

$$\rho_{xy} = \frac{\sigma_{xy}}{\sqrt{\sigma_{xx}\sigma_{yy}}}.$$

The correlation coefficients will be $-1 \leq \rho \leq 1$. Its sign indicates correlation (+) or anti-correlation (–), whereas the magnitude is a measure of its strength. The correlation coefficients can also be expressed as a matrix

$$M_{\text{cor}} = \begin{pmatrix} 1 & \rho_{12} & \cdots & \rho_{1z} \\ \rho_{21} & 1 & \cdots & \rho_{2z} \\ \vdots & \vdots & \ddots & \\ \rho_{z1} & \rho_{z2} & & 1 \end{pmatrix}.$$

Here the on-diagonal elements equal trivially to one. Both the covariant matrix and correlation matrix are symmetric around the main diagonal with $\sigma_{xy} = \sigma_{yx}$ and $\rho_{xy} = \rho_{yx}$.

C. Correlation Analysis

The correlation matrix in Table C.1 can be used to examine if the model behaviour matches our intuitive understanding of the involved physics. Both the initial diffusion D_0 and the diffusion scaling s_D contribute positively to diffusion. When increasing one of them, the other has to be lowered to produce a similar diffusion curve. They should thus be anticorrelated. Their correlation factor of -0.53 confirms this.

The losses in the system scale with the number of atoms squared n^2. A higher initial diffusion D_0 will lower the atom density, so a higher loss scaling s_L is necessary to keep the losses comparable. With a correlation factor of 0.42 these variables are understandably correlated.

The relationship between the loss scaling s_L and the diffusion scaling s_D is a bit more complicated. The loss scaling s_L needs to be higher for higher diffusion. But both s_D and D_0 contribute to diffusion, and they are anticorrelated! One of these, however, has to dominate. It is now important to remember that s_D has little influence on lower lattice difference frequencies, i.e. shorter distances travelled, the only region where the losses are important. For short distances travelled, D_0 has a higher influence on the diffusion. s_D and s_L are thus weakly anticorrelated with a correlation factor of -0.35.

Diffusion and the height of the atom cloud above the sample x_0 are closely connected. For a higher x_0 the diffusion has to be higher as well to have a comparable loss rate through atoms crashing into the sample. The height x_0 should thus be correlated with the diffusion and one of the diffusion scaling s_D or the initial diffusion D_0 has to dominate. The influence of x_0 gets large at higher lattice difference-frequencies, i.e. higher distances travelled, when the atoms actually start to hit the sample sur-

	x_0	s_L	s_D	D_0
x_0	1	-0.56	0.79	-0.69
s_L		1	-0.35	0.42
s_D			1	-0.53
D_0				1

Table C.1.: Correlations of the shared variables.

face. In this regime, the initial diffusion D_0 is not so important anymore and s_D gains influence. x_0 is therefore strongly correlated with s_D and strongly anticorrelated with D_0 with correlation factors 0.79 and -0.69, respectively.

The loss scaling s_L and x_0 have no direct connection. The former influences the low-frequency regime, whereas the latter works predominantly in the high-frequency regime. The height x_0 is, however, strongly correlated to s_D, which is anticorrelated to s_L. At the same time, x_0 is strongly anticorrelated to s_D, which is correlated to s_L. Both of these influences cause x_0 to have an anticorrelation with s_L with a correlation factor of -0.56.

The correlation behaviour of the shared variables is comprehensible and gives affirmation that the numerical model behaves correctly.

Summaries

1. Samenvatting in het Nederlands

In dit proefschrift introduceren wij een opstelling om koude atomen te verplaatsen tot in de nabijheid van nano-fotonische structuren. Deze korte uitspraak roept een hoop vragen op. Hoe brengen we de atomen en nano-fotonische structuren bij elkaar en wat zal hun onderlinge afstand zijn? Waarom moeten de atomen koud zijn? Wat is koud genoeg? Wat zijn nano-fotonische structuren en waarom zijn ze zo interessant? En, als belangrijkste vraag: Waarom doen we dit onderzoek en wat hopen we te leren?

Atomen Alles om ons heen wat we kunnen zien, voelen en ademen bestaat uit atomen. Deze bouwstenen der materie kunnen in verschillende fundamentele toestanden voorkomen: vast, vloeistof en gas. Voor onze experimenten gebruiken wij rubidium atomen in gas vorm. Op kamertemperatuur zijn deze atomen verrassend snel. Ze hebben snelheden rond de 860 km/uur*. Voor onze experimenten willen wij de atomen op dezelfde plaats houden als onze nano-fotonische structuren. Aangezien de atomen zich voortbewegen met bijna supersonische snelheden moeten wij ze dus eerst afremmen. Dit bereiken wij door ze af te koelen.

Koeling Voor atomen geldt dat hoe hoger hun temperatuur is, des te groter is hun kinetische energie en daarmee hun snelheid. Om de kinetische energie te verlagen gebruiken wij licht. Dit staat bekend als laser koeling.

* $v_{\mathrm{th}}(T = 293\,\mathrm{K}) = \sqrt{\frac{2k_{\mathrm{B}}293\,\mathrm{K}}{m_{\mathrm{Rb}}}} = 239\,\mathrm{m/s} \mathrel{\hat{=}} 860\,\mathrm{km/uur}$

Licht bestaat uit fotonen die een energie hebben overeenkomend met hun kleur. Fotonen aan de blauwe zijde van het regenboog spectrum hebben een hogere energie dan fotonen aan de rode zijde. Atomen kunnen alleen fotonen van een zeer specifieke kleur absorberen omdat de elektronen van de atomen alleen gequantiseerde energie toestanden kunnen aannemen. Dit is te vergelijken met trap lopen; hoe hoger de tree, des te hoger is de energie. Net zoals dat het niet mogelijk is om tussen twee treden te staan is het voor een elektron niet mogelijk om zich tussen twee gequantiseerde energie toestanden te bevinden. Atomen kunnen dus licht absorberen als de energie van het inkomende foton overeenkomt met dat van een van de energie niveaus van een elektron. Wij zeggen in dit geval ook wel dat de frequentie van het foton "op resonantie" is met het atoom. Het impuls van het foton wordt hierbij overgedragen aan het atoom.

Door naast het absorberen van fotonen ook het Doppler effect te benutten kunnen de atomen gekoeld worden. Het Doppler effect is de verandering in waargenomen frequentie van bewegende bronnen van geluid of licht. De verandering in de toon van een ambulance sirene als deze voorbij rijdt vindt ook plaats voor licht. Met laser koeling wordt een atomair gas beschenen met rood verstemd licht. Dit is licht waarbij de foton energie zo gekozen is dat deze onder één van de elektron energie niveaus ligt. Een atoom dat van een lichtbron, bijvoorbeeld een laser, af beweegt ondervindt door het Doppler effect een lagere licht frequentie en een lagere foton energie. Wanneer het atoom richting de lichtbron toe beweegt ondervindt het fotonen met een hogere foton energie. Nu is het foton op resonantie met het atoom en kan het geabsorbeerd worden. De impuls van het foton wordt overgedragen aan het atoom waarbij zijn kinetische energie wordt verminderd.

Door nu het atoom van alle richtingen met rood verstemd licht te beschijnen zal het atoom altijd tegen de propagatie richting van de fotonen bewegen. Het atoom zal dus in alle richtingen worden afgeremd wat de thermische energie verlaagd. Door middel van de absorptie van het foton impuls kunnen de atomen worden afgekoeld tot enkele millikelvins. Dit is een duizendste van een graad Celsius boven het absolute nulpunt van

$-273.15\,^{\circ}\mathrm{C}$. Doordat de atomen een stuk minder beweeglijk zijn, kunnen we ze tevens een stuk makkelijker vangen.

Vangen Om de atomen te vangen maken we gebruik van het effect "lichtverschuiving" dat niet van foton absorptie afhangt. Om dit effect uit te leggen moeten we het atoom nader bekijken. Dit bestaat uit een positief geladen nucleus omringd door negatief geladen elektronen. Zonder externe invloeden is het atoom niet gepolariseerd waardoor de elektronen wolk uniform verdeeld is rondom de nucleus.

Onder invloed van een elektrostatisch veld worden de elektronen en de nucleus elk in tegenovergestelde richting getrokken. Ze trekken elkaar echter nog steeds aan waardoor het moeilijk is om ze te scheiden. Het elektrostatische veld trekt ze uit elkaar tot het punt dat het veld net zo hard de elektronen en nucleus uit elkaar trekt als dat zij onderling aan elkaar trekken. Er stelt zich een evenwicht in waarbij het atoom zijn energie heeft verlaagd.

Als dit atoom wordt beschenen met licht dat te ver in het rood is verstemd zal het geen fotonen absorberen. Het elektromagnetische veld van het licht zal echter wel een kracht uitoefenen op zowel de elektronen als de nucleus. Deze zullen beide heen en weer bewegen en, met een lage frequentie het veld van het licht volgen. In dit geval reageert het atoom in fase met het veld. Onder deze omstandigheden verlaagd het atoom dus zijn energie wat een gunstige situatie voor het atoom is. Nu geldt dat hoe hoger de intensiteit van het licht, des te lager de energie van het atoom zal zijn. Het atoom wordt dus aangetrokken tot regio's van hoge intensiteiten van rood verstemd licht.

Voor blauw verstemd licht gebeurd het omgekeerde. Hoe "blauwer" het licht, des te hoger de frequentie van de fotonen. Het elektromagnetische veld is nu te snel voor het atoom om te volgen. De ladingen worden zo snel heen en weer getrokken dat ze altijd net te laat zijn om te volgen. Het atoom oscilleert nu uit fase met het gedreven veld. Dit betekent dat het atoom gepolariseerd is tegen het externe veld waardoor zijn energie nu hoger is. Dit is niet gunstig en dus zal het atoom de lage intensiteit

regio's opzoeken.

Samengevat, het atoom wordt aangetrokken door rood verstemd licht en afgestoten door blauw verstemd licht. We kunnen nu dus een val voor de atomen maken door een rood verstemde laser bundel te focusseren. De atomen worden aangetrokken door de hoge intensiteit regio's van het veld in het focus. Door deze bundel te bewegen of door het veld te manipuleren kunnen we de atomen zelfs bewegen aangezien ze de hoge intensiteit regio's zullen volgen. Dit is het mechanisme om de atomen te verplaatsen naar het oppervlak van de nano-fotonische structuren.

Nanofotonica In de nanofotonica wordt licht op de nanoschaal bestudeerd. In ons alledaagse leven zien we licht misschien als iets dat in een rechte lijn beweegt over macroscopische afstanden. Zodra we echter naar nanoschalen gaan gedraagt licht zich alles behalve intuïtief. Licht kan bijvoorbeeld opgesloten worden met behulp van spiegels. Twee parallelle spiegels kunnen licht begeleiden door het simpelweg tussen hen heen en weer te laten reflecteren. Dit is in principe hoe optische fibers met een grote kern werken. Om ervoor te zorgen dat het licht in de kern van de fiber blijft reflecteert het licht continue aan de grens tussen de kern aan de binnenkant en de bekleding aan de buitenkant van de fiber. Zelfs wanneer de fiber gebogen wordt blijft het licht in de kern van de fiber. Wanneer de kern nu kleiner wordt, reflecteert en veranderd de richting van het licht niet meer. Het volgt de kern als water in een tuinslang. Wanneer de fiber zelfs nog dunner wordt zal er op een gegeven moment licht uit de fiber lekken waardoor het licht ook deels zich *aan de buitenkant van de fiber* voortbeweegt. Dit licht noemen wij een "evanescente golf" of "uitdovende golf". In termen van de tuinslang analogie zou het water nu over de buitenkant van de tuinslang lopen. Wanneer de fiber weer groter wordt zal het licht weer terug de fiber in gaan.

Er zijn ook andere manieren om een evanescente golf te creëren. Met behulp van roosters kan dit bijvoorbeeld worden opgewekt aan het oppervlak van metalen. Een rooster breekt een inkomende laserstraal zodanig dat deze parallel aan het metaal oppervlak propageert. Het licht koppelt

aan elektron golven aan het oppervlak. Samen vormen zijn een quasi-deeltje dat wij een *Oppervlakte Plasmon Polariton* noemen. In vergelijking met het licht aan het oppervlak van een fiber heeft een Oppervlakte Plasmon Polariton een veel strakkere ruimtelijke opsluiting en een hoger lokaal veld intensiteit. Ze vervallen echter wel sneller door bijvoorbeeld Ohmische verliezen in het metaal net zoals stroom door een draad.

Gezien het feit dat licht over het oppervlak van metalen kan propageren zorgt dit ervoor dat we nano-fotonische apparaten kunnen bouwen die met atomen kunnen wisselwerken. Licht kan gebruikt worden om atomen op te slaan, te manipuleren of te koppelen. Met nano-fotonische structuren is het mogelijk om een ingewikkeld potentiaal landschap te creëren met zeer hoog gelokaliseerde velden en sterke gradiënten voor interacties tussen licht en atomen. De kleine afmetingen van de nano-fotonische structuren hebben meerdere voordelen. Zo passen er bijvoorbeeld vele structuren op een enkel sample waarbij ze nog steeds met elkaar kunnen communiceren. Het schaalt erg gemakkelijk. Ook kunnen interacties tussen verschillende structuren heel snel zijn omdat alle elementen zeer dicht op elkaar kunnen zitten.

Toepassingen Wat hebben we aan dit onderzoeksonderwerp? Nanofotonica bestudeerd licht op de nanoschaal. Simpel gezegd brengt het de kracht van optica naar apparaten zo groot als chips. Hiernaast maken ze ook eigenschappen als hoge lokale intensiteiten en sterke gradiënten meer toegankelijk. Deze extreme toestanden van licht zorgen voor snelle en zeer gevoelige meetapparaten. Nanofotonica maakt het mogelijk om schaalbare systemen te ontwerpen aangezien meerdere fotonische systemen snel met elkaar kunnen reageren.

Het combineren van nanofotonica en koude atomen schept een groot aanbod van vooruitzichten. Het blootstellen van atomen aan extreme toestanden van licht geeft toegang tot sterke koppeling tussen licht en materie, een eis voor quantum informatie verwerking. Fundamenteel gezien manipuleert sterke koppeling aspecten van materie en maakt het mogelijk om elektronische energie niveaus te bouwen. De nanofotonica maakt het

ook mogelijk om emissie processen te versnellen van atomen als enkele foton emitters.

De schaalbaarheid van de nanofotonica heeft zich inmiddels uitgebreid naar de atoom fysica. Atomen kunnen worden gevangen, gekoppeld en gemanipuleerd op zeer kleine schalen en in grote getallen. Bovendien is het potentiaal landschap voor atomen zeer aanpasbaar.

Inzichten Wat hopen we te leren? Het voornaamste is het onderzoeken van nieuwe interacties tussen licht en materie. We kunnen dit nu op een zeer flexibele manier doen. De opstelling staat ons toe vele verschillende typen samples te gebruiken. Fotonische of plasmonische samples met metalen vliesjes of halfgeleider membranen, golfgeleiders of resonatoren kunnen binnen twee dagen verwisseld zijn.

Het doel is om in rap tempo vele verschillende experimenten uit te voeren. Op deze manier kunnen we meerdere interessante onderwerpen beslaan en gebruik maken van hun synergie effecten.

Dit proefschrift Dit proefschrift begint met een formele introductie in het onderzoeksgebied in Hoofdstuk 1. Het daarop volgende Hoofdstuk 2 beschrijft een mogelijk experiment dat zou kunnen worden uitgevoerd met de opstelling. Tevens beschrijft het mogelijke handelswijzen voor de onderzoekers die mij zullen opvolgen. De opstelling is in detail beschreven in Hoofdstuk 3 en gekarakteriseerd in Hoofdstuk 4. Het bleek dat de bouw van de opstelling tamelijk ingewikkeld was. We zijn in staat atomen te verplaatsen naar het oppervlak van een structuur. Echter is dit met minder precisie dan noodzakelijk is voor de geplande experimenten. Hoofdstuk 5 beschrijft een tweedelige numerieke simulatie om ons te helpen te begrijpen wat er gebeurt tijdens het transport van atomen onder realistische experimentele condities. De simulatie beschrijft inderdaad het fenomeen dat wij in het experiment waarnemen en levert waardevolle inzichten op die de momentele tekortkomingen kunnen oplossen. We hebben nu een goed begrip wat betreft welke type experimenten haalbaar zijn en welke grens condities van toepassing zijn.

Vooruitblik De numerieke simulaties hebben ons een aantal dingen geleerd die nog verbeterd kunnen worden. In het algemeen zijn we er bijna: We hebben een vacuümkamer met een mechanisme om snel van sample te kunnen wisselen. Binnenin de vacuümkamer kunnen we een zeer puur gas van rubidium atomen afkoelen en beheersen tot millikelvin temperaturen. De atomen kunnen worden afgeleverd bij het oppervlak van een sample en we hebben gewerkt aan meerdere proefonderzoeken met verschillende nano-fotonische structuren. Vele experimenten zullen mogelijk zijn zodra het atoom transport is verfijnd. Ik kan niet wachten op de contributies van de volgende generatie in deze opwindende tak van de wetenschap.

2. Summary in English

In this thesis we present an apparatus to bring cold atoms in close proximity to nanophotonic structures. There are a lot of questions attached to this short statement. How do we bring them together and how close will they be? Why do the atoms need to be cold? How cold? What are nanophotonic structures and what makes them so interesting? And the most importantly: Why do we do this, what do we expect to learn in the process?

Atoms Everything that we can see, touch or breathe is made of atoms. These tiny building blocks of matter can adopt different fundamental states: solid, liquid and gas. In our experiments we use rubidium in gaseous form. At room temperature, the atoms in a cloud of rubidium are surprisingly fast. They have a speed around 860 km/h*. We want to keep the tiny atoms in the same place as tiny nanophotonic structures to do experiments, but they fly around at almost Mach speed. This is why we have to slow them down. We do this by cooling them.

Cooling The higher the temperature of the atoms, the higher their kinetic energy, or their speed. To bring down their kinetic energy, we brake them down with light. This is called laser cooling.

The quantizations of light, called photons, have energies corresponding to their colour. Photons on the blue side of the rainbow spectrum have a higher energy than photons on the red side. Atoms can only absorb photons of very specific colours, because the electrons of atoms can adopt only quantized energy states. It's like standing on stairs; the higher the step, the higher the energy. And just like you cannot stand between two steps of stairs, the electron cannot be between two of these quantized energy states. Atoms can absorb light when the energy of an incoming photon matches one of the energy steps of an electron, when the photon

* $v_{\mathrm{th}}(T = 293\,\mathrm{K}) = \sqrt{\frac{2k_{\mathrm{B}}293\,\mathrm{K}}{m_{\mathrm{Rb}}}} = 239\,\mathrm{m/s} \mathrel{\hat{=}} 860\,\mathrm{km/h}$

frequency is "on resonance" with the atom. The momentum of the photon is then transferred onto the atom.

How can this be used to cool atoms? By exploiting the Doppler effect. The Doppler effect is the change in perceived frequency for moving sources of sound or light. The change in siren tone when an ambulance passes, also happens with light. For laser cooling, a cloud of atoms is exposed to red-detuned light; this is light with photon energies slightly below one of the electron energy steps. An atom moving away from a source of light, for example a laser, experiences a lower light frequency and a lower photon energy. An atom moving towards a light source experiences photons with a higher photon energy. Here the photon is actually on resonance with the atom and can be absorbed. The momentum of the photon is then transferred onto the atom, reducing its kinetic energy.

By exposing the atom to red-detuned light from all sides, the atom will always move against some light. The atom is then slowed down in all directions, reducing its thermal energy. By absorbing photon momenta, the atom can be cooled below millikelvins. That is less than one thousandth of a degree above the absolute minimum of $-273.15\,°\mathrm{C}$. This also makes them easier to trap.

Trapping The effect used for atom trapping is called "light-shift" and does not rely on photon absorption. To explain it, we first need to have a closer look at the atom itself. It consists of a positively charged nucleus surrounded by negatively charged electrons. Without any external influence the atom is not polarized so that the electron cloud is uniformly distributed around the nucleus.

When exposed to an electrostatic field, the electrons are pulled to one side and the nucleus to the other. They are still attracted to each other, so they cannot easily separate. The electrostatic field drags them apart until it pulls just as hard as the electrons and the nucleus attract each other. The atom is now in equilibrium with its surroundings and has lowered its energy.

If the atom is exposed to far red-detuned light then the atom will not

absorb photons, but the electromagnetic field of the light will exert a force on the electrons and the nucleus. They will move back and forth at a low frequency, following the field of the light. It is said that the atom responds in-phase with the field. In this surroundings the atom thus lowers its energy, which is a preferable state. The higher the light intensity, the lower the atom energy. The atom is attracted to regions with a high intensity of red-detuned light.

For blue-detuned light, the opposite will happen. The "bluer" the light, the higher is the frequency of the photons. Now the electromagnetic field is too fast for the atom to follow. The charges are pulled back and forth so fast that they are always a bit too late to follow. The atom oscillates now out-of-phase with the driving field. This means that the atom is polarized against the external field, so its energy is actually higher than before. This is not favourable, so the atom seeks the low-intensity regions.

In essence, the atom is attracted to red-detuned light and repelled by blue-detuned light. One can now create an atom trap by simply focusing a red-detuned laser beam. The atoms will be attracted to the high-intensity field regions in the focus. By steering the beam or manipulating the field we can even transport the atoms, since they will follow the high intensity. This is the mechanism used to bring the atoms onto the surface of the nanophotonic sample.

Nanophotonics The field of nanophotonics deals with the study of light at the nanoscale. In our everyday lives we think about light as something that travels in a straight line, over macroscopic distances. However, confined to nanoscales it starts to behave unintuitive. Light can be confined for example by mirrors. Two parallel mirrors can guide light, which bounces back and forth between them. That is how large-core optical fibres work. The light is kept inside the core by continuously being reflected on the boundary of the core on the inside and the cladding on the outside of the fibre. The light stays inside, even in a bent fibre. When the core gets smaller, the light actually does not reflect or change path anymore. It follows the core like water in a garden hose. If the fibre gets

even thinner, at some point the light starts to leak out and partly travel *on the outside of the fibre*. This light is called "evanescent light". In the garden hose analogy, the water now would run on the outer surface of the hose. When the fibre gets bigger again, the light comes back inside.

There are more ways to create evanescent light. With the help of gratings, it can be launched on the surface of metals. A grating diffracts an incoming laser beam such that it propagates parallel to the metal surface. The light couples to electron waves on the surface. Together they form a quasi-particle called *Surface Plasmon Polariton*. Compared to light on a fibre surface the Surface Plasmon Polariton has a tighter spatial confinement and a higher local field intensity. They do, however, decay quicker due to for example Ohmic losses in the metal, just like current in a wire.

The fact that light can propagate on the surface of matter enables building nanophotonic devices that can interact with atoms. This light can be used to store, manipulate, or couple atoms. With nanophotonic structures one can tailor very intricate potential landscapes for light-atom interactions with highly localized fields and strong gradients.

The small size of the nanophotonic structures has multiple benefits. Many structures can be on the same sample and interact with each other; it scales well. Interactions between structures can be extremely fast, since all elements can be very close to each other.

Applications What is the prospect of this research topic? What is there to gain from it? Nanophotonics studies light at the nanoscale. It brings the power of optics to chip size, while additionally making features such as high local intensities and strong gradients more accessible. These extreme states of light allow for fast and highly sensitive measuring devices. Nanophotonics allows for designing highly scalable systems, since many photonic systems can quickly interact with each other.

Combining nanophotonics with cold atoms offers a plethora of prospects. Exposing atoms to extreme states of light gives access to strong coupling of light and matter, a pre-requisite for quantum information processing. Strong coupling fundamentally manipulates matter and enables engineer-

ing of electronic energy levels. Nanophotonics can also accelerate single-photon emission processes of atoms.

The scalability of nanophotonics now extends to atomic physics. Atoms can be trapped, coupled and manipulated at very small length scales, and in large numbers. Moreover, the potential landscape for the atoms is highly customizable.

Insights What do we expect to learn from this project? The primary aspect is studying new ways of light-matter interaction. We can do this in very flexible ways. The setup allows for very different types of samples. Photonic or plasmonic samples with membranes, waveguides or resonators can be exchanged within two days.

The aim is to conduct different types of experiments in quick succession. That way we can cover multiple interesting topics and make use of their synergy effects.

Thesis Content The thesis begins with a formal introduction into the field of research in Chapter 1. The following Chapter 2 describes a sample experiment that could be conducted in the experimental setup. It also describes possible next approaches for the researchers following my footsteps. The setup is described in detail in Chapter 3 and characterized in Chapter 4. It turned out that building such an apparatus is quite intricate. We can deliver atoms to the sample surface, but with less control than necessary. Chapter 5 deals with a two-step numerical simulation to help explaining what is actually happening during the atom transport under experimentally realistic conditions. The simulation indeed captures the phenomena that we encounter and gives valuable insight for resolving the current shortcomings. We now have a good understanding of what types of experiments are feasible and what boundary conditions apply.

Next Steps The numerical simulation taught us a few things that can be improved. In general we are almost there: we have a vacuum chamber with a fast sample-exchange mechanism. Inside the chamber we can

cool and control clouds of very pure rubidium atoms down to millikelvin temperature. The atoms can be delivered to a sample surface and we worked on pilot studies with various nanophotonic structures. Once the atom transport is refined, many more experiments are possible. I cannot wait to see what the next generation will contribute to this exciting field of science.

3. Deutsche Zusammenfassung

Diese Doktorarbeit beschreibt einen experimentellen Aufbau, mit dem wir gekühlte Atome in die Nähe von nanophotonischen Strukturen bringen können. Dieser kurze Satz wirft eine Menge Fragen auf: Wie bringen wir die Atome und nanophotonische Strukturen zusammen und wie nah? Warum müssen die Atome gekühlt werden und wie kalt müssen sie sein? Was sind nanophotonische Strukturen und was macht sie so interessant? Und am wichtigsten: Warum tun wir das überhaupt, was wollen wir dabei lernen?

Atome Alles was wir sehen, anfassen oder atmen, all dies besteht aus Atomen. Diese winzigen Bausteine der Materie treten in unterschiedlichen Aggregatszuständen auf: Fest, flüssig und gasförmig. Für unsere Experimente gebrauchen wir gasförmiges Rubidium. Bei Raumtemperatur sind die Atome in einer Rubidium Gaswolke erstaunlich schnell. Sie können Geschwindigkeiten von bis zu 860 km/h* erreichen. Die kleinen Atome sollen in der Nähe von kleinen nanophotonischen Strukturen bleiben, sie fliegen jedoch mit beinahe Überschallgeschwindigkeit. Deshalb müssen wir sie abbremsen und das tun wir, indem wir sie kühlen.

Kühlen Je heißer die Atome, desto höher ist ihre kinetische Energie oder ihre Geschwindigkeit. Um ihre kinetische Energie zu vermindern, bremsen wir sie mit Licht. Das nennt sich Laserkühlung. Lichtquanten, auch Photonen genannt, haben Energien die von ihrer Farbe abhängen. Photonen an der blauen Seite des Regenbogenspektrums haben eine höhere Energie als die an der roten Seite. Atome können nur Photonen mit einer ganz bestimmten Farbe absorbieren, weil ihre Elektronen nur bestimmte quantisierte Energiezustände annehmen können. Genau so wie man nicht zwischen zwei Treppenstufen stehen kann, können sich die Elektronen nicht zwischen zwei solcher Energiezuständen befinden. Atome können Licht absorbieren, wenn die Energiedifferenz zweier Energiestufen mit der Ener-

* $v_{\mathrm{th}}(T = 293\,\mathrm{K}) = \sqrt{\frac{2k_{\mathrm{B}}293\,\mathrm{K}}{m_{\mathrm{Rb}}}} = 239\,\mathrm{m/s} \mathrel{\hat{=}} 860\,\mathrm{km/h}$

gie eines eintreffenden Photons übereinstimmt, wenn die Schwingungsfrequenz eines Photons „resonant“ mit dem Atom ist. Der Impuls des Photons wird dann auf das Atom übertragen.

Wie kann man mit diesem Mechanismus Atome kühlen? Wir nutzen den Doppler-Effekt aus. Der Doppler-Effekt ist das Phänomen von veränderter wahrgenommener Frequenz von sich bewegenden Licht- oder Schallquellen. Wie die Sirene eines passierenden Krankenwagens sich in der Frequenz zu verändern scheint, so passiert dies auch mit Lichtquellen. Für Laserkühlung werden Atome rot-verstimmtem Licht ausgesetzt, das ist Licht dessen Photonenenergien etwas unter einer der Elektronen-Stufen sind. Ein Atom, das sich von der Lichtquelle weg bewegt, erfährt eine geringere Lichtfrequenz und so eine geringere Photonenenergie. Ein Atom, das sich auf eine Lichtquelle zu bewegt, sieht eine höhere Photonenenergie. In diesem Fall sind die Photonen resonant mit dem Atom und können absorbiert werden. Der Impuls des Photons geht auf das Atom über und verringert so seine kinetische Energie.

Ist ein Atom von allen Seiten rot-verstimmtem Licht ausgesetzt, dann bewegt es sich immer entgegen einer Lichtquelle. Das Atom wird so in alle Richtungen gebremst und verringert seine thermische Energie. Durch Absorption von Photonenimpulsen können Atome bis in den Millikelvinbereich gekühlt werden. Das ist weniger als ein tausendstel Grad Celsius über dem absoluten Minimum von $-273.15\,^{\circ}\mathrm{C}$. Dies macht es auch einfacher die Atome einzufangen.

Einfangen Für das Einfangen von Atomen nutzen wir den sogenannten „Licht-Verschiebungs-Effekt“, der ohne die Absorption von Photonen auskommt. Um diesen Effekt zu erklären, muss man sich das Atom zunächst genauer ansehen. Es besteht aus einem positiv geladenen Kern, umgeben von negativ geladenen Elektronen. Ohne Außeneinwirkung ist das Atom unpolarisiert, so dass die Elektronenwolke den Kern gleichmäßig umhüllt.

Wird das Atom einem elektrostatischen Feld ausgesetzt, dann werden die Elektronen auf eine Seite gezogen und der Kern auf die andere. Elektronen und Kern ziehen sich noch immer an und sind nicht so einfach zu

trennen. Das Feld zieht sie auseinander, bis sie sich eben so stark anziehen, wie das elektrostatische Feld an ihnen zieht. Das Atom ist dann wieder im Gleichgewicht mit seiner Umgebung und hat seine Energie reduziert.

Setzt man das Atom stark rot-verstimmtem Licht aus, absorbiert es keine Photonen, das Licht übt lediglich Kraft auf den Atomkern und seine Elektronen aus. Sie schwingen dann mit langsamer Frequenz hin und her, und folgen dem elektrischen Feld des Lichtes. Man sagt, das Atom reagiert „in Phase“ mit dem externen Feld. In diesem Falle verringert das Atom seine Energie, es ist ein energetisch günstiger Zustand. Je höher die Lichtintensität, desto geringer ist die Energie des Atoms. Das Atom wird von Regionen hoher rot-verstimmter Lichtintensität angezogen.

Das Gegenteil geschieht bei blau-verstimmtem Licht. Je „blauer“ das Licht, desto höher ist die Frequenz der Photonen. Jetzt ist das Feld zu schnell, als dass die Elektronen und der Kern noch folgen können. Sie werden so schnell hin und her gezogen, dass sie immer etwas zu spät folgen. Das Atom schwingt nun *gegenphasig* mit dem antreibenden Feld. Das bedeutet, dass das Atom stets gegen das externe Feld polarisiert. Seine Energie ist nun höher als zuvor. Dies ist energetisch ungünstig und das Atom wird von Regionen hoher Lichtintensität abgestoßen.

Zusammengefasst ergibt dies: Das Atom wird von rot-verstimmtem Licht angezogen und von blau-verstimmtem Licht abgestoßen. Man erhält so eine Atomfalle einfach durch einen fokussierten, rot-verstimmten Laserstrahl. Die Atome werden von der Region hoher Intensität im Fokus angezogen. Indem der Laserstrahl gelenkt oder das elektromagnetische Feld anderweitig manipuliert wird, können die Atome transportiert werden. Sie folgen schließlich weiterhin der hohen Lichtintensität. Auf diese Art und Weise werden die Atome dann auf die Oberfläche der nanophotonischen Strukturen gebracht.

Nanophotonik Im Feld der Nanophotonik wird Licht im Nanometerbereich studiert. Im Alltag erfahren wir Licht als etwas, das sich geradlinig über makroskopische Distanzen fortbewegt. Auf Nanometerlänge beschränkt verhält es sich jedoch unintuitiv. Licht kann mit Spiegeln begrenzt werden, wie man es sich noch einfach vorstellen kann. Zwei par-

allele Spiegel können Licht leiten, es wird zwischen den Spiegeloberflächen hin und her reflektiert. So funktionieren Glasfasern mit großem Durchmesser. Das Licht verbleibt im Inneren und wird an der Grenze zwischen Glasfaserkern und -mantel reflektiert, auch wenn die Faser gebogen wird. Wenn jetzt der Kern kleiner wird, so wird das Licht nicht mehr reflektiert, sondern folgt der Faser wie Wasser in einem Gartenschlauch. So funktionieren Glasfasern mit kleinem Kern. Wird der Kern nun noch kleiner, so verlässt das Licht zum Teil den Kern und bewegt sich *auf der Oberfläche der Faser* fort. Dies bezeichnet man als „evaneszentes Licht“. Im Bilde des Gartenschlauch-Vergleiches flösse das Wasser auf der Oberfläche des Schlauches entlang. Wird der Kern wieder größer, kehrt das Licht folglich wieder in die Glasfaser zurück.

Es gibt jedoch noch andere Möglichkeiten evaneszentes Licht zu erzeugen. Mittels optischer Gitter kann es auf Metalloberflächen erzeugt werden. Das Gitter beugt das Licht, so dass es sich parallel zur Metalloberfläche ausbreitet. Das Licht koppelt mit Elektronenwellen auf dem Metall, zusammen formen sie ein Quasiteilchen mit dem Namen *Oberflächenplasmon*. Im Vergleich zu Licht auf einer Glasfaseroberfläche ist das Licht hier stärker räumlich begrenzt und hat eine höhere lokale Feldintensität. Das Licht klingt aber schneller ab. Dies geschieht durch ohmsche Verluste, genau so wie ihn Strom in einem Kabel erfährt.

Die Tatsache, dass Licht sich auf der Oberfläche von Materie fortbewegen kann, ermöglicht nanophotonische Instrumente, die mit Atomen wechselwirken können. Mit Hilfe dieses Lichtes können Atome eingefangen, manipuliert oder miteinander gekoppelt werden. Mit nanophotonischen Strukturen kann man sehr komplexe Potentiallandschaften mit sehr hohen lokalen Feldstärke und starken Gradienten für Licht-Atom Wechselwirkungen maßschneidern.

Die kleine Größe der nanophotonischen Strukturen hat vielerlei Vorteile. Viele Strukturen passen auf eine Probe und können dort mit einander wechselwirken, es skaliert gut. Weiterhin kann die Wechselwirkung zwischen Strukturen extrem schnell sein, da alle Elemente dicht beieinander sind.

Anwendungen Weshalb diese Forschungsrichtung? Welche Einsichten können wir gewinnen? Nanophotonik untersucht Licht im Nanometerbereich. Sie bringt das Vermögen der Optik auf Chipgröße und macht zugleich hohe lokale Lichtintensitäten und starke Gradienten zugänglicher. Diese extremen Lichtzustände ermöglichen schnelle und sehr empfindliche Messgeräte. Nanophotonik ermöglicht hoch-skalierbare Systeme, weil viele photonische Systeme mit einander interagieren können.

Die Kombination von Nanophotonik und kalten Atomen eröffnet ein Füllhorn an Möglichkeiten. Extreme Lichtzustände ermöglichen es, starke Koppelungen von Licht und Materie zu untersuchen. Dies ist eine Voraussetzung für Quanteninformatik. Starke Koppelungen beeinflussen Materie auf eine fundamentale Art und Weise und erlauben es, elektronische Energieniveaus maßzuschneidern. Nanophotonik kann auch die Einzelphotonen-Emission von Atomen beschleunigen.

Die Skalierbarkeit der Nanophotonik kann nun auch in die Atomphysik angewendet werden. Atome können auf sehr kleinen Längenskalen eingefangen, gekoppelt und manipuliert werden. Zudem kann auch die Potentiallandschaft für die Atome entworfen und gestaltet werden.

Einsichten Was können wir von diesem Projekt lernen? Der Hauptaspekt ist die Forschung an neuen Arten von Licht-Materie Wechselwirkungen. Wir können dies mit vielen unterschiedlichen Methoden angehen. Der experimentelle Aufbau funktioniert mit unterschiedlichen Arten von Proben. Photonische- oder plasmonische Proben mit Metallfilmen oder Halbleitermembranen, Wellenleiter oder Resonatoren können binnen zwei Tagen gewechselt werden.

Ziel ist es, verschiedene Arten von Experimenten schnell nacheinander durchführen zu können. So kann unsere Forschung viele verschiedene interessante Themen abdecken und ihre Synergieeffekte ausnutzen.

Inhalt der Prüfschrift Die Prüfschrift beginnt mit einer formalen Einführung in das Forschungsfeld in Kapitel 1. Das Kapitel 2 beschreibt ein Beispielexperiment, das man mit dem experimentellen Aufbau durch-

führen kann. Weiterhin werden weiterführende Schritte für nachfolgende Forschungen aufgezeigt. Der Aufbau selbst ist im Detail in Kapitel 3 beschrieben und wird anschließend in Kapitel 4 charakterisiert. Es stellte sich heraus, dass der Aufbau eines solchen Experimentes doch sehr komplex ist. Atome können auf die Probenoberfläche transportiert werden, jedoch mit weniger Kontrolle als nötig. Kapitel 5 handelt von numerische Simulationen, um zu erklären, was unter realistischen experimentellen Konditionen tatsächlich vor sich geht. Die Simulationen beschreiben in der Tat die Phänomene, die wir beobachtet haben und geben wertvolle Einsichten zur Lösung der Probleme. Wir haben jetzt eine gute Vorstellung von möglichen Experimenten und deren Rahmenbedingungen.

Folgende Schritte Die numerischen Simulationen haben uns einige Dinge aufgezeigt, die wir verbessern können. Eigentlich ist das Ziel fast erreicht: Wir haben eine Vakuumkammer mit einer praktischen und schnellen Proben-Austausch-Vorrichtung. In dieser Vakuumkammer können wir Wolken aus sehr reinen Rubidiumatomen auf Millikelvin-Temperatur herunterkühlen und manipulieren. Anschließend können wir die Atome auf eine Probenoberflächen transportieren. Weiterhin haben wir an Vorstudien mit verschiedenen nanophotonischen Strukturen gearbeitet. Ist der Atom-Transport-Mechanismus verbessert, dann sind viele weitere Experimente möglich. Man wird sehen und mit Aufmerksamkeit beobachten, was die nachfolgende Generation an dieses spannende Forschungsfeld herantragen kann und wird.

4. Summary in Chinese 摘要

本论文介绍了一个可以让冷原子接近纳米光子结构的实验装置。对这个装置人们可以提出很多问题：以什么方式使两者靠近？可以达到多近？为什么需要“冷”原子？“冷”原子有多冷？纳米光子结构又是什么？做这个研究的出发点是什么？最重要的是：我们为什么要研制这个装置？从这个过程中我们能学到哪些物理原理？

原子 我们能够看到、摸到和闻到的东西都是由原子构成的。这些微小的基本物质单元可以有不同的基本状态：比如固态、液态和气态。在我们的实验中，我们使用的是气态下的铷原子。在实验过程中，我们要让这些原子保持在非常接近纳米光子结构的位置。然而在室温下，铷气中的原子移动非常快。其速度高达860公里/小时左右，接近马赫速度。要控制铷原子的位置，我们必须将其减速。减速的方式就是冷却。

冷却 原子的温度越高，动能越大，速度也就越快。我们使用激光让铷原子减速，降低它们的动能。这就是所谓的激光冷却。

光的量化单位是光子。光子的能量与其颜色相对应。在光谱蓝色端的光子能量比红色端的光子能量更高。特定元素的原子只能吸收特定颜色的光子，因为原子中的电子只能在特定的能级（原子轨道）之间跃迁。就像一个人上楼梯，台阶越高，需要的力气就越大。正如我们不能站在两个台阶中间，电子也不能处于两个能级之间。当传入的光子能量与一个电子跃迁到更高的能级所需的能量相匹配时，即当光子的频率与原子相匹配时，原子就可以吸收光。光子的动量就被转移到原子中。

如何利用这个原理来冷却原子呢？我们利用多普勒效应。多普勒效应是指观察者对移动的声音或光源感受到的频率与波源发出的频率不同的现象。救护车驶过时我们听到的警笛声调（声波频率）会变化，类似的现象在光波中也会发生。激光冷却，就是将原子云暴露在其频率稍微低于原子谐振频率的激光（红失谐光）中。也就是说，红失谐光的光子能量比原子中电子跃迁能级所需的能量略低。当一个原子在远离此激光，它感知的光频降低，对它来说激光的光子能量变得更少。一个向着光源靠近的原子则会感知到更高的光子能量。这个光子就能和原子共振，并被吸收。光子的反方向动量会转移到原子上，降低其动能。

通过将原子全方位暴露在红失谐光中，原子就会一直向着光的反方向走。这样原子就会全方位减速，降低其热能。通过吸收光子的动量，原子可以冷却到毫加尔文之下。即不高于绝对零度−273.15 °C的千分之一。这样使这些原子更容易被捕获。

捕获 捕获原子的原理叫做“光偏移”，这个过程不依靠对光子的吸收。要解释这个原理，我们需要更近一步观察原子本身。原子是由一个带正电荷的原子核，和周围带负电荷的电子组成的。没有外界干扰的情况下，原子不会发生偏振，电子云均匀的围绕在原子核周围。

原子倾向于进入或保留在能量更低的状态中。例如，当暴露在静电场中时，电子会被拉到一侧，而原子核在另外一侧。它们仍然相互吸引，所以不会轻易分开。静电场将原子核和电子拉开，直到拉力与原子核和电子之间的吸引力相抵消。这时原子与周围环境相平衡，能量也降低了。这是一个相对稳定的状态。

如果原子暴露在**远红**失谐光中，原子不会吸收光子，但光的电磁场会对电子和原子核产生力的作用。它们会跟着光，以缓慢的频率来回移动。这叫做原子与该场同相。在这种环境下，原子的移动降低其能量，是能量更低的状态。光的强度越高，原子的能量就越低。原子会被吸引至红失谐光中强度更高的区域。

对于蓝失谐光来讲，就会截然相反。光越“蓝”，光子的频率就越高。电磁场的速度过快，原子跟不上。电荷被快速的来回拖拽，总是慢半拍。这样原子的振动和驱动场有相差。这意味着原子会发生偏振抵御外部场，因此能量会比之前更高。原子会因此寻找低强度的区域。

换句话说，原子会被红失谐光吸引，被蓝失谐光排斥。因此，可以简单地通过红失谐光激光束来捕获原子。原子会被吸引到高强度场中。通过控制光束或者操控磁场，我们可以转移原子，因为它们会跟着高强度红失谐光移动。这就是将原子引导到纳米光学样品表面的原理。

纳米光子学 纳米光子学是研究光在纳米尺度下的特性的科学。在日常生活中，我们认为宏观上，光是沿直线传播的。然而，在纳米尺度上，就不这么直观了。例如，光可以受镜子局限，两面平行的镜子就可以使光线来回反射。这是大芯径光纤的工作原理。光在光纤芯内部和光纤外层的交界处不断的进行反射。即使是弯曲的光纤，光也保持在光纤内

部。当光纤芯变小，光就不再反射或改变路径了。它像水一样，可以随着胶皮水管流动。如果光纤芯变得更细，在某一时刻光开始泄露，一部分光会在**光纤外**流动。这种光被称为“倏逝光”。就像水在胶皮水管表面流动。当光纤慢慢变大，光还会回到内部。

创造倏逝光的方法有很多种。在光栅的帮助下，可以在金属表面产生。光栅将射入的激光束，衍射到平行于金属表面。激光在金属表面产生电子波并与之耦合，共同组成一个准粒子。这被称为**表面等离激元**。相比光纤表面的光，表面等离激元有更严格的空间约束力和更强的局部场强。然而，由于金属中的欧姆损耗等原因，它们像电线中的电流一样，衰减较快。

利用光可以在物质表面传播这一现象，我们可以构建能够和原子相互作用的纳米光子仪器。这种光可以用来储存、控制原子或将原子耦合。利用纳米光学结构，我们可以利用高度局部化和高梯度的电磁场，创造出非常复杂的势能布局来完成光和原子的相互作用。

纳米光学结构的小尺寸有着诸多优点。许多结构可以在同一个样品中彼此相互作用。由于结构规模增大时，结构间的距离仍然相对较小，所以可扩展性强。因为所有结构元素之间距离非常近，所以不同结构之间的相互作用非常快速。

应用 这项研究课题的应用在哪里？我们能从中获得什么？纳米光学研究光在纳米尺度下的状态。它把光学的强大功能浓缩在芯片大小的区域里，同时还使得像高局域强度和强磁场剃度这样的功能更容易实现。这些光的极端状态造出了快速，高敏感度的测量仪器。由于许多光子系统能够快速的相互作用，纳米光学也使得有高度可扩展性的系统成为可能。

纳米光子学与冷原子的结合提供了非常多的机遇。将原子暴露在光的极端状态下可以使光和物质耦合。这是量子信息处理的先决条件。高强度的耦合从根本上控制物质，并使制造电子能量级成为可能。纳米光子学还可以加快原子作为单光子发射器的发射速度。

纳米光子学的可扩展性已经延伸到原子物理领域。原子可以在非常小的范围内，大量的被捕获，耦合以及操纵。此外，原子的势能分布是高度可控的。

启示 我们期待从这个项目中学到什么呢？首先就是学习光与物质相互作用的新途径。我们的实验装置有多种方式达到这个目的。很多不同种类的样本都可以在此装置上使用。带有金属膜、波导或谐振器的光子或等离子样品在短短两天内就可以完成交换。

这样做的目的是要短时间快速进行不同种类的实验，以便利用协同效应，覆盖多个我们感兴趣的课题。

论文内容 本文第一章正式介绍研究领域。第二章描述了一个此实验装置上可以做的案例实验，以及日后研究人员继续实验可采取的方式。第三章详细介绍装置的设计和组成。第四章介绍装置的性能和规格。建立这个装置的过程是很复杂的。我们可以将原子送到样本表面，但是可控性仍低于实验需要的水平。第五章包含一个两步的数值模拟来帮助我们解释在真实实验条件下，原子输送的实际情况。该模拟再现了我们观察到的现象，并对解决仪器的现有不足提供有价值的启示。现在我们可以很好的理解什么类型的实验是可行的，以及边界条件是什么。

展望 数值模拟结果为我们提供了一些可以改善现有装置的建议。我们已经很接近目标的实验状态：一个能够快速交换样本的真空室。真空室中，我们可以控制纯净的铷原子云，并将其降温至毫开尔文温度。原子已经可以被递送至样本表面。我们也进行了多个试点实验，尝试了多种有不同纳米光子结构的样品。一旦原子运输更精确，更多实验就会成为可能。我期待着看到新一代的研究人员能够在此科学领域有进一步的建树。

Acknowledgements

Oh what a ride. An endeavour like a PhD project is always a very personal experience. Sometimes it may look like a normal job, but that's far from it. Every day is different. One is constantly battling Mother Nature to reveal her secrets, with one's wits and mankind's knowledge as weapons. In the end, after shedding blood, sweat and tears, one adds a tiny piece to the puzzle of that mankind's knowledge, ready to be wielded by the next generation to continue the fight. And it is worth it. You not only contributes to a greater good, it also makes you grow as a person. In the end, I learned so much about myself and other people. Maybe even more than about physics.

The work of many years is coming to an end, distilled into this thesis. This project started with an empty laboratory. I had the pleasure and honour to plan, build and set up much of the present setup. This would not have been possible without the support, trust and hard work of many wonderful people.

First and foremost I thank my supervisor and copromotor Dries van Oosten. It was an honour to be your first mate on your ship, or 'the monkey that speaks', in your words. I saw your group come to be, grow and transform. You learned a lot in these years and so did I. Your vast amount of knowledge spans many fields of physics and allows your group to be diverse and agile. This is something that really makes you stand out. Time will tell where your ship will go, but I know it will be somewhere exciting.

Peter van der Straten, you were my copromotor and a voice of wisdom in rough seas. I treasure your decisiveness and focus on solutions. A seasoned veteran like you is no common sailor. For me you were the wise

owl in the lookout, even though you are a captain of your own ship.

The mighty Neptune in the seas is Jaap Dijkhuis. You were navigating the shallows of bureaucracy and politics. I could always count on you for help and support. You left before the end of my journey and went into hard-earned retirement. Please enjoy it, it is well-deserved.

Chief engineer for everything involving currents is Frits Ditewig, a true master in his profession. There was none of my electronic problem for which you could not find a solution. Being around so many wise guys (that earned countless unspoken I-told-you-so's) did not put you off. Instead you continued your duty even after retirement. Chapeau! Luckily, in the end you could get a worthy successor, Dante Kilian.

Dante, you take over a lot of legacy, but you are the right guy for that job. You fix everything that we throw at you and I thoroughly enjoyed our discussions about whatever side projects we were currently indulging in, be it audio DACs or white dinners. I'm happy to have had you around.

Paul Jurrius is carpenter, plumber, metal worker, craftsman and artisan in one. We were the Golden Duo. I had a blast planning and building parts of the setup with you. Never did I have the feeling of bringing you problems to solve, it were always fun challenges with creative solutions in the end. Plus, being the chief mate of borrels, you were bonding the crew.

Our chief officer of security, communications and logistics is Cees de Kok. You govern our morse-machines, manage stocks and orders, repair lasers and are our secretary and general Jack-of-all-trades. You are fixing things behind the scenes and even in very hard times we could rely on your commitment.

Countless other monkeys were aboard with me, more than I could name. There are a handful that I cannot let go without special mention.

Arjon van Lange, you were the first one to share the journey with. I learned a lot from you, more than you probably know. You have the daunting task of finishing the battle with Mother Nature, together with Kostas Voutyras. Keep on rockin', both of you.

Sandy Pratama is the third simian of the starting trio. You are a true

code monkey and master of the C's. Your honesty and outspokenness is refreshing. Somehow you manage to be more direct than the Dutch. Never lose that! Thank you also for introducing me to lots of good food and showing me the best sambal in the country.

Initially starting as a cabin boy, Sebastiaan "Sebas" Greveling did such good work that he was soon promoted to monkey rank. Now you still don't stop being excellent and built a setup that condenses photons into a BEC, together with Marcel Scholten who joined later the same way. As a friend and colleague it is a pleasure to see you succeed. Furthermore, you are always in the centre of social happenings, challenging Paul as chief mate of borrels. Thank you for helping me with the Dutch parts of the thesis. It turned out great!

Mama, zu sagen, ohne Dich wäre ich nicht, hier ist eine Binsenweisheit. Aber es stimmt auf mehr als die offensichtliche Weise. Du hast mich immer unterstützt auf meinem Weg, mir Rat gegeben, Dich aber nie aufgedrängt. Du hast mitgefiebert und mich begleitet durch Höhen und Tiefen, eng an meinem Leben Teil gehabt und hast es noch weiterhin. Du würdest es selbst nie so sehen, aber diese Arbeit ist auch Dein Verdienst. Danke für alles.

Papa, danke, dass Du mir hilfst meinen Arbeitsstress in rechte Licht zu rücken und mein Augenmerk auf die wichtigen Dinge im Leben zu richten. Deine Gelassenheit, Reiselust und Begierde nach neuen Erfahrungen sind mir ein Ansporn. Dein Interesse an meiner Reise durch's Leben, Dein offenes Ohr und Deine Unterstützung haben einen großen Anteil an dieser Arbeit. Danke, dass Du stets bei uns vorbei schaust, wenn es Dich in den Süden zieht, oder auch einfach mal so.

Gaby, mein Lieblingstäntchen. Deine Wissbegierde ist eine Inspiration. Du fragst und hinterfragst viel und nimmst stets an meinem Leben Teil. Ich wünsche mir, dass ich in meinem weiteren Fortgang so viel Neugier und Tatendrang behalte wie Du sie hast. Baci, baci, Dein Nipote.

Louisa, vielen Dank für's Probelesen der deutschen Passagen. Du findest nicht nur jegliche grammatischen Fehler und verkehrte Kommata, sondern zeigst mir auch die Schönheit meiner Muttersprache.

赵越爸爸妈妈，谢谢你们一直以来对我的关怀和鼓励！

Zhao Yue, my one and only. I don't even know where to begin. We met at the beginning of my PhD, and now, almost six years later, I still can't imagine life without you. You experienced this project the closest. You shared all my highs and lows and supported me through all of them. You helped me work on my weaknesses and showed me strengths that I never saw before. You took part in moulding me into the person that I am now. For everything you have done, I cannot thank you enough. You have my deepest gratitude. And Love. 谢谢赵越，我爱你。

Bibliography

[Båå82] Tryggve Bååk. Silicon oxynitride; a material for grin optics. *Appl. Opt.*, 21(6):1069–1072, Mar 1982.

[BDN12] Immanuel Bloch, Jean Dalibard, and Sylvain Nascimbène. Quantum simulations with ultracold quantum gases. *Nature Physics*, 8(4):267–276, 2012.

[BHB+09] M Bajcsy, Sebastian Hofferberth, V Balic, T Peyronel, Mohammad Hafezi, Alexander S Zibrov, V Vuletic, and Mikhail D Lukin. Efficient all-optical switching using slow light within a hollow fiber. *Physical review letters*, 102(20):203902, 2009.

[BK06] Sergey I Bozhevolnyi and Laurens Kuipers. Near-field characterization of photonic crystal waveguides. *Semiconductor Science and Technology*, 21(5):R1, 2006.

[BK07] Mark L Brongersma and Pieter G Kik. *Surface plasmon nanophotonics*. Springer, 2007.

[BLSD+10] Aleksandr Biberman, Benjamin G Lee, Nicolás Sherwood-Droz, Michal Lipson, and Keren Bergman. Broadband operation of nanophotonic router for silicon photonic networks-on-chip. *IEEE Photon. Technol. Lett*, 22(12):926–928, 2010.

[Bon15] PC Bons. *Probing the properties of quantum matter; an experimental study in three parts using ultracold atoms*. PhD thesis, 2015.

[BSS92] D. S. Bomse, A. C. Stanton, and J. A. Silver. Frequency modulation and wavelength modulation spectroscopies:comparison of experimental methods using a lead-salt diode laser. *Appl. Opt.*, 31(6):718–731, Feb 1992.

[BSS+99] S Bize, Y Sortais, MS Santos, C Mandache, A Clairon, and C Salomon. High-accuracy measurement of the 87rb ground-state hyperfine splitting in an atomic fountain. *EPL (Europhysics Letters)*, 45(5):558, 1999.

[CCC+15] Rémi Carminati, Alexandre Cazé, Da Cao, F Peragut, V Krachmalnicoff, Romain Pierrat, and Yannick De Wilde. Electromagnetic density of states in complex plasmonic systems. *Surface Science Reports*, 70(1):1–41, 2015.

[CKM+90] S. Chu, M. Kasevich, K. Moler, E. Riis, and D. Weiss. Precision measurements using laser cooled atoms. In *Precision Electromagnetic Measurements, 1990. CPEM '90 Digest., Conference on*, pages 5–6, June 1990.

[CLPS15] Victor J Cadarso, Andreu Llobera, Mar Puyol, and Helmut Schift. Integrated photonic nanofences: Combining subwavelength waveguides with an enhanced evanescent field for sensing applications. *ACS nano*, 2015.

[CRGW03] G. Cennini, G. Ritt, C. Geckeler, and M. Weitz. Bose–Einstein condensation in a CO2-laser optical dipole trap. *Applied Physics B*, 77(8):773–779, 2003.

[Dee06] R. Deep. *Probability and Statistics with Integrated Software Routines*. Academic Press, 2006.

[Dre70] KH Drexhage. Influence of a dielectric interface on fluorescence decay time. *Journal of luminescence*, 1:693–701, 1970.

[DSWW98] K. Dieckmann, R. J. C. Spreeuw, M. Weidemüller, and J. T. M. Walraven. Two-dimensional magneto-optical trap

as a source of slow atoms. *Phys. Rev. A*, 58:3891–3895, Nov 1998.

[Dua08] F. J. Duarte. *Tunable Laser Applications, Second Edition*. Optical Science and Engineering. CRC Press, 2008.

[Eul68] L. Euler. *Institutionum calculi integralis*. Number Bd. 1 in Institutionum calculi integralis. Impensis Academiae Imperialis Scientiarum, 1768.

[FMSH07] Ian Freestone, Nigel Meeks, Margaret Sax, and Catherine Higgitt. The lycurgus cup—a roman nanotechnology. *Gold Bulletin*, 40(4):270–277, 2007.

[Gap09] D. Gapontsev. *YLR LP Series manual*. IPG photonics, 2009.

[Geo15] Iulia Georgescu. Rubidium round-the-clock. *Nature chemistry*, 7(12):1034–1034, 2015.

[GKC92] Kurt E. Gibble, Steven Kasapi, and Steven Chu. Improved magneto-optic trapping in a vapor cell. *Opt. Lett.*, 17(7):526–528, Apr 1992.

[GOSDD98] D. Guéry-Odelin, J. Söding, P. Desbiolles, and J. Dalibard. Strong evaporative cooling of a trapped cesium gas. *Opt. Express*, 2(8):323–329, Apr 1998.

[GP08] M. Grasselli and D. Pelinovsky. *Numerical Mathematics*. Jones & Bartlett Learning, 2008.

[Gre13] S. Greveling. *An Optical Conveyor for Light-Atom Interaction*. Master thesis, Universiteit Utrecht, 2013.

[Gri05] Paul F Griffin. *Laser Cooling and Loading of Rb into A Large Period, Quasi–Electrostatic, Optical Lattice*. PhD thesis, Durham University, 2005.

[GTC+12] M. Gullans, T. G. Tiecke, D. E. Chang, J. Feist, J. D. Thompson, J. I. Cirac, P. Zoller, and M. D. Lukin. Nanoplasmonic lattices for ultracold atoms. *Phys. Rev. Lett.*, 109:235309, Dec 2012.

[GTHC+15] Alejandro González-Tudela, C-L Hung, Darrick E Chang, J Ignacio Cirac, and HJ Kimble. Subwavelength vacuum lattices and atom–atom interactions in two-dimensional photonic crystals. *Nature Photonics*, 9(5):320–325, 2015.

[GWO99] Rudolf Grimm, Matthias Weidemüller, and Yurii B Ovchinnikov. Optical dipole traps for neutral atoms. *arXiv preprint physics/9902072*, 1999.

[Hec15] E. Hecht. *Optics*. Pearson Education, 2015.

[HF01] J.D. Hoffman and S. Frankel. *Numerical Methods for Engineers and Scientists, Second Edition,*. Taylor & Francis, 2001.

[HLW+14] XJ He, TY Li, L Wang, JM Wang, XH Tian, JX Jiang, and ZX Geng. Electromagnetically induced transparency and slow light in a simple complementary metamaterial constructed by two bright slot-structures. *Applied Physics A*, 116(2):799–804, 2014.

[HNW08] E. Hairer, S.P. Nørsett, and G. Wanner. *Solving Ordinary Differential Equations I: Nonstiff Problems*. Springer Series in Computational Mathematics. Springer Berlin Heidelberg, 2008.

[Ise09] A. Iserles. *A First Course in the Numerical Analysis of Differential Equations*. A First Course in the Numerical Analysis of Differential Equations. Cambridge University Press, 2009.

[JDGD+13] B Juliá-Díaz, T Graß, O Dutta, DE Chang, and M Lewenstein. Engineering p-wave interactions in ultracold atoms using nanoplasmonic traps. *Nature communications*, 4, 2013.

[Joh15] Justin Johnson. neural-style. https://github.com/jcjohnson/neural-style, 2015.

[KCM+00] S. J .M. Kuppens, K. L. Corwin, K. W. Miller, T. E. Chupp, and C. E. Wieman. Loading an optical dipole trap. *Physical review A*, 62(1):013406, 2000.

[KDJ+93] W. Ketterle, K. B. Davis, M. A. Joffe, A. Martin, and D. E. Pritchard. High densities of cold atoms in a dark spontaneous-force optical trap. *Physical Review Letters*, 70:2253–2256, April 1993.

[Leb01] P.N. Lebedev. The experimental study of the pressure of the light. *Annalen der Physik, Leipzig*, 6:433, 1901.

[McG62] Daniel D McGarry. The metalogicon of john salisbury, 1962.

[MDS+88] Naoto Masuhara, John M Doyle, Jon C Sandberg, Daniel Kleppner, Thomas J Greytak, Harald F Hess, and Greg P Kochanski. Evaporative cooling of spin-polarized atomic hydrogen. *Physical Review Letters*, 61(8):935, 1988.

[ME88] P.W. Milonni and J.H. Eberly. *Lasers*. Wiley Series in Pure and Applied Optics. Wiley, 1988.

[MvdS12] H. J. Metcalf and P. van der Straten. *Laser Cooling and Trapping*. Graduate Texts in Contemporary Physics. Springer New York, 2012.

[NH01] E. F. Nichols and G. F. Hull. A preliminary communication on the pressure of heat and light radiation. *Phys. Rev. (Series I)*, 13:307–320, Nov 1901.

[O'H05] J. F. O'Hanlon. *A User's Guide to Vacuum Technology*. Wiley, 2005.

[ORI+10] Ardavan F Oskooi, David Roundy, Mihai Ibanescu, Peter Bermel, John D Joannopoulos, and Steven G Johnson. MEEP: A flexible free-software package for electromagnetic simulations by the FDTD method. *Computer Physics Communications*, 181(3):687–702, 2010.

[Ozb06] Ekmel Ozbay. Plasmonics: merging photonics and electronics at nanoscale dimensions. *science*, 311(5758):189–193, 2006.

[Pre96] D. W. Preston. Doppler-free saturated absorption: Laser spectroscopy. *American Journal of Physics*, 64:1432–1436, November 1996.

[Rol67] Dr. P. K. Rol. *Inleiding tot de vacuümtechniek*. Argus, 1967.

[RPC+87] E. L. Raab, M. Prentiss, Alex Cable, Steven Chu, and D. E. Pritchard. Trapping of neutral sodium atoms with radiation pressure. *Phys. Rev. Lett.*, 59:2631–2634, Dec 1987.

[San06] J. E. Sansonetti. Wavelengths, transition probabilities, and energy levels for the spectra of rubidium (rb i through rb xxxvii). *J. Phys. Chem. Ref. Data*, 35(1):301–421, 2006.

[Sch15] Schott. *Optical Glass Data Sheets*. Schott, 7 2015.

[SD07] S.N. Sivanandam and S.N. Deepa. *Introduction to Genetic Algorithms*. Springer Berlin Heidelberg, 2007.

[SGOD+99] J Söding, D Guéry-Odelin, P Desbiolles, F Chevy, H Inamori, and J Dalibard. Three-body decay of a rubidium bose–einstein condensate. *Applied physics B*, 69(4):257–261, 1999.

[SGV+12] Philipp Schneeweiss, M Gierling, G Visanescu, DP Kern, TE Judd, A Günther, and J Fortágh. Dispersion forces between ultracold atoms and a carbon nanotube. *Nature nanotechnology*, 7(8):515–519, 2012.

[SOT97] T. A. Savard, K. M. O'Hara, and J. E. Thomas. Laser-noise-induced heating in far-off resonance optical traps. *Phys. Rev. A*, 56:R1095–R1098, Aug 1997.

[Ste09] D. A. Steck. Rubidium 87 D Line Data. URL http://steck.us/alkalidata/rubidium87numbers.pdf, 2009.

[SZS14] Christian Stehle, Claus Zimmermann, and Sebastian Slama. Cooperative coupling of ultracold atoms and surface plasmons. *Nature Physics*, 10(12):937–942, 2014.

[Tho15] *PDA36A(-EC) Si Switchable Gain Detector User Guide*, rev d edition, March 2015.

[Trä12] F. Träger. *Springer Handbook of Lasers and Optics*. Springer, 2012.

[TTdL+13] JD Thompson, TG Tiecke, NP de Leon, J Feist, AV Akimov, M Gullans, AS Zibrov, V Vuletić, and MD Lukin. Coupling a single trapped atom to a nanoscale optical cavity. *Science*, 340(6137):1202–1205, 2013.

[TTdL+14] TG Tiecke, Jeffrey Douglas Thompson, Nathalie Pulmones de Leon, LR Liu, V Vuletić, and Mikhail D Lukin. Nanophotonic quantum phase switch with a single atom. *Nature*, 508(7495):241–244, 2014.

[TVH+06] Matthias Taglieber, A-C Voigt, Florian Henkel, Sebastian Fray, TW Hänsch, and Kai Dieckmann. Simultaneous magneto-optical trapping of three atomic species. *Physical Review A*, 73(1):011402, 2006.

[vOK11] D. van Oosten and L. Kuipers. Trapping a single atom with a fraction of a photon using a photonic crystal nanocavity. *Phys. Rev. A*, 84:011802, Jul 2011.

[VRS+10] E. Vetsch, D. Reitz, G. Sagué, R. Schmidt, S. T. Dawkins, and A. Rauschenbeutel. Optical interface created by laser-cooled atoms trapped in the evanescent field surrounding an optical nanofiber. *Phys. Rev. Lett.*, 104:203603, May 2010.

[VS96] U Volz and H Schmoranzer. Precision lifetime measurements on alkali atoms and on helium by beam–gas–laser spectroscopy. *Physica Scripta*, 1996(T65):48, 1996.

[Wie08] C. E. Wieman. *Collected Papers of Carl Wieman*. World Scientific Publishing Company, 2008.

[YSJH96] Jun Ye, Steve Swartz, Peter Jungner, and John L Hall. Hyperfine structure and absolute frequency of the 87 rb 5p 3/2 state. *Optics letters*, 21(16):1280–1282, 1996.

[ZXL+12] Wenjia Zhang, Lin Xu, Qi Li, Hugo LR Lira, Michal Lipson, and Keren Bergman. Broadband silicon photonic packet-switching node for large-scale computing systems. *Photonics Technology Letters, IEEE*, 24(8):688–690, 2012.

Curriculum Vitae

Born in Kiel, Germany on 2nd September 1981.

1992 – 2001	**Abitur (university-entrance diploma)** *Ricarda Huch Schule*	Kiel, Germany
2002 – 2010	**BSc & MSc (Diploma)** *Universität Konstanz* Built a titanium:sapphire laser, conducted single mode spectroscopy and terahertz generation. Research Semester at NIST in Boulder, Co., USA. Thesis: *Setup and Application of a 10 GHz Femtosecond Laser*	Konstanz, Germany
2010	**Graduate Student Assistant** *Universität Konstanz* Operated and characterised an excimer laser.	Konstanz, Germany
2010 – 2016	**PhD in Physics** *Universiteit Utrecht* Built a laboratory and a delicate optical setup that uses lasers to manipulate atom clouds in ultra-high vacuum. Designed and fabricated nanoplasmonic samples. Set up servers and wrote numerical simulations. Thesis: *A Versatile Atom Transport Apparatus for Photonics*	Utrecht, The Netherlands
2016 – present	**IT Researcher** *CBS (Centraal Bureau voor de Statistiek)* Developing software to bring new technologies into statistics. Innovating data collection and Big Data management.	Den Haag, The Netherlands